Universidade do Minho
Escola de Engenharia

Pedro Henrique Oliveira de Melo Santos

Growth and characterization of $Cu(In,Ga)Se_2$ thin film solar cells with a Cu-rich Cu-In-Ga target

Dissertação de Mestrado

Mestrado em Engenharia Física

Trabalho efetuado sob a orientação de

Dr. Sascha Sadewasser

Professor Dr. João Pedro dos Santos Hall Agorreta de Alpuim

Dezembro de 2020

ACKOWLEDGMENTS

Firstly, I would like to express my gratitude to my supervisor, Dr. Sascha Sadewasser, for all the support, constant availability to help, and guidance that you gave me throughout the thesis. I would also like to thank Professor Pedro Alpuim, who was my Universidade do Minho supervisor, for all the classes you give me throughout my degree, which motivated me to do a thesis in this area.

It is impossible to acknowledge the work done in this thesis without acknowledging all of the INL LaNaSC (Laboratory for Nanostructured Solar Cells) group members. Thanks for all the training, stimulating discussions, and all the help that you gave throughout this year. Especially during the tough times that we face today, it was motivating to know that I have a support group, that was willing to help me with any difficulties that I faced.

Finally, but by no means least, to all my friends, my girlfriend Catarina, and my family, thank you for always believing in me and motivating me during my academic journey.

STATEMENT OF INTEGRITY

I hereby declare having conducted this academic work with integrity. I confirm that I have not used plagiarism or any form of undue use of information or falsification of results along the process leading to its elaboration.

I further declare that I have fully acknowledged the Code of Ethical Conduct of the University of Minho.

ABSTRACT

High-efficiency $Cu(In,Ga)Se_2$ (CIGSe) thin-film solar cells are typically fabricated by a multi-stage co-evaporation process, where one of these stages leads to a Cu-rich composition and the other stages balance the CIGSe layer composition, to reach the desired stoichiometries. Cu-rich conditions favor the growth of CIGSe grains, improving the overall efficiency of the solar cell.

In this work, CIGSe absorber layers were deposited on soda-lime glass/molybdenum (SLG/Mo) substrates by sputtering from a Cu-In-Ga (CIG) target with the following composition: $Cu_{0.6}In_{0.25}Ga_{0.15}$. Selenium was supplied simultaneously by a pulsed valved-cracker evaporation source. The Cu-rich nature of the CIG target lead to the presence of Copper-Selenide on the absorber layer, which is known to be detrimental to the performance of CIGSe solar cells. To eliminate this undesired phase, in a first approach, Potassium cyanide etching (KCN-etching) was used. Absorber layers were deposited at temperatures of 200°C, 350°C, 400°C, 450°C, and 500°C. SEM, EDX, XRD, and Raman spectroscopy revealed that an increase in temperature leads to an improved CIGSe film. Despite this, the absorber layers manifested well-pronounced grain boundaries and a large density of holes near the grain boundaries, all of which can be detrimental for the solar cell performance. To fabricate complete solar cells, a CdS buffer layer was deposited by chemical bath deposition, and an i-ZnO/ZnO:Al double layer was sputter-deposited as the front contact. Maximum efficiency of 8.4% was obtained for a deposition temperature of 450°C. The I-V curves of solar cells deposited at 500°C exhibited a reverse-bias current leakage behavior, possibly to the existence of pinholes or the presence of Copper-Selenide in deeper regions of the absorber layer, not reached by the KCN solution. An average efficiency of 3.4% was obtained for the 500°C solar cell.

In a second approach, the excess Copper was consumed by a post-deposition of Indium-Selenide following the CIGSe deposition, thus avoiding the need for the KCN-etching process. The temperature selected for such depositions was 500°C. Owing to the extra supplied Indium, the CIGSe layers submitted to this treatment have a lower [Ga]/([Ga]+[In]) (GGI) ratio compared with the GGI ratio of the KCN-treated samples. This GGI ratio difference is one of the focal points when characterizing the difference between the absorber layers. The Indium post-deposition leads to more compact films with less pronounced grain boundaries, and an inferior density of holes. Solar cell results showed improved efficiencies, reaching an average of 6.1%, which was a significant enhancement to the 3.4% obtained for the KCN solar cell. The reverse-bias current leakage problem was successfully eliminated, thus confirming that it was the KCN-etching that causes this problem.

Key words: CIGSe, Indium, KCN, post-deposition

RESUMO

Células solares de filme finos de $Cu(In,Ga)Se_2$ (CIGSe) são tipicamente fabricadas através de um processo de co evaporação composto por várias fases, onde uma dessas fases resulta numa composição rica em Cobre, e as restantes fases balanceiam a composição da camada CIGSe, atingindo as estequiometrias desejadas. Uma deposição com excesso de Cobre favorece o crescimento dos grãos do CIGSe, melhorando a eficiência da célula solar.

Neste trabalho, filmes finos de CIGSe foram depositados em substratos de vidro/Molibdénio, com recurso a um alvo de Cu-In-Ga (CGI) com a seguinte composição química: $Cu_{0.6}In_{0.25}Ga_{0.15}$. Selénio foi fornecido simultaneamente com recurso a uma fonte de evaporação pulsada. A natureza rica em Cobre do alvo de *CIG* resulta na presença da fase *Copper-Selenide* no filme, que, caso não seja removida, é prejudicial para o desempenho das células solares. Numa primeira abordagem, está fase será eliminada com recurso a *KCN-etching*. Camadas de *CIGSe* foram depositadas com as seguintes temperaturas: 200 °C, 350 °C, 400 °C, 450 °C e 500 °C. Análises de SEM, EDX, XRD e espectroscopia de Raman revelaram que um aumento na temperatura de deposição resulta numa melhoria das propriedades do filme de CIGSe. Contudo, todas as camadas manifestaram fronteiras de grão muito pronunciadas, e uma elevada densidade de buracos perto das mesmas, o que pode ser prejudicial para o desempenho das células solares. Para fabricar células solares completas, uma camada *buffer* de *CdS* foi depositada por *CBD*, e uma dupla camada de *i-ZnO/ZnO:Al* foi depositada por *sputtering*. Uma eficiência máxima de 8.4% foi atingida para uma temperatura de deposição de 450 °C. As curvas *I-V* das células solares depositadas a 500 °C revelaram um comportamento de vazamento de corrente em polarização reversa, possivelmente devido à presença de buracos perto das fronteiras de grão, ou devido à presença da fase *Copper-Selenide* em regiões mais profundas da camada *CIGSe*, que não são atingidas pela solução de *KCN*. Uma eficiência média de 3.4% foi obtida para células solares depositadas a 500 °C.

Numa segunda abordagem, o excesso de Cobre foi consumido através de uma pós-deposição de Índio, evitando assim a necessidade do uso da solução de *KCN*. Uma temperatura de 500 °C foi selecionada para tais deposições. Devido ao excesso de Índio fornecido, as camadas de CIGSe apresentam um rácio de [Ga]/([Ga]+[In]) (GGI) inferior ao apresentado pelas amostras subtidas ao processo de *KCN*. A pós-deposição de Índio resulta em filmes com fronteiras de grão menos pronunciadas e uma densidade inferior de buracos. As células solares apresentaram um aumento significativo de eficiência, sendo atingida uma média de 6.1%, quando em comparação com os 3.4% obtidos na experiência de KCN.

Palavras chave: CIGSe, Índio, KCN, Pós-deposição

INDEX

FIGURE INDEX

TABLE INDEX

List of Abbreviations, initials and acronyms

PV - Photovoltaic

UV - Ultra-violet

I - Irradiance

W - Watt

m - Meter

AM - Air mass

SC - Semiconductors

VB - Valence band

CB – Conduction band

$\overrightarrow{E_0}$ - Built-in electric field

V_{bi} - Built-in potential

N_A - Acceptor impurity concentration

N_D - Donor impurity concentration

k_B - Boltzmann constant

T - Temperature

T_{SUB} - Substrate temperature

n_i - Intrinsic carrier concentration

h - Planck's constant

c - Speed of light in vacuum

I - Total current

I_{ph} - Photo-generated current

I_{mp} - Current at maximum power point

V_{mp} - Voltage at maximum power point

η - Efficiency

FF - Fill factor

P_{in} - Input solar power radiation

Mo - Molybdenum

Na - Sodium

Cu - Copper

In - Indium

Ga - Galium

Se - Selenium

SLG - Soda-lime glass

nm - Nanometer

CdS - Cadmium sulfide

CBD - Chemical bath deposition

SEM - Surface Electron Microscope

SE - Secondary electrons

BSE - Backscattered electrons

RF - Radio frequency

ZnO - Zinc Oxide

i-ZnO - Intrinsic Zinc Oxide

ZnO:Al - Zinc Oxide doped with aluminum

STAR - Sputtering Advanced System for Research

DC - Direct Current

RF - Radiofrequency

ms - Microseconds

mbar - Milibar

sccm - Standard cubic centimeters per minute

PVD - Physical vapor deposition

KCN - Potassium cyanide

GBs - Grain boundaries

INL - International Iberian Nanotechnology Laboratory

1. INTRODUCTION

The global increase in energy demand and environmental pollution is motivating research and technological investments, as the industry is looking for an environmentally friendly source of energy. Solar energy is the most abundant, effective, and eco-friendly source of renewable energy. In the initial stages, photovoltaic systems energy generation was not reliable, as the photovoltaic systems had short lifetimes. However, through development, the lifecycle of PV systems has increased to 20-25 years, as they become one of the most promising sources of energy to be deployed on a large scale.

There are several approaches to create solar panels, where different materials and technologies, which can have a profound impact on the amount of energy generated and its cost, are used. The cost of solar power has been dropping dramatically over the past decade and, simultaneously, the photovoltaic efficiency has been rising [1]. At present, commercially available solar panels are dominated by first and second generations cells. First-generation cells, which occupy around 92% of the photovoltaic market [2], are made of crystalline Silicon, and absorber layers show thicknesses above 100μm. Si-cells require complex and expensive manufacturing processes, due to its high absorber layer thickness and high thermal budget, as temperatures of 1100°C are needed for its production. Power conversion efficiencies of 26.7% have been reached for c-Si solar cells [3].

An alternative to the first-generation cells is thin-film solar cells such as $Cu(In,Ga)Se_2$ (CIGSe) and CdTe, commonly referred to as second-generation solar cells. The difficult disposal and high toxicity of Cadmium present big issues in the large-scale commercialization of Cadmium Telluride solar cells. CIGSe solar cells are the most promising alternative to silicon solar cells due to their lower manufacturing cost, reduced use of material (absorber layers only require a thickness of 1-2μm), and comparable efficiencies (CIGSe have reached a record efficiency of 23.35% [4]). CIGSe layers are prepared by reactive co-evaporation [5], selenization of metallic or compound precursors [6], reactive co-sputtering [7], and non-vacuum techniques [8],[9].

In the present work, the fabrication of thin-film $Cu(In,Ga)Se_2$ solar cells will be conducted in STAR (**S**pu**T**tering for **A**dvanced **R**esearch), a system capable of manufacturing complete solar cells in situ, under vacuum. The main focus of this thesis is the optimization of the properties of the absorber layer. CIGSe layer were grown with a Copper-rich Cu-In-Ga sputtering target, with a simultaneous supply of selenium via a pulsed valve-cracker evaporation source.

The specific objectives of the Master thesis leading to this dissertation were the following significant topics:

- Study and development of an introductory literature review on the basics of photovoltaic technology and $Cu(In,Ga)Se_2$ solar cells properties.

- Familiarization with the STAR magnetron sputtering system, structural, optoelectronic, and device analysis techniques.

- Development of a suitable deposition process for the use of a $Cu(In,Ga)Se_2$ layer in photovoltaic devices

- Explore the effect of the stoichiometry of Copper-rich and Copper-poor Cu-In-Ga sputtering targets, and indium post-deposition on the properties of the CIGSe absorber and on the performance of the solar cells

The present dissertation is organized into seven chapters. The first chapter is the Introduction, describing the motivation, objectives, and addressing the main challenges of this work. The second chapter gives an overall review of the working principles of solar cells, to allow a better interpretation of the obtained results, and the CIGSe solar cell structure is explained in detail. The following chapter introduces all experimental techniques, namely the sputtering setup and characterization methods used to evaluate the produced films. Chapter 4 presents the calibrations that were performed before the fabrication of the devices. For the deposition of the CIGSe layers, a Cu-In-Ga target with a high Copper atomic percentage was used, which leads to the formation of undesired $Cu_{2-x}Se$ phases. To eliminate this undesired phase, two different approaches were studied: KCN-etching, where the Copper-Selenide phase is etched with the KCN solution, and an Indium-Selenide post-deposition, where the interdiffusion of Indium throughout the absorber layers balances the Copper stoichiometry, thus removing the $Cu_{2-x}Se$ phase. Chapter 5 describes the results of KCN chemical etching on the properties of CIGSe films and complete solar cell devices, prepared at different deposition temperatures. Chapter 6 then describes the results for the Indium-Selenide post-deposition approach, including a comparison with the results for the KCN etching. Finally, Chapter 7 summarizes the results, discusses the main conclusions of the dissertation, and suggests some topics to be developed as future work.

2. WORKING PRINCIPALS OF SOLAR CELLS

2.1 Solar spectrum

The sunlight is Earth's most abundant resource for renewable energy conversion [10], thus understanding how its energy is distributed is fundamental. It radiates energy in the form of electromagnetic radiation. The solar radiation spectrum closely matches that of a black body radiator at approximately 5800K, as evident in Figure 1. The average irradiance above the Earth's atmosphere is I=1366 W/m^2 [11], and is represented by the Air Mass (AM) 0 spectrum (yellow part in Fig. 1). The AM 0 spectrum is important when dealing with solar energy harvesting in outer space (e.g. solar panels in satellites). Unlike the broad and uniform spectrum outside the atmosphere, the solar radiation that reaches Earth's surface suffers several phenomena of diffraction and absorption changing its spectral distribution and irradiation significantly. The average irradiation, on a clear day, is approximately I=1000 W/m^2 [12]. The terrestrial solar radiation is described by the AM 1.5 spectrum (red part in Figure 1). Additionally, the solar energy distribution is dependent on the time of the day, season, latitude, elevation above sea level, angle of the sun, among others.

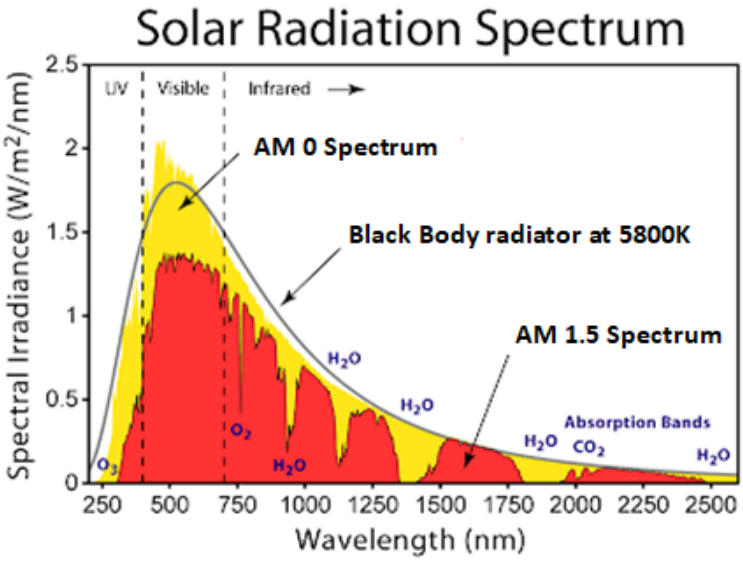

Figure 1. Solar irradiance above Earth's atmosphere (AM 0 spectrum) and at Sea Level (AM 1.5 spectrum). Image adapted from [13].

2.2 Introduction to semiconductors

2.2.1 Semiconductors and their doping

Modern solar cells base their operation on the properties of semiconductor materials as the light absorption layer [14]. Semiconductors can arrange themselves in a crystalline, polycrystalline (i.e. composed of several crystallites or small crystals), or amorphous form. Both crystalline and polycrystalline type semiconductors possess periodic and organized lattice structure, in contrast to amorphous semiconductors, which possesses no long-range lattice structure periodicity.

In semiconductors, electrons can either be in the valence band (VB) or conduction band (CB). These bands are separated by a bandgap, which is a forbidden energy range where there are no electronic energy levels. If an electron has enough energy, it can transit from the VB to the CB, and an electron-hole pair is created. Semiconductors can be classified as direct or indirect bandgap semiconductors. For a direct bandgap semiconductor, the top of the VB and the bottom of the CB occur at the same momentum. In an indirect bandgap semiconductor, the top of the VB and the bottom of the CB occur at different momentums. This implies that the electronic transition of an electron or hole from the CB to the VB, or vice-versa, requires the absorption or emission of a phonon for the conservation of momentum. The necessity of a simultaneous photon-phonon interaction in indirect bandgap semiconductors leads to a small absorption coefficient α, in comparison with direct bandgap semiconductors [15].

To improve a semiconductor's electronic properties, it is common to purposely introduce impurities into its lattices [16]. This phenomenon is called doping. For group IV semiconductors, the most common doping method consists of replacing some of its atoms with elements typically from group III or V. For example, in the case of the semiconductor Si, there are two doping types: n-type (introducing dopants from group V) and p-type (introducing dopants from group III). Group V impurities, also referred to as donor impurities, create local energy levels just below the CB and donate a free electron to the CB, increasing the free electron density. The Fermi level is shifted towards the CB. On the other hand, group III impurities, also referred to as acceptor impurities, have one less electron than the host semiconductor (Si), creating local energy levels just above the VB, increasing the density of holes. In this case, the Fermi level lies closer to the VB. In both cases, the conductivity of the material is increased.

2.2.2 Photovoltaic effect

The photovoltaic effect was discovered in 1839 by Alexandre Edmond Becquerel, and was later described by Albert Einstein in 1904 [17]. Becquerel observed that when specific materials are set under illumination their conductivity increases. This phenomenon involves the production of electron-hole pairs in a semiconductor due to the energy of the incident photons, and the subsequent collection of the generated carriers at opposite contacts [18]. The photovoltaic effect occurs, in its simplest form, when photons with energy equal or higher than the semiconductor bandgap are absorbed. The photon energy E_{ph} is related to the wavelength λ of the light, as evidenced by the following equation:

$$E_{ph} = \frac{hc}{\lambda}, \tag{1}$$

where h is the Planck's constant, and c is the speed of light in vacuum. The photovoltaic effect is the most important working principle of a solar cell since its operation is based on the conversion of absorbed sunlight into electricity.

2.2.3 Recombination processes

Due to external factors, such as temperature or light absorption, semiconductors are disturbed from the equilibrium state and additional charge carriers are created. The system will naturally fall back into equilibrium, as electrons and holes annihilate each other (i.e. an electron in the CB stabilizes back down into the VB and neutralizes a hole). Such a mechanism is called recombination. The energy in this process is released either as a photon, phonons, or it is transferred to a third particle. There are three types of recombination, which can be seen in Figure 2: Band-to-band recombination, Auger recombination, and Shockley-Read-Hall (SRH) recombination.

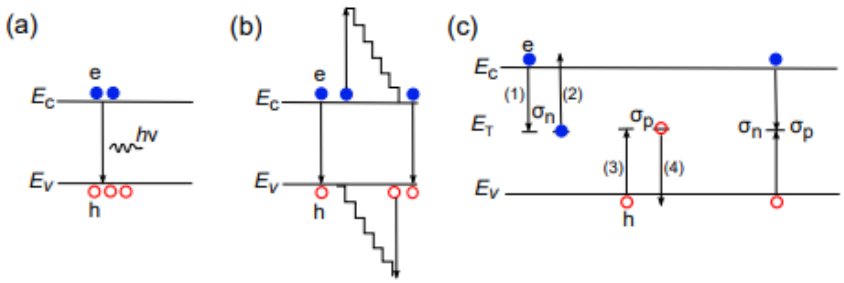

Figure 2. Recombination mechanisms in semiconductors. (a) Band-to-band recombination. (b) Auger recombination (c) Shockley-Read-Hall recombination. [19]

Band-to-band recombination, also known as radiative recombination, occurs when the excess energy is emitted as a photon. This process is the exact inverse of the absorption mechanism and is predominantly found in direct bandgap semiconductors. Several devices, such as laser diodes, base their operation on the radiative recombination phenomenon.

Auger recombination is a non-radiative process that requires three charge carriers. The excess energy of an electron-hole pair recombination is transferred to either an electron or a hole that is subsequently excited to higher energy levels [20]. Auger is the dominant recombination mechanism in indirect bandgap semiconductors and is strongly dependent on the doping concentration [21].

The inevitably formed defects in the lattice of semiconductors result in additional electronic states with energy E_T inside the bandgap, known as traps [22]. Traps can either capture or re-emit charge carriers and work as recombination centers. Such recombination is referred to as Shockley-Read-Hall recombination. The energy released in each transition is emitted as a phonon. The rate at which SRH recombination occurs is dependent on the difference in energy of the introduced trap levels to the CB and VB edges. Trap energy levels closer to the mid of the bandgap are very effective for recombination, so they are undesired in solar cells.

2.2.4 PN Junction

When p-type and n-type semiconductors come into contact a PN-junction is formed. Just as they are first joined together, a large carrier gradient exists between both sides of the junction. In agreeance with Fick's law [23], as the charge carriers diffuse to the opposite region (electrons to the p zone, and holes to the n zone), driven by the concentration gradient, they recombine with their respective opposite charges, forming a region with a low concentration of electrons and holes of width W, known as the depletion zone or space-charge region. An electric field $\overrightarrow{E_0}$ pointing from the n-type region to the p-type region is present in the depletion zone. The integration of this electric field is called built-in potential V_{bi} and is given by the following equation:

$$V_{bi} = \frac{k_B T}{e} \ln\left(\frac{N_A N_D}{n_i^2}\right), \tag{2}$$

where k_B is the Boltzmann constant, T is the temperature, N_D is the donor impurity concentration on the n-side, N_A is the acceptor impurity concentration on the p-side, and n_i is the intrinsic carrier concentration. This potential difference produces a bending of the energy bands, as shown in Figure 3. Additionally, the Fermi level of both extrinsic regions will be aligned.

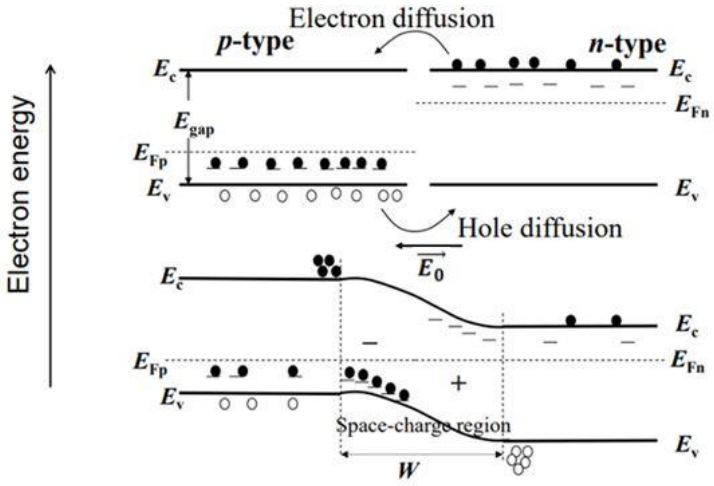

Figure 3. Representation of the PN (homo)junction in equilibrium. E_{Fn} and E_{Fp} are the Fermi energy levels of the n-type and p-type zones, respectively. Image adapted from [24].

From now on let us assume that the circuit is closed, so that a current flow is possible. If additional electron-hole pairs are generated due to external factors (e.g. temperature or photovoltaic effect) the built-in electric field $\overrightarrow{E_0}$ pulls the excited electrons towards the n-type zone and the holes towards the p-type zone, minimizing their recombination rate. This phenomenon creates a drift current in a direction opposite to that of the diffusion current and is responsible for the solar energy harvesting in solar cells.

Carriers formed outside the depletion zone, have a lower probability of being collected and contributing to the photocurrent due to recombination [25]. It is necessary that the diffusion length of the minority carries is large enough so that the light-absorption generated carriers can reach the contacts without recombining. For this reason, in the solar cell industry, absorption layers are typically p-type semiconductors, as they allow a better collection probability [26].

2.2.5 Heterojunctions

A heterojunction is a junction formed by two different semiconductors. Heterostructures offer extra degrees of freedom since the use of materials with different bandgaps and refractive indices, increases the flexibility of semiconductor device designs, which can increase their performance [27]. Heterojunctions can be classified as isotype (i.e. both semiconductors have the same doping type) or anisotype heterojunctions (i.e. one of the semiconductor is p-doped, and the other is n-doped). For the case of study, anisotype heterojunctions are of interest. In Figure 4, the energy band of such a heterojunction is represented.

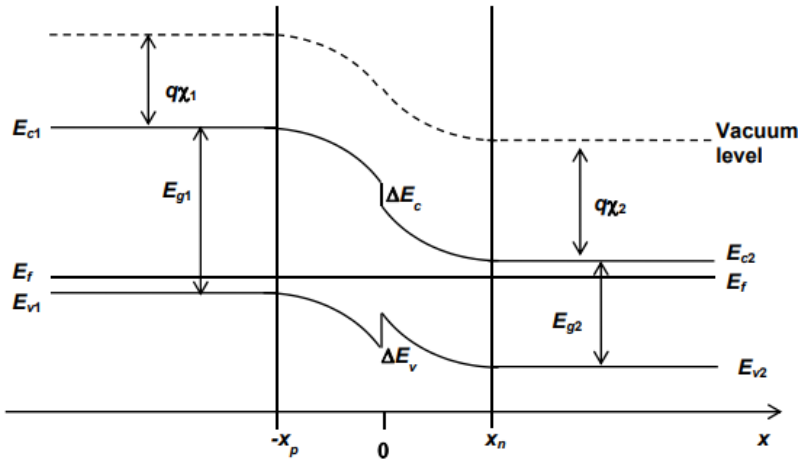

Figure 4. Energy band representation of a PN heterojunction [28]

It can be seen that there is a discontinuity in both valence and conduction bands, which is a consequence of the inherently different properties of the used semiconductors (e.g. bandgap and electron affinity). These discontinuities are the most important parameter in a heterojunction device, as they determine the optical and transport properties of the device [29].

In the solar cell industry, these discontinuities are engineered in a way that the n-type layer has a large bandgap, allowing the passage of most of the solar radiation. On the other hand, the absorber layer, which is typically p-type, has a narrow bandgap to absorb most of the received solar radiation. Occasionally, resulting from the lattice misalignment of the different semiconductors used in the junction, trap states might be formed. These states increase the recombination rate of the photogenerated carriers [30], lowering the photocurrent and reducing solar cell efficiency. The correct choice of semiconductors is, therefore, one of the most important challenges in heterojunction solar cells.

2.3 Electronic characteristics of solar cells

2.3.1 Current-voltage characteristics

For an ideal solar cell, the total current under illumination I is given by the sum of the dark current (equal to the diode current) and the photo-generated current I_{ph}:

$$I = I_0 \left(e^{\frac{qV}{k_B T}} - 1 \right) - I_{ph} \tag{3}$$

When classifying the PV characteristics of a solar cell, 3 parameters are of importance:

- Short-circuit current, I_{SC}: current through the solar cell when the voltage across it is zero (i.e. when the solar cell is short-circuited)

- Open-circuit voltage, V_{OC}: maximum voltage that can be delivered by the solar cell and occurs when the net current through the device is zero. It can be calculated from Eq. (3) by putting $I = 0$:

$$V_{OC} = \frac{k_B T}{q} \ln\left(\frac{I_{ph}}{I_0} + 1\right) \quad (4)$$

- Maximum power point of the current-voltage curve, P_{max}: It is the operating point at which the solar cell is delivering its maximum power and is given by the product of both current and voltage at maximum power point (I_{mp},V_{mp}):

$$P_{max} = V_{mp} I_{mp} \quad (5)$$

Once the parameters described above are determined, one can easily evaluate the solar cell's performance. The solar cell conversion efficiency η is used to compare the performance of solar cells. It is the ratio between the output power from the cell and the input solar radiation power:

$$\eta = \frac{P_{max}}{P_{in}} \quad (6)$$

Another useful specification of solar cells is the fill factor (FF). FF is defined as the ratio between the maximum power generated by the solar cell and the theoretical power, given by the product of V_{OC} and I_{SC}:

$$FF = \frac{P_{max}}{V_{OC} I_{SC}} \quad (7)$$

Figure 5 shows the typical I-V curve of a solar cell in dark and in illumination.

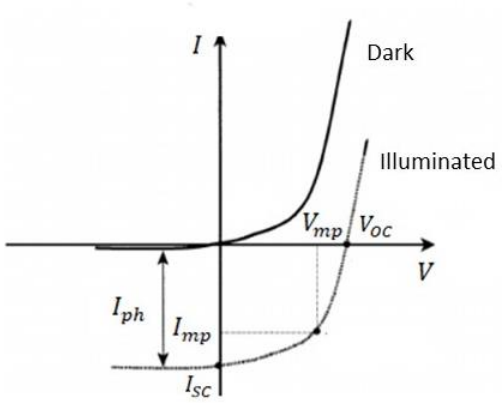

Figure 5. I-V characteristic of a solar cell. Image adapted from [31].

2.3.2 Equivalent circuit of a solar cell

The equivalent circuit of an ideal solar cell, from which Eq. (3) can be determined, can be modeled as a current source I_{ph} in parallel with a diode, connect to an external load R_L, as indicated in Figure 6a. However, a real solar cell has further ohmic resistances due to manufacturing defects during the PV cell production, that create additional current paths for the generated current. Such resistances can be divided into two groups: shunt resistance R_{sh}, and series resistance R_s. The equivalent circuit of a real solar cell is indicated in Figure 6b.

The magnitude of the shunt resistance is influenced by point defects in the p-n junction, leaking currents, e.g. along the edges of the solar cell, and impurities in the semiconductor lattice. Ideally, this resistance should be as high as possible. According to Kirchhoff's current law, low R_{sh} would create an additional parasitic current path, reducing the overall current captured by R_L. The series resistance is influenced by the contact resistance of the metal-semiconductor interface, ohmic resistance in the metal contacts and semiconductors materials. When manufacturing solar cells, one aims at minimizing the R_s value. [32]. High R_s would act as an obstacle to the current passage, in compliance with Ohm's law. The influence of parasitic resistance in the I-V curve of a PV cell can be seen in Figure 7.

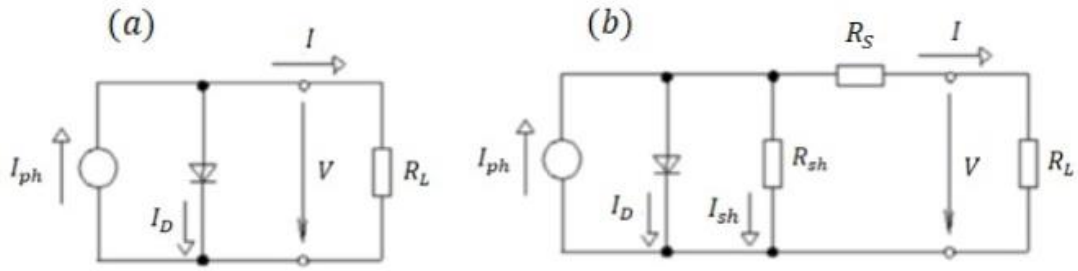

Figure 6. The equivalent circuit of (a) an ideal and (b) a real solar cell. Image adapted from [15].

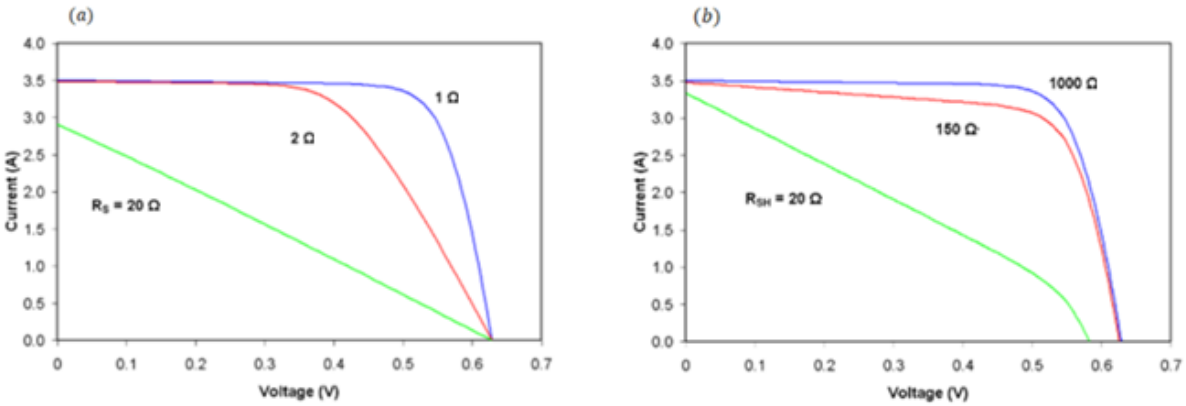

Figure 7. (a) Effect of the series resistance in the I-V curve of a solar cell. (b) Effect of the shunt resistance on the I-V curve of a solar cell [33].

2.3.3 Loss-of-efficiency mechanisms

Several factors reduce the efficiency of a solar cell. The different loss mechanisms can be divided into two types: optical and electrical losses. Optical losses are due to the reflection of light on different surfaces, non-absorbed light, and the shadowing effect. Antireflective coatings are typically used to reduce the reflection at the solar cell surface. To increase the percentage of absorbed light, a reflecting metal is used on the back of the cell. This allows the reflection of light that passed through the solar cell back into it, thus increasing the absorption probability. Electrical losses are strongly influenced by recombination processes and manufacturing defects that result in undesired parasitic resistances.

2.4 Cu(In,Ga)Se_2 solar cells

In general, thin-film solar cells are composed of the following layers (Fig. 8): substrate, back contact, absorption layer, buffer layer, transparent conductive oxide (TCO), and an antireflective (ARC) layer.

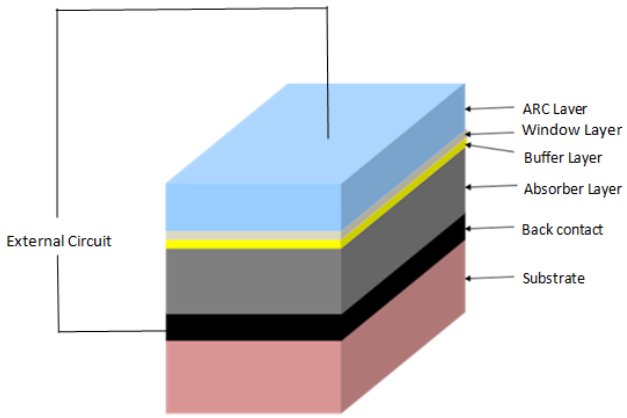

Figure 8. Typical structure of heterojunction solar cells. Image adapted from [34].

A typical Cu(In,Ga)Se_2 (CIGSe) solar cell is composed of the following layers: Molybdenum back contact, Cu(In,Ga)Se_2 absorber layer, Cadmium-Sulfide buffer layer, and an intrinsic and Aluminum-doped Zinc-Oxide window layer. The role of each layer will be discussed in more detail in the following sub-chapters. Figure 9 shows a cross-section of a CIGSe solar cell as well as the typical thickness of each layer.

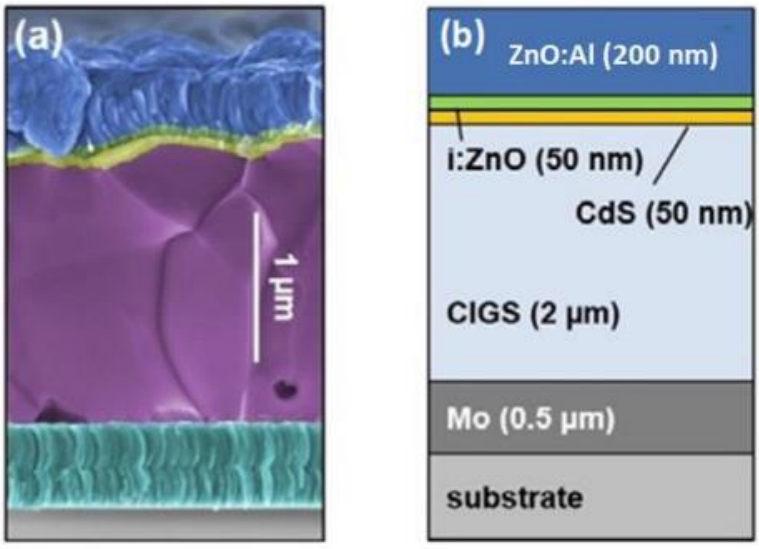

Figure 9. (a) Colored SEM image of a CIGSe cross-section. (b) Schematic of the standard structure of CIGSe solar cell [35]

One important parameter leading to high-efficiency solar cells is an appropriation of the conduction band offset (CBO) of the CIGSe/CdS/Window layers. Figure 10 shows the energy diagram of a typical CIGSe solar cell. The CdS/CIGSe system shows a small spike-like CBO, where the conduction band of the CdS buffer layer is at a higher energy level in comparison with that of the CIGSe layer, but the generated electron current can easily overstep it, meaning that there is no potential barrier blocking the passage of the photo-generated charges [36] , thus it is not harmful for the cell performance.

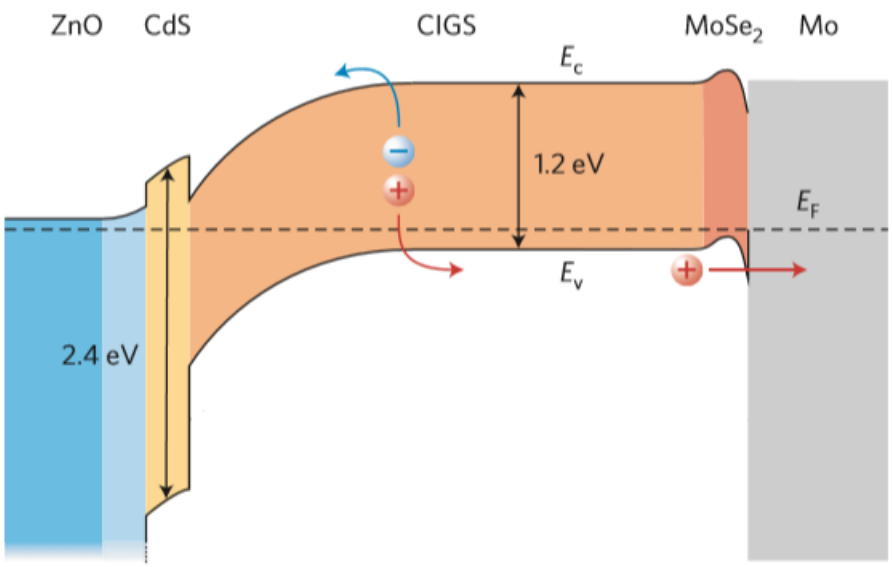

Figure 10. Energy band diagram of a CIGSe solar cell [37]

The fabrication of $Cu(In,Ga)Se_2$ solar cells is conducted at a wide range of temperatures, varying from room temperature to 600°C, so the coefficient of thermal expansion (CTE) of the different layers should be similar to avoid adhesion problems and crack formation during the deposition of the different layers, especially at higher temperatures.

2.4.1 Soda-lime Glass and Flexible Substrates

Soda-lime glass (SLG) substrate is a rigid flat substrate (allowing a conformal growth of the layers deposited on its surface) widely used in CIGSe solar cells. SLG supplies a necessary amount of Na, fundamental for increasing the absorber layer performance. This effect will be discussed in the next section. Also, SLG is light, shows good adhesion to the regularly used Mo back contact, and can withstand up to about 530 °C [38].

Another interesting approach is the production of flexible photovoltaics, which are particularly interesting for uneven surface applications. SLG is a rigid substrate, so it cannot be used as a flexible substrate. Metals and polymers are the most promising candidates for flexible photovoltaic cells [39]. The use of metals requires a dielectric layer to provide electrical insulation between the substrate and the Mo back contact, which can increase production cost. Also, they have high surface roughness, so an additional polishing process is necessary. Polymers, on the other hand, have much lower density and surface roughness than metals and have insulating properties.

Usually, both metals and polymers are Na-free, so an external addition of Sodium is required. This can be done by depositing a layer containing Na (e.g. NaF layer [2]) before the deposition of the CIGSe layer. From a process point of view, the necessity of such a layer can be a disadvantage. However, it can be an advantage in terms of homogeneity and reproducibility.

2.4.2 Molybdenum Back Contact

An efficient solar cell back contact should meet the following requirements: low recombination rate for the minority carriers and low resistivity, high reflectivity in the visible spectrum, good adhesion to the substrate, should be chemically inert with the material deposited on top, and have similar thermal expansion coefficients.

In CIGSe PV technology, Molybdenum is the most commonly used material for the back contact since it fulfills most of the above requirements. Despite this, producing a Mo thin film that shows, simultaneously, low resistivity and good adhesion to a substrate is difficult to achieve. Usually, for low resistivity films, poor adhesion is observed, and vice-versa [40]. For flexible CIGSe photovoltaics, good adhesion between the Mo layer and the absorber layer is essential, since the CIGSe/Mo interface needs to withstand stress induced by bending of the module without cracking or delamination [39].

Previous studies [40],[41] showed that the most adequate method for Mo deposition is to use a Mo bilayer, obtainable by doing a 2-step sputtering process at different pressures, where the intended Mo properties could be achieved. Higher pressure deposition gives the Mo layer good adhesion to the substrate. Therefore, this layer is used as the bottom Mo layer. Lower pressure deposition causes the film to form with compressive stress, reducing its resistivity. Thus, the lower pressure Mo layer is sputtered following the deposition of higher-pressure Mo films. Another Molybdenum advantage is that it doesn't react with Ga, In, or Cu, but it reacts with Se, forming, under the influence of temperature, a $MoSe_2$ interface layer [42] that brings some benefits to the solar cell performance. If no $MoSe_2$ interface

layer is established, the CIGSe/Mo interface will form a Schottky contact, which brings substantial problems due to resistive losses, that arise from the Schottky barrier [43]. However, the presence of a $MoSe_2$ thin layer acts as a hetero-contact and causes a favorable ohmic contact between the Mo and CIGSe layers. The I-V characteristics of a solar cell are significantly improved, as its's efficiency can increase up to 5% in the presence of a $MoSe_2$ interface [42]. Furthermore, Mo thin films allow the diffusion of Na by thermal activation [2], increasing the carrier concentration of the p-type absorber layer [44]. The main disadvantage of using a Mo layer as the back contact is that its average reflectivity in the visible spectrum is inferior to 0.4% [45], which is much lower than the desired values.

2.4.3 $Cu(In,Ga)Se_2$ Absorber Layer

The absorber layer is the most fundamental layer of a solar cell, as it is responsible for absorbing the incident sunlight and creating excess charge carriers, which participate in the photocurrent. In the case of CIGSe solar cells, the absorber layer is a p-type polycrystalline compound constituted by Copper, Indium, Gallium, and Selenium, $Cu(In,Ga)Se_2$. It is a direct bandgap semiconductor (with a significantly thinner absorption layer it can reach similar absorption coefficients to those obtained by indirect bandgap semiconductors, such as Silicon) whose bandgap can be tuned by varying the stoichiometry of the compound. The chalcopyrite unit cell structure is based on two overlapped anion and cation lattices, that form a face-centered tetragonal structure (Figure 11). The lattice parameters can be calculated with the following equation:

$$\frac{1}{d^2} = \frac{h^2+k^2}{a^2} + \frac{l^2}{c^2} \tag{8}$$

where a and c are the lattice parameters, and d is the interplanar spacing of the (hkl) peak.

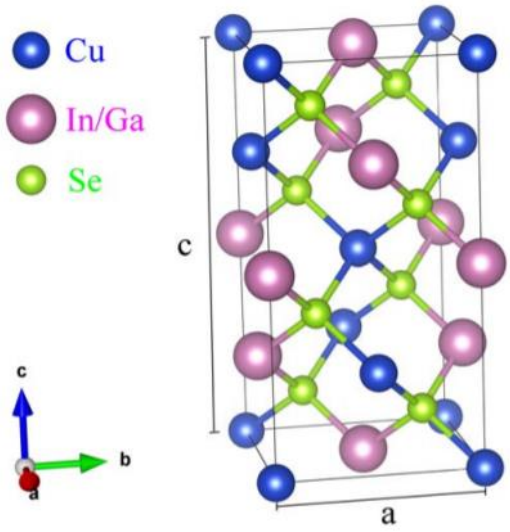

Figure 11. The unit cell of chalcopyrite Cu(In,Ga)Se_2 [46]. *Each Se atom is the center of a tetrahedral bond with 2 Cu and 2 group III atoms.*

The composition of the CIGSe absorber layer is fundamental to its properties, so a deposition process that easily allows controlling the stoichiometry of the film is crucial. Due to the increasing research interest in this chalcogenide material, ideal values for its composition have already been set. $CuInSe_2$ and $CuGaSe_2$, the materials that form the Cu(In,Ga)Se_2 alloy, belong to the semiconducting I-III-VI_2 groups [47].

Figure 12 shows the complex phase diagram of $CuInSe_2$. By varying the temperature and Cu percentage, four different phases are found: the α phase ($CuInSe_2$), the β phase ($CuIn_3Se_5$), the δ (high-temperature sphalerite) phase, and the Cu_2Se phase. When depositing CIGSe layer, the desired phase is the α phase. The α phase exists in a range of Cu content between 22 and 25%, depending on the temperature. From the phase diagram, it can be seen that growth at lower temperatures requires better control of the Cu content, since the width of percentages that allow the formation of the α phase is very narrow. The formation of a Cu_2Se phase for high Cu content must be avoided since it acts as a degenerate p-type semiconductor [48] and is detrimental for solar cell performance. Thus, CIGSe typically has a Cu-poor composition, meaning the final Cu percentage is below 25%. The benefit of such Copper deficiency is that Cu vacancies are formed throughout the thin film, acting as acceptor impurities.

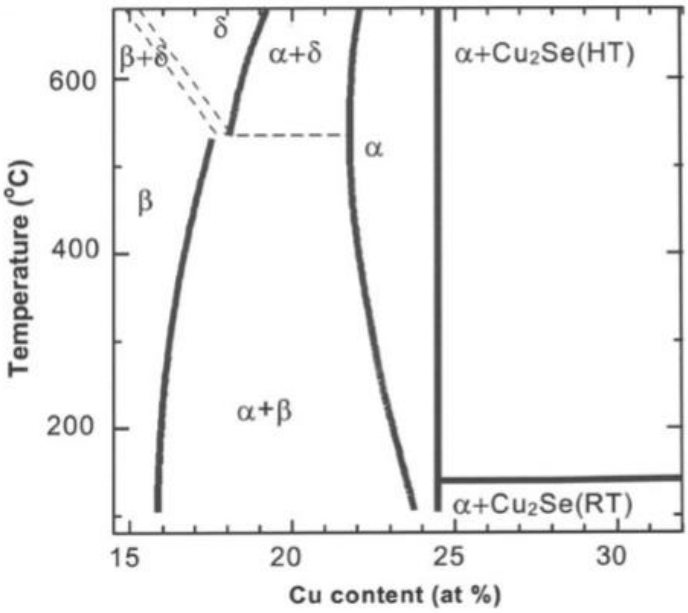

Figure 12. Pseudo-binary cut of the ternary phase diagram, comprising all Cu-In-Se compounds for different Cu percentages and temperatures. [47]

An important parameter of an absorber layer is the optical bandgap. The theoretical analysis concluded that a bandgap between 1.4 and 1.5 eV is ideal to achieve the maximum efficiency possible [49], [50]. However, it has been experimentally observed [51] that, for the CIGSe absorber layer, problems associated with bandgaps (such as recombination at the CdS/CIGSe interface due to discontinuity in the CIGSe CB) within the above-mentioned values will arise and the efficiency of the cell is significantly reduced. Defect states increased recombination, and band discontinuities are consequences of high bandgap CIGSe absorber layers [2]. Energy bandgap values between 1.1 and 1.2 eV were used in the production of world record CIGSe solar cells [52]. The value of bandgap (E_G) depends on the [Ga]/([Ga]+[In]) (GGI) ratio. The bandgap can vary from 1.0 eV for pure $CuInSe_2$, to 1.7eV, for pure $CuGaSe_2$ [53]. The bandgap dependence on the GGI ratio is given by the following equation [54]:

$$E_G(x)[eV] = E_G^{CGS} * x + E_G^{CIS} * (1 - x) - b * x * (1 - x), \quad (9)$$

where x is the GGI ratio, E_G^{CGS}=1.68eV, E_G^{CIS}=1.03eV, and b is the optical bowing constant (at room temperature, b=0.12). Additionally, some studies demonstrated that a decrease in the Cu percentage can cause an increase in bandgap energy [55].To obtain high-efficiency solar cells the [Ga]/([Ga]+[In]) and [Cu]/([Ga]+[In]) (CGI) ratios should be between [0.2-0.3] and [0.75-0.95] respectively. If the [Ga]/([Ga]+[In]) ratio exceeds 0.3, meaning that the sample has a high concentration of Gallium, the

number of defects in the film increases, the absorption coefficient decreases, and the minority charge collection is reduced [51]. Gallium concentration can be varied to obtain the highest V_{oc} and efficiency possible. These aforementioned ratio values equate to the following approximate percentages of the different elements in the p-type absorber layer: Cu≈25%, In≈17.5%, Ga≈7.5% and Se≈50%. Furthermore, this layer should have an optimized thickness of around 2μm [56] and growth conditions should enhance grain growth.

It has been reported in the literature that a small supply of Sodium (about 0.1% atomic percentage) to the absorber layer can be extremely beneficial for its performance [57]. The source of Na can be either the substrate or a sodium-containing layer deposited on it. The incorporation of Na in the absorber layer passivates the defects in the CIGSe/CdS junction, affects the grain size, and acts as a catalyst in the formation of the $MoSe_2$ layer, thereby increasing the open-circuit voltage and fill factor [58]. Despite its benefits, if the Sodium atomic percentage is too high, a Na_2Se_x layer can be formed, retarding the $MoSe_2$ formation, as fewer selenium atoms will be available to form the aforementioned layer.

2.4.4 CdS Buffer Layer

The best performing CIGSe solar cell fabricated so far used a Cadmium-Sulfide (CdS) thin film as a buffer layer [59]. CdS is the most commonly used buffer material in CIGSe fabrication, although new alternatives are being researched due to the toxicity inherent to Cd-containing materials. The goal is to find a Cd-free material that exceeds efficiencies of those obtained with CdS buffer layers [60].

CdS is a direct bandgap n-type semiconductor that forms the device's heterojunction with the absorber layer. It has a bandgap of 2.4 eV, so it absorbs high-energy photons (mainly within the blue range), preventing them to be absorbed in the p-type layer. This is a disadvantage because the photo-generated carriers in this layer do not contribute to the photocurrent, due to the low carrier life of the minority charge carriers. To minimize the absorption of this layer, CdS films have a low thickness, which also reduces the resistance introduced into the system. Ideal CdS layers have a thickness between 40 and 80 nm [2]. The main benefit of CdS is that it allows a good band alignment with the CIGSe band, which is a crucial factor to extract photo-generated carriers [61].

Chemical bath deposition (CBD) is the most commonly used method to make the CdS layer deposition [62]. With this technique, the defects at the Cu-poor surface of CIGSe are occupied and passivated by Cd atoms [37]. CBD depositions also offer a good CIGSe surface cover, lowering shunt paths and protecting the CIGSe layer from damage during the window layer deposition. Moreover, the CdS-CBD allows the

surface cleaning of the CIGSe layer surface due to the use of ammonium that enhances the performance of the CIGSe-CdS interface.

The main disadvantage of this deposition method is that it is a non-vacuum process, as opposed to the processes used for all other layers of CIGSe solar cells, which are deposited in a vacuum environment. Thus, the vacuum processing is interrupted which is not ideal.

2.4.5 ZnO Window Layer

A top contact of a solar cell should meet the following requirements: high transmissivity and negligible reflectivity, good electrical conductivity with minimal recombination losses, and minimal resistance introduced into the system. The solar spectrum is more intense in the visible and near-infrared regions, so an optimum top contact (also referred to as window layer) should be very transparent in these regions, implying a high bandgap E_G>3 eV is desired. To achieve good electrical conductivity, a low resistivity is necessary (10^{-3} Ω.cm or lower). Achieving high conductivity in thin layers can be a challenge, so it is common to n-dope the TCO layer, increasing the free carrier concentration and therefore its conductivity [63].

An intrinsic zinc oxide (i-ZnO) and aluminum-doped zinc oxide (ZnO:Al) double layer is commonly used as the top contact in high-efficiency CIGSe PV. Typically, the zinc oxide bilayer consists of a [50-100] nm thick high resistivity undoped ZnO layer and a [200-500] nm Aluminum-doped ZnO layer. The undoped layer prevents the diffusion of Aluminum impurities to the buffer layer [64], and reduces the influence of shunt currents, increasing the performance of the solar cell [65].

The highly-doped ZnO top layer has low resistivity and a bandgap of 3.3 eV, although this value changes accordingly with the aluminum doping. An aluminum weight percentage of [1.5-2]% has been shown to lead to the best window layer properties [66]. It is important to notice that, if the aluminum percentage is too high, contrary to what is expected, the bandgap can decrease, due to the Burstein-Moss shift effect, where the excessive introduction of doping levels creates a band edge by the dopant level [67]. Upon moisture exposure, an increase of resistivity of about one order of magnitude has been reported [2]. Thus, long-term stability can be a problem for CIGSe cells with a ZnO window layer, which is typically addressed by lamination with a top glass.

Several deposition techniques for the ZnO window layer have been tested and successfully employed: radiofrequency (RF) and DC magnetron sputtering [68], [69], chemical vapor deposition (CVD) [70], the sol-gel method [71], spray pyrolysis [72] and pulsed laser deposition [73]. Despite the wide variety of available methods, magnetron sputtering consistently achieved the best performing window layers.

3. EXPERIMENTAL TECHNIQUES

3.1 Basic Principles of Magnetron Sputtering

Magnetron Sputtering is a high-rate vacuum coating process that falls under the category of physical vapor deposition (PVD). It is commonly used for depositing metals, alloys, and compounds of a wide range of materials and is conducted in a high-vacuum environment. A gas inlet is used as a supply of inert gases (the most commonly used noble gas is Argon) and reactive gases, which will later form a plasma composed of neutral and ionized inert elements, electrons, and photons. An external energy source (e.g. RF, DC) is required to maintain the plasma active. Magnetron sputtering takes advantage of the magnetic field created by magnets to confine the accelerated free electrons in the magnetic trap, increasing the ionization efficiency of the Argon atoms. The Ar^+ ions are afterward attracted to the negatively biased charged target with high kinetic energies, which upon impact causes the erosion of the target and subsequent deposition in a substrate (Fig. 13).

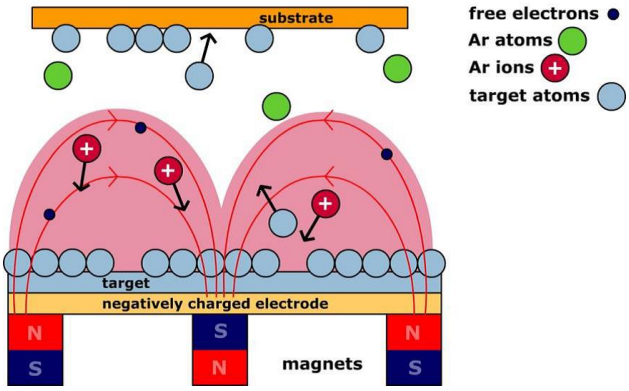

Figure 13. Schematic of magnetron sputtering process[74]

3.2 Sputtering Deposition system

The deposition system used in this project is STAR - **S**put**T**ering **A**dvanced System for **R**esearch, a deposition system developed by the Institute for Micro and Nanotechnology in Madrid and the International Iberian Nanotechnology Laboratory in Braga. Figure 14 shows a 3D-CAD design of STAR and a picture of the system used at INL. STAR consists of three independent vacuum chambers with the capability to fabricate, in-situ, a complete CIGSe solar cell, avoiding exposure of the CIGSe layer to air. Such exposure can be detrimental for solar cell performance [75]. Samples are transferred between the different chambers using a manually controlled transfer bar.

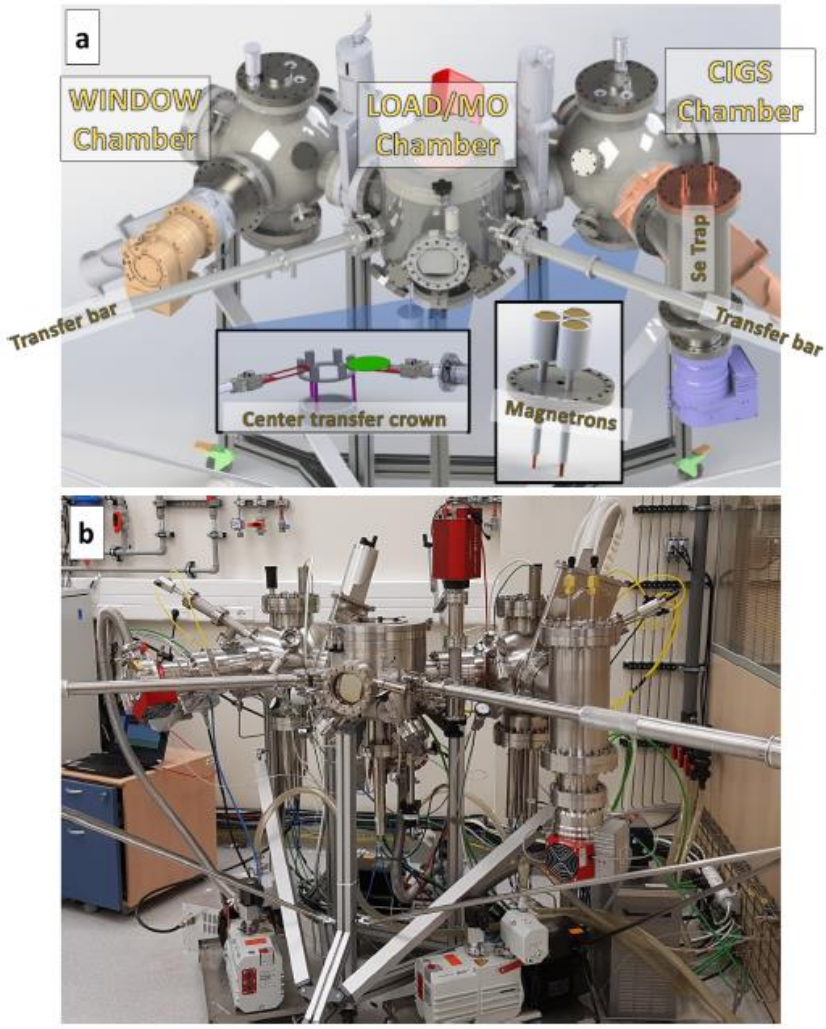

Figure 14. (a) 3D-CAD design of STAR system (b) Picture of the equipment used at INL facilities [76]

Each chamber has its pumping system (composed of a primary turbomolecular and secondary rotatory pump), pressure gauge, controlled N_2 and Argon input lines. Both Argon input lines and power supplies (current and voltage) are controlled via computer software. A revolver-like magnetron (Figure 15a) and a power supply (DC or radio-frequency (RF)) are used to create a magnetic field that bonds the plasma atoms/ions and enhances the ionization of the plasma, increasing, therefore, the sputtering efficiency. Operation in STAR is based around the central chamber, which acts as the sample loading and back contact deposition chamber. Samples are loaded on titanium sample holders, which are subsequently loaded into a substrate holder cassette (Figure 15b).

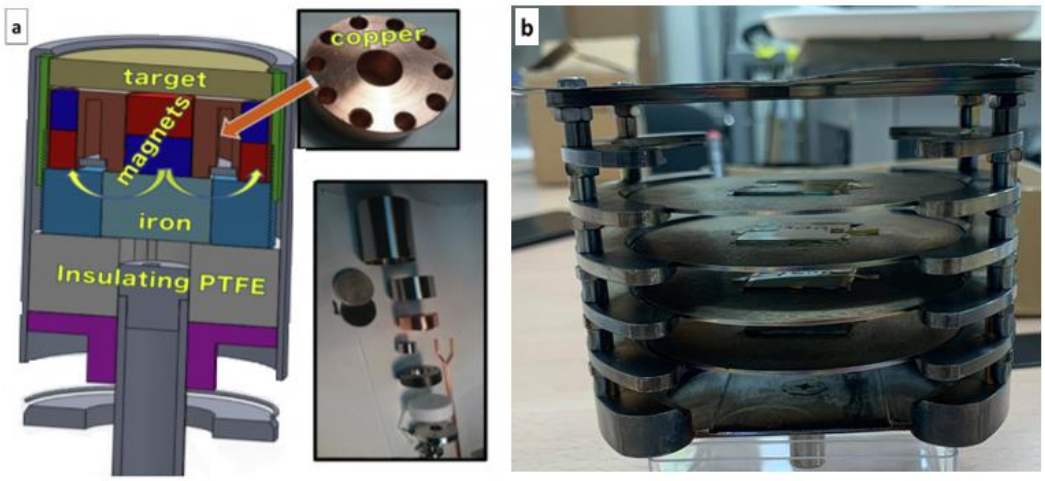

Figure 15. (a) 3D-CAD design of the cross-section of the magnetron sputtering [76] *(b) Picture of the substrate holder cassette and the Titanium substrate holders*

A 99.95% purity Molybdenum and a DC power supply are used for the Molybdenum deposition.

The window chamber is used for both the window and buffer layer depositions. This chamber has three RF powered magnetrons with three different targets: ZnO, ZnO:Al(2%), used for the window layer deposition, and a $Zn(O_{0.75}S_{0.25})$, used for the buffer layer deposition. Even though not interrupting the vacuum process is a big advantage of the STAR system, previously conducted studies showed that the highest solar cells efficiencies are obtained with a CdS buffer layer deposited via the CBD technique [76]. For this reason, in the present work, a CdS buffer layer will be deposited by CBD in a non-vacuum environment.

The $Cu(In,Ga)Se_2$ absorber layer is deposited in the CIGSe Chamber. This chamber has 3 DC powered magnetrons with three different targets: CIG, Indium, and Molybdenum. With STAR it is possible to conduct several different methods to make CIGSe depositions such as using a single target made of a Cu-In-Ga alloy, using three different targets (Cu, In, and $In_{1-x}Ga_x$), simultaneously, among others. Both specified methods resort to the use of a selenium valve-cracker source and a substrate heater, to conduct the deposition at the desired temperatures (temperatures up to 700°C can be achieved). The temperatures referred to in the practical chapters are the nominal temperatures. The real temperature values might be slightly higher than the nominal temperature. In the scope of this thesis, a $Cu_{0.6}In_{0.25}Ga_{0.15}$ alloy will be used. The Selenium reservoir (Se cell) is heated by a spiral filament to temperatures of 300°C, causing the Se sublimation. The sublimated Se gas is composed of large Se_n molecules, and it is beneficial to break them into smaller molecules. Following the Se sublimation, the

gas passes through a tantalum cracker heated up to 600°C, which breaks the large Se molecules into the desired Se_2 molecules. Figure 16 illustrates a 3D-CAD design of the selenium cell.

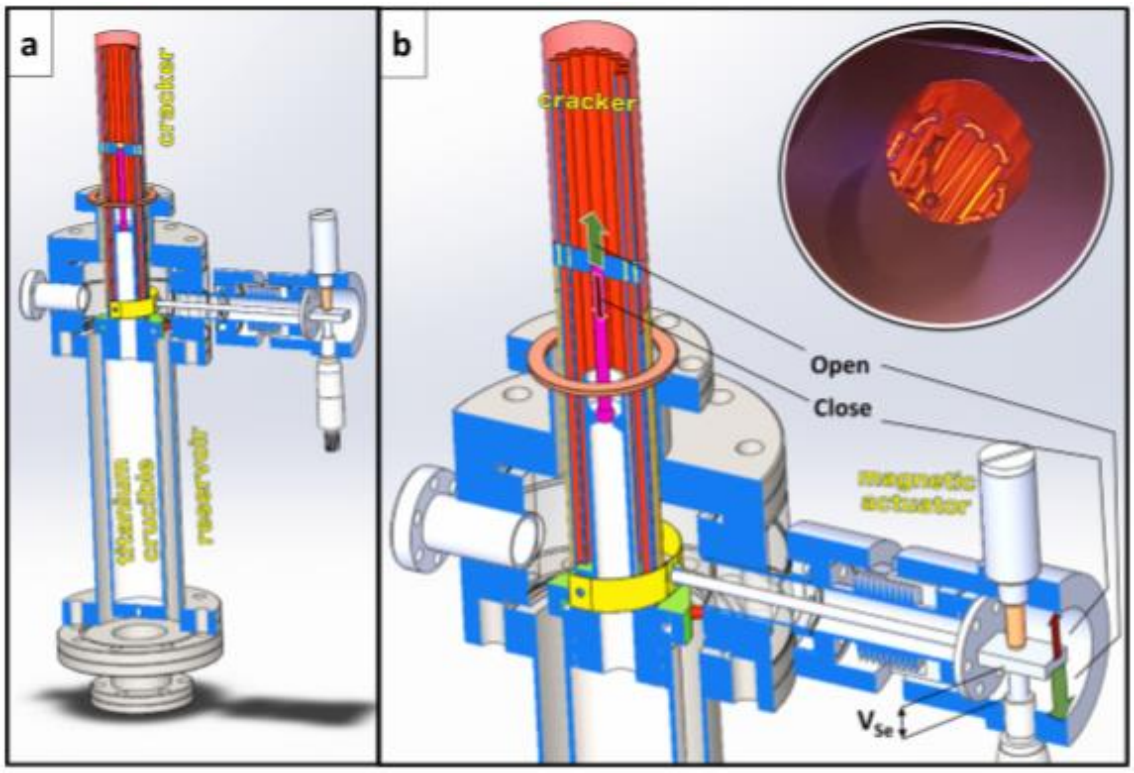

Figure 16. (a) 3D-CAD design of the entire selenium cell. (b) an enlarged drawing of the valve/cracker region. [76]

To precisely control the amount of selenium that passes to the CIGSe chamber and is subsequently deposited on the sample, an external valve and an open-and-close mechanism are used. The external valve opening is manually controlled with a high-accuracy micrometer screw. The valve opening can vary from 8-10 mm, where 10 mm is the maximum aperture, allowing the maximum passage of selenium to the chamber, and 8 mm is the minimum aperture. Finally, a software-controlled mechanism is used to close and open the line of selenium. This feature allows pulsed selenium evaporation, and pulses as short as 100 ms can be achieved. Figure 17 shows a graphic representation of this mechanism. When the valve is closed, the Se supply is completely shut off. When the valve is opened, the Se that was evaporated by the Se cell and broken into smaller molecules by the cracker is directed to the sample. Different pulses significantly change the amount of Se supplied to the sample.

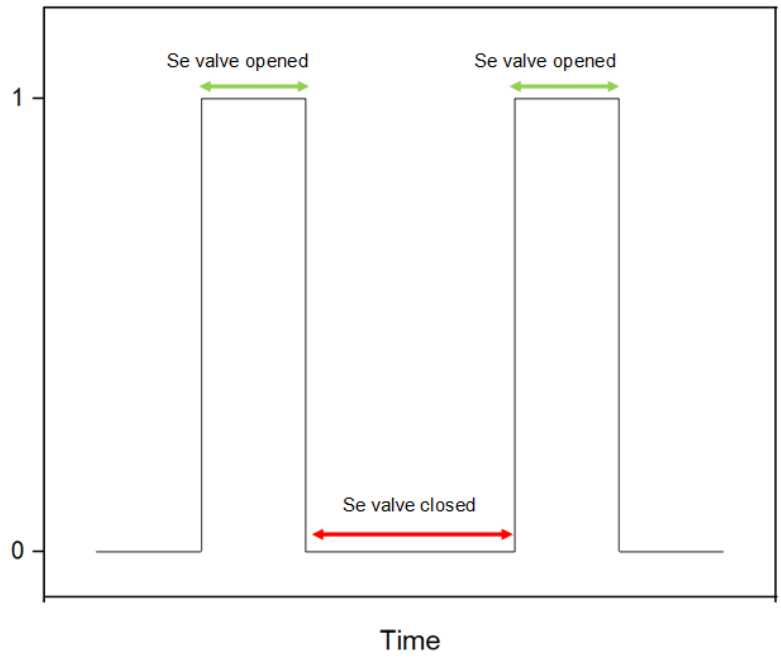

Figure 17. Graphic representation of the Selenium valve opening mechanism.

3.3 Contacts and buffer layer deposition parameters

The first step in the production of the solar cells consists of proper cleaning of the soda-lime glass (SLG) substrate. This step is crucial to achieving good solar cell performance. The presence of impurities on the SLG glass can lead to defects in the different layers of the solar cell. The following picture shows the effect that a badly cleaned SLG glass has on the morphology of the Molybdenum back contact. The cleaning process of the SLG is conducted in an ultrasonic bath and consists of several cleaning steps with a mixture of deionized water and soap.

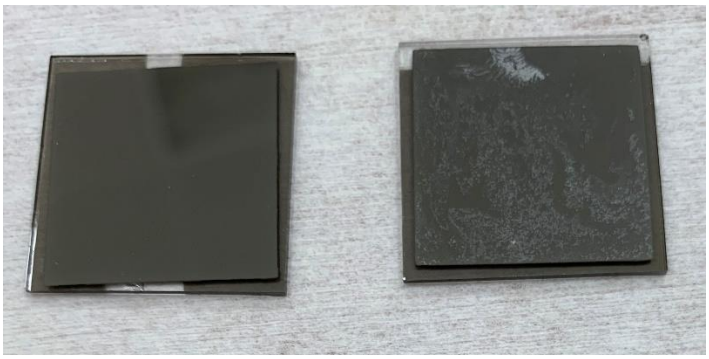

Figure 18. Picture of Molybdenum layer deposited on clean glass (left picture) vs Molybdenum layer deposited on dirty glass (right picture).

To ensure a clean target surface, before each deposition inside STAR, a pre-sputtering of each target is conducted.

As discussed in the previous section, the Mo back contact is deposited by a 2-step sputtering process at different working pressures to obtain the desired bi-layer Molybdenum film. The bottom layer will have a thickness of 100 nm and the top layer will be 400nm thick, equating to a total 500nm thick back contact. The deposition conditions can be seen in Table 1. It is important to notice that the deposition time of the different layers and the voltage can be slightly adjusted, as regular calibrations are conducted since the deposition rate is dependent on the target's usage.

Table 1. Deposition conditions of the Molybdenum bilayer.

Layer Thickness (nm)	**Argon flow (sccm)**	**Working pressure (mbar)**	**Current (A)**	**Voltage (V)**
(1) 100	90	1.2×10^{-2}	0.2	247
(2) 400	45	6.5×10^{-3}	0.2	270

The CdS buffer layer is fabricated by chemical bath deposition. For the majority of the cells fabricated in this work, a KCN-etching treatment (with a 5% wt solution of KCN) of the absorber layer with a fixed duration of 30s is conducted before the CBD process. The role of this step will be explained in the following chapters. The CBD process is done at a temperature of 60°C and a solution of 1.33g of thiourea ($SC(NH_2)_2$), 0.118g of Cd acetate,15ml of NH_3, and 115ml of H_2O is used. To obtain the desired 50nm CdS thick layer, this process has a duration of 14min.

Solar cells were finally completed with the deposition of the window layer. 50nm intrinsic-ZnO layer and 200nm aluminum-doped ZnO layers were deposited by RF-sputtering at room temperature. Table 2 shows the deposition conditions for both layers.

Table 2. Deposition conditions of the window layer.

Layer	Thickness (nm)	Argon flow (sccm)	Working pressure (mbar)	Power (W)
i-ZnO	50	20	5.6×10^{-3}	40
ZnO:Al	200	20	5.6×10^{-3}	60

3.4 Characterization techniques

3.4.1 Scanning Electron Microscopy

Scanning electron microscopy (SEM) is a characterization method used to obtain high-resolution images of solid specimens. SEM generates a variety of signals due to the interaction of high-energy focused electrons with the sample.

The interactions can be divided into two main categories: elastic and inelastic. Elastic events occur when an electron interacts with the nucleus of the specimen and its direction is altered, without a significant change in energy (they retain about 60% to 80% of their initial energy [77]). Backscattered electrons (BSE) provide data on the composition of the sample. The backscattered signal is dependent on the atomic number of the sample's atoms, which translates to different contrasts in the formed image. Heavier elements appear brighter than lower-atomic number atoms [78]. Furthermore, due to their high energy, BSE supply information of deep sample regions. Inelastic events occur when the electrons of the beam transfer substantial energy to the samples' atoms, causing their ionization. As a consequence, loose electrons with low energy, also called secondary electrons (SE), are emitted. Owing to the SE low energy, those generated at deeper sample regions are absorbed, so only SE from a region within few nanometers of the sample surface can escape [79], so they precisely mark the position of the electron beam. Moreover, SE provide topographic information (roughness and surface texture) with good resolution. Increasing the tilting angle of the sample results in higher secondary electrons detection. Characteristic x-rays are generated when an outer shell electron drops to a lower energy level to fill a vacancy created by the secondary electron. The analysis of the x-rays provides information on the chemical composition of the sample. Such an analysis is called energy-dispersive x-ray spectroscopy (EDX).

Figure 19 shows the different interaction mechanisms of the electron beam with the samples, as well as their respective interaction volume.

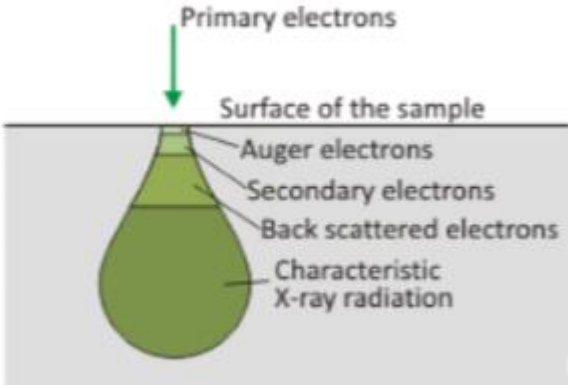

Figure 19. Illustration of the different signals generated by the electron beam specimen interaction in SEM [80][77].

Figure 20a shows the usual structure of a scanning electron microscope. SEMs are composed of an electron gun, responsible for providing the necessary energy to the electrons of the beam, a complex system of lenses and coils to focus, redirect and control the beam, detectors to capture the different signals emitted as a consequence of the beam-sample interaction, all enclosed in a vacuum chamber. The equipment used at INL facilities is a FEI Quanta 650 FEG SEM (see Fig. 20). Its acceleration voltage varies from 1-50keV, has a large range of vacuum pressure conditions (ultra-high, high, and low vacuum), a multi-sample holder is available and a stage that allows for x-y-z, rotational and tilting movement.

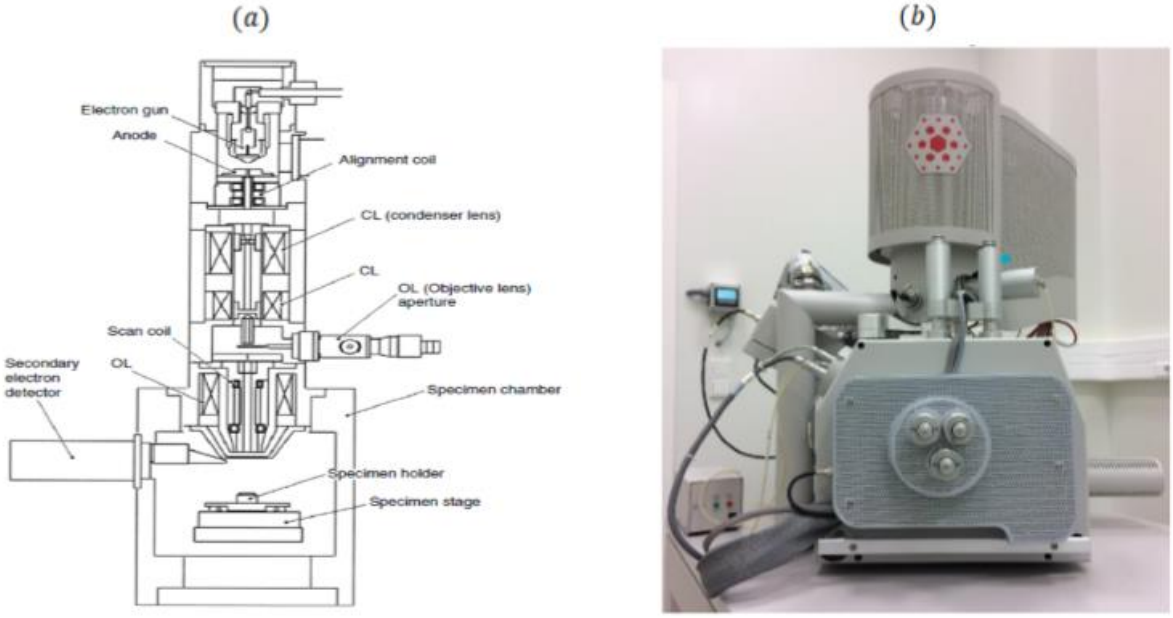

Figure 20. (a) Schematic diagram of scanning electron microscope [77]. *(b) SEM equipment used at INL facilities: FEI Quanta 650 FEG.*

3.4.2 X-Ray Diffraction

The structural properties of crystalline materials are heavily linked to their optoelectronic characteristics. X-ray diffraction (XRD) is an analytical technique that takes advantage of the previously mentioned dependence to determine the atomic structure of a crystal via the interaction of the radiation with the material itself. XRD analysis is based on Bragg's law, which states that when irradiating X-rays on a crystalline sample at an angle of incidence θ it is possible to observe constructive interference if Bragg's condition is fulfilled. Consider two X-ray waves: 1 and 2, that are initially in phase and get reflected by consecutive atomic planes (Figure 21). Wave 2 will travel a longer distance of $2dsin(\theta)$ in comparison with the length covered by wave 1. If this path difference is equal to $n\lambda$, the interference between both rays is constructive and can be detected, otherwise, such interference will be destructive, and the waves will cancel each other. Bragg's law is thus given by the following equation:

$$n\lambda = 2dsin(\theta), \tag{10}$$

where λ is the wavelength of the incident ray, n is the order of refraction (usually $n = 1$), d is the interplanar distance, and θ is the angle of incidence.

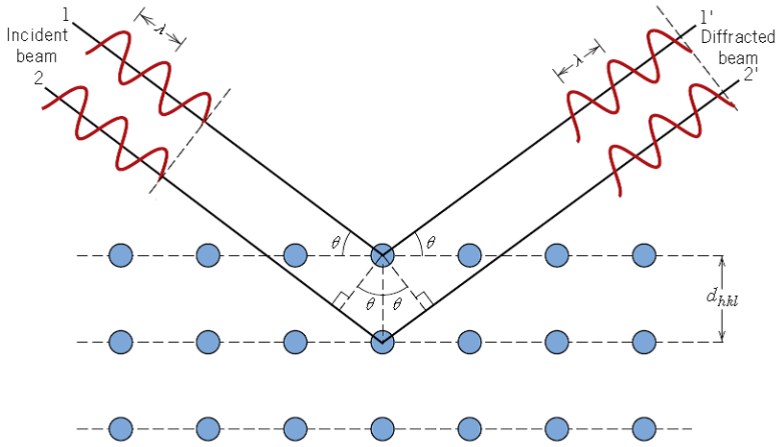

Figure 21. Schematic describing Bragg's law. The X-ray hits the sample at an angle of incidence θ. d_{hkl} is the distance between diffracting planes. [81]

During an XRD analysis, the X-Ray source rotates around the sample, varying the incident angle. The diffracted waves are captured by a detector, which converts the signal to a count rate for each scanned angle. Each material has a specific set of unique diffraction peaks [82]. These peaks are identified by comparison of the d-spacing measurements obtained during the XRD analysis with standard reference

patterns (which can be found in several different databases). A typical XRD-measured peak of a crystalline sample can be seen in Figure 22.

From the analysis of the highest intensity peak, it is possible to determine the size of the crystallites (D), given by the Scherrer equation:

$$D = \frac{K\lambda}{Bcos(\theta_B)}, \tag{11}$$

where λ is the X-ray wavelength, K is a dimensionless shape factor dependent on the average crystallite shape (in this work, the value used for K is 0.9), B is the width of the highest intensity peak at half of the intensity, and θ_B is the Bragg angle.

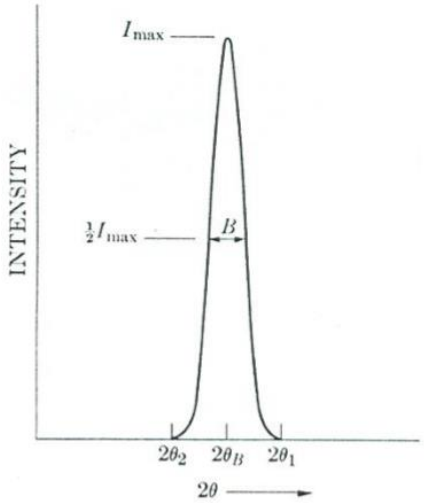

Figure 22. Schematic of an XRD measured peak for a crystalline sample [81].

To describe the preferential orientation of the sample crystals, the texture coefficient T_C(hkl) can be calculated, using the following equation:

$$T_C(hkl) = \frac{{}^{I_{(hkl)}}/_{I_{r(hkl)}}}{{}^{1}/_{N}[\Sigma^{{}^{I(hkl)}/_{I_r(hkl)}}]}, \tag{12}$$

where I(hkl) indicates the X-ray diffraction intensities of a certain peak, n is the number of diffraction peaks considered, and I_r(hkl) is the intensity of the reference diffraction pattern shown on the ICDD PDF card of the studied material. If the texture coefficient of a certain peak is greater than unity, it implies a preferred orientation.

The equipment used in this work is an XRD model: Panalytical X'PERT PRO MRD (Fig. 23). A Cu X-ray tube is used to produce the monochromatic radiation, which is later collimated and directed towards the sample.

Figure 23. XRD equipment at INL facilities.

3.4.3 Raman Spectroscopy

When light with a known frequency scatters on a surface two different scattering phenomena can occur: elastic and inelastic scattering. Elastic (Rayleigh) scattering takes place when the scattered light has the same energy as the incident light (i.e. there is no loss of energy) and the photon frequency remains constant. Inelastic scattering of light occurs when the incident photon interacts with the sample and its frequency is shifted to lower (Stokes radiation) or higher (anti-stokes radiation) photon frequencies. This phenomenon was observed by C.V. Raman in 1928 [83] and is referred to as Raman scattering. The frequency shift, known as Raman shift, is calculated by the following formula:

$$Raman\ shift\ [cm^{-1}] = \frac{10^7}{\lambda_{ex}[nm]} - \frac{10^7}{\lambda_{Raman}[nm]} \quad (13)$$

where λ_{ex} is the wavelength of the incident radiation (usually this radiation is either monochromatic or shows a very narrow frequency band), and λ_{Raman} is the scattered wavelength.

The occurrence of Raman scattering is better understood as a change of the rotational and/or vibrational states of the material while being illuminated. These changes are Raman active if there is a change in the polarizability of the molecules. When the incident photon hits the sample, it can either transfer or receive energy from these quantum states changes. This interaction causes a wavelength shift of the

scattered light, forming the Raman spectra, which provides information about the chemical structure, phase, crystallinity, intrinsic stress and strain, and molecular interactions of the examined sample.
The equipment used for Raman measurements is the Witec alpha300 R confocal Raman microscope. An excitation laser wavelength of 532nm with power ranging from [0.8-1.0] mW will be used during the Raman measurements.

Figure 24. Raman microscopy at INL facilities.

3.4.4 Solar simulator

When the solar cell fabrication is completed, it is necessary to measure its I-V characteristics to understand the influence of the different deposition parameters. The 2.5×2.5 cm^2 cell is divided into smaller cells, providing larger statistics. The ZnO:Al is not conductive enough to allow proper current transport over large distances, so diving the cells into smaller cells avoids such a problem. Besides this, since the deposition of the different layers is not completely uniform, the cell separation also provides a better understanding of the influence of the distance of the sample to the different targets and the selenium source. The cell separation can be done either manually, by scratching the sample with a needle, or via photolithography. A detailed comparison of the two methods is provided in section 4.1. Once the cells are separated, one corner of the sample is scratched until the Molybdenum layer is reached. The exposed Mo layer is covered with Indium, to ensure a proper electrical connection with the separated cells and simultaneously avoid the oxidation of the exposed molybdenum.
To properly compare the performance of the different solar cells it is necessary to have consistent measurement conditions. The measurements are done in an Oriel Sol3A Class AAA Solar Simulator. The

applied voltage varied from -0.1 to 0.6V, although this value could be slightly adjusted, according to the performance of the cell.

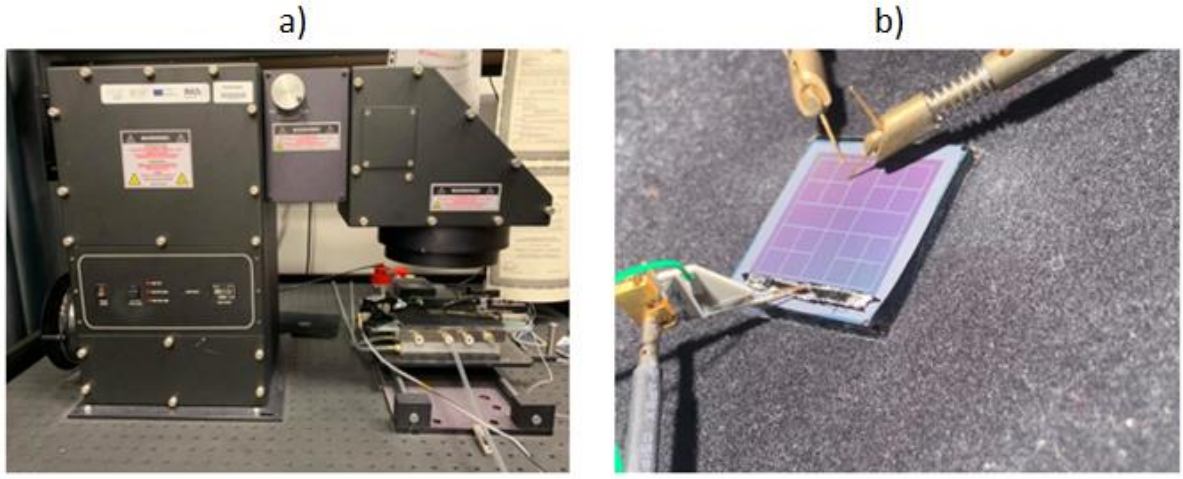

Figure 25. (a) Solar simulator equipment at INL facilities. (b) Close-up image of solar cell I-V measurement setup with the contact needles.

4. CALIBRATIONS

4.1 CIG target Calibration at different powers and Selenium rates

It is extremely important to understand the behavior of the CIG target at different sputtering conditions, to better control the deposition of the absorber layer. The target behavior was tested under different Argon flows without any supply of Selenium. It has been proven that sputtering with lower working pressures improves the quality of the deposited CIGSe films, as larger grains can be obtained [84]. The correspondent working pressures and powers for different Argon supplies can be seen in Table 3 and Figure 26, respectively. It is clear that, for the same applied current, lower pressures allow higher sputtering powers. However, this comes at a cost. With lower Argon flow, the plasma becomes more unstable, shutting off quite frequently. This was the case for sputtering with a 20 sccm Argon flow. Therefore, an Argon flow of 25 sccm, corresponding to a working pressure of 5.5×10^{-3} mbar, was chosen as default for all CIGSe depositions presented in this thesis.

Table 3. CIGSe chamber pressure at different Argon flows.

Argon flow (sccm)	Working pressure (mbar)
20	4.9×10^{-3}
25	5.5×10^{-3}
30	5.9×10^{-3}
35	6.3×10^{-3}

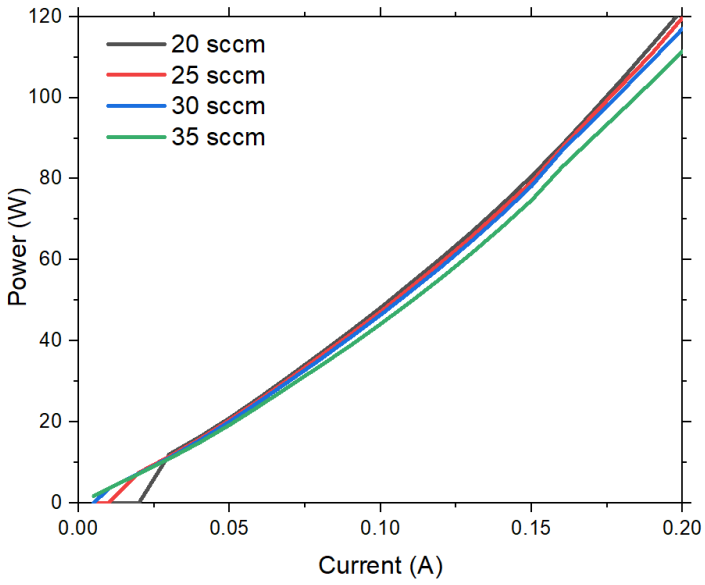

Figure 26. Influence of Argon flow on sputtering power of CIG target

In STAR one can manipulate the deposition of the CIGSe layer in two different ways, assuming a fixed working pressure of 5.5×10^{-3} mbar. First, it is possible to control the sputtering power of the CIG target and secondly, to choose how much selenium is supplied. Selenium evaporates at 220 °C. If the absorber layer deposition is done at temperatures lower than 220 °C and excess selenium is supplied to the sample, amorphous selenium can be incorporated in the CIGSe layer, which is not desirable. This problem does not occur at higher temperatures (T > 220 °C), as any excess selenium will evaporate. In previous STAR studies, it has been shown that varying the valve opening and the Selenium pulses duration can influence parameters such as the rugosity of the absorber layer, even though the stoichiometries remain constant, assuming sufficient selenium is being supplied [103].

Before making any CIGSe depositions, a corner piece of the target was removed to confirm its stoichiometry. EDX results can be seen in Table 4. A 60% atomic percentage of Copper, 24 atomic % of Indium, and 16% of Gallium were measured, meaning that films deposited with this target will be very Copper-rich ($\frac{[Cu]}{[Ga]+[In]}$ (CGI)=1.5), and exhibit low indium concentrations ($\frac{[Ga]}{[Ga]+[In]}$ (GGI)=0.4). High-efficiency CIGSe absorber layers should have the following stoichiometric ratios: 0.8 < CGI < 1 (Cu-poor films) and 0.2 < GGI < 0.3. Increasing the CGI ratio leads to higher conductivity and a decrease in resistivity of the CIGSe layer [55]. The conductivity of Cu-rich films is about three orders of magnitude higher than that of Cu-poor films. With the stoichiometry of the used target, it is expected that unwanted $Cu_{2-x}Se$ phases will form [85], likely creating shunt paths and therefore, deteriorating the performance of the solar cell. One focus of this thesis will be on how to deal with and eliminate this undesired phase.

Table 4. CIG target stoichiometry. Results were obtained in EDX using an accelerating voltage of 30k eV.

Cu at %	In at %	Ga at %
60	24	16

As discussed in previous chapters, an ideal CIGSe absorber layer should have a thickness of 1-2 μm. To ensure that consistent, reliable, and easily comparable results are obtained all deposited CIGSe layers will have a thickness of 2 μm. Consequently, a thickness calibration at different powers, and with simultaneous selenium supply, was conducted. A substrate temperature of 350°C, a valve opening of 9 mm, and 0.1s ON/0.9 s OFF selenium pulses were selected for this calibration. Figure 27a shows the deposition rate dependence on sputtering power. As expected, an increase in current, and subsequent power increase, leads to a higher deposition rate. Such behavior is linear until a sputtering power of 60 W is reached. For higher values of power, the deposition rate increase is not as evident, possibly because not enough selenium is being supplied, as a consequence of increased collisions of Selenium atoms/molecules with the higher density of Cu-In-Ga atoms. To confirm this, EDX with an accelerating voltage of 20 keV was performed on all calibration samples, and the Selenium to Copper, Indium, and Gallium rate was analyzed. Standard CIGSe films should have a Selenium atomic percentage of 50%, resulting in a $\frac{[\mathrm{Se}]}{[\mathrm{Cu}]+[\mathrm{Ga}]+[\mathrm{In}]}$ ratio equal to 1. The ratio to power dependence can be seen in Figure 27b. The 87 W film shows a ratio of 0.78, meaning that there is a Selenium deficiency in the sample, confirming the above hypothesis.

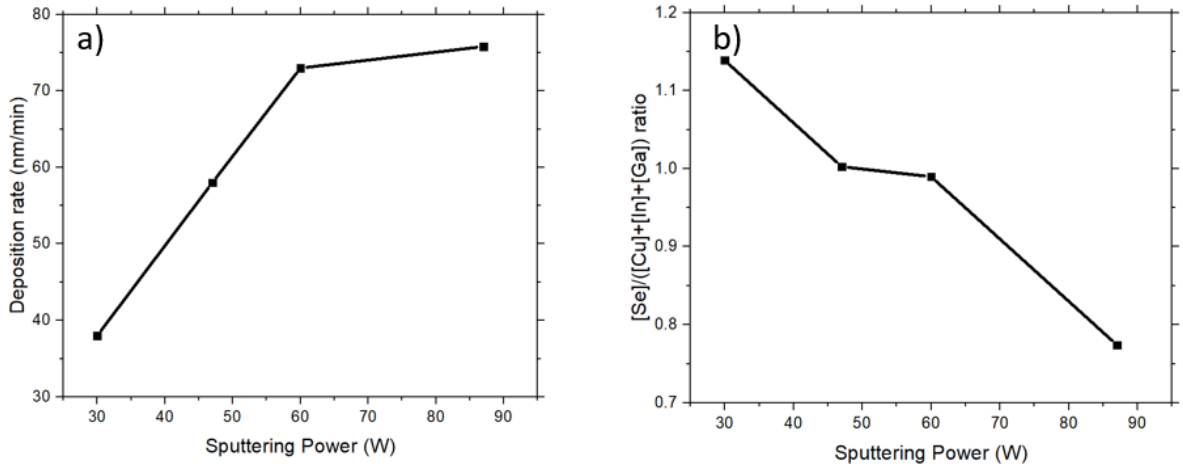

Figure 27. (a) Deposition rate dependence on sputtering power for the CIGSe layers and (b) Se/(Cu+In+Ga) ratio dependence on sputtering power.

4.2 Optimization of the valve opening

The next step was to determine the optimal Selenium valve opening. Several CIGSe layers were grown with different valve openings (8.6, 8.8, and 9 mm) at 200 °C (low temperature was used to minimize the selenium re-evaporation and to have a better understanding of how much Se is being supplied to the sample). All other deposition parameters were kept constant, as determined in the previous sub-chapter. Scanning electron microscopy images for different valve openings are shown in Fig. 28. For a valve opening of 8.6 mm, the absorber layer surface is homogeneously covered with whisker-like structures. These structures were also present in the 8.8 mm sample, even though their density is much smaller. Finally, the 9 mm sample did not exhibit this type of structure. The whisker-like growth phenomenon was previously reported in the literature [86], where it was attributed to growth under low Se-flux and high-Cu concentrations. The insufficient supply of selenium was confirmed by EDX analysis, where the 8.6 mm sample showed a [Se]/([Cu]+[Ga]+[In]) ratio of 0.65 (Fig. 29).

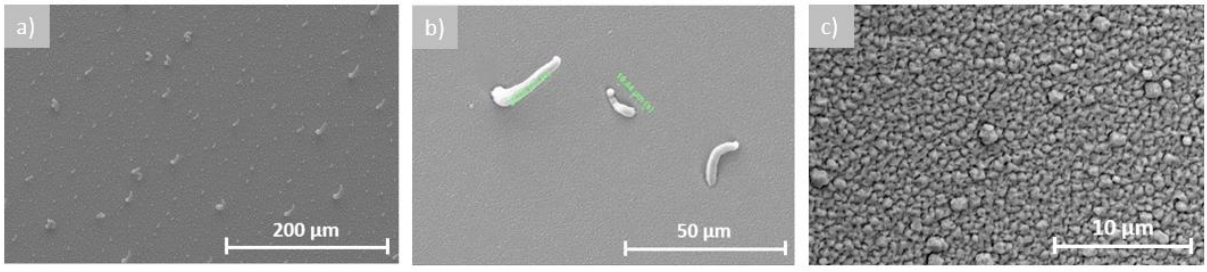

Figure 28. SEM images of 2µm CIGSe films grown at 200 °C, P_{CIG}=30W, p=5.5× 10^{-3} mbar, 0.1 ON/0.9 OFF Se pulses, with a valve opening of (a) 8.6 mm (b) 8.8 mm and (c) 9 mm.

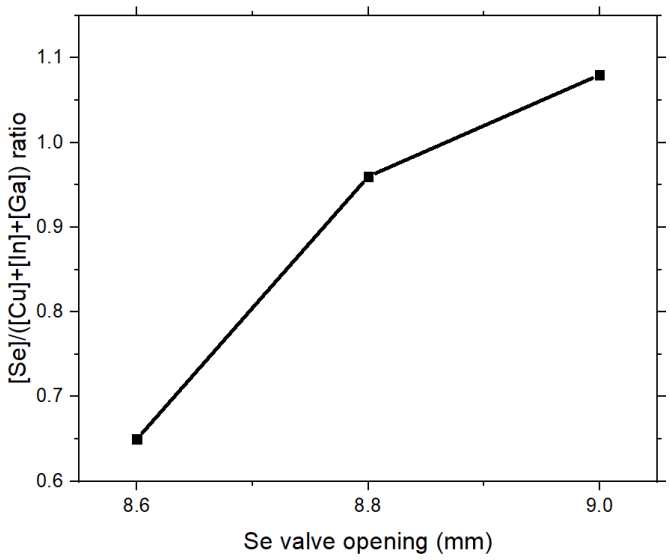

Figure 29. Se/(Cu+In+Ga) ratio of CIGSe absorber layers grown with different valve openings.

The whiskers-like structures might create shunting of the solar cells, deteriorating their performance and are, therefore, undesired. Thus, for all depositions presented in the next chapters, the following deposition parameters were selected: a sputtering power of 30 W, a valve opening of 9 mm, 0.1 s ON/0.9 s OFF selenium pulses, and 5.5×10^{-3} mbar working pressure. The total time for a 2 μm thick CIGSe depositions will be 52 min and 30 s.

4.3 Manual cell separation vs. lithography separation

The separation of the finished solar cells into smaller cells is fundamental. Here, two different methods of solar cell separation will be studied: manual and lithography-assisted separation (Fig. 30). Manual separation is done with a needle to scratch the window, CdS, and CIGSe layers, leaving molybdenum exposed. The main disadvantages of such a method are that the separated cells have different areas, and, due to inconsistency in the scratching process (i.e. the applied force), the removal of the window, CdS, and CIGSe layers may not be performed correctly, which may lead to incomplete separation of the cells (see Fig. 31). However, such a problem does not occur for lithography-assisted separation. This process is conducted in the cleanroom, where an AutoCAD designed hard mask is used to define the lines that separate the cells. Following the photoresist coating, baking, UV exposure, and development, the samples are submitted to an HCl etching process, which removes the exposed window and CdS layers, finalizing the separation of the cells. The CIGSe film is not removed, however, this is not a problem,

as the electron diffusion length of the absorber layer is within the [0.5-1.3] μm range [87]. The main advantages of lithography-assisted separation are that the cells have consistent sizes and are always well divided.

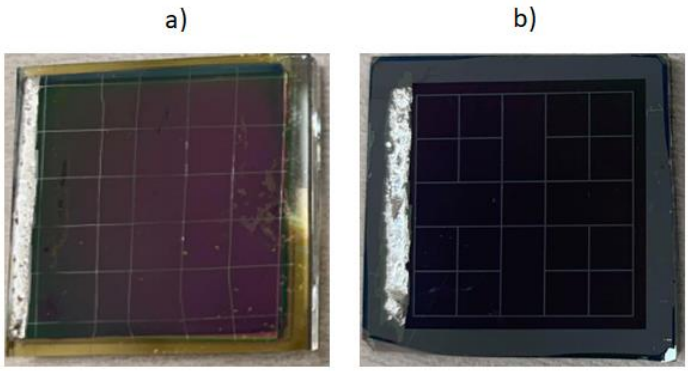

Figure 30. Picture of a (a) manually scratched cell and (b) lithography separated cell

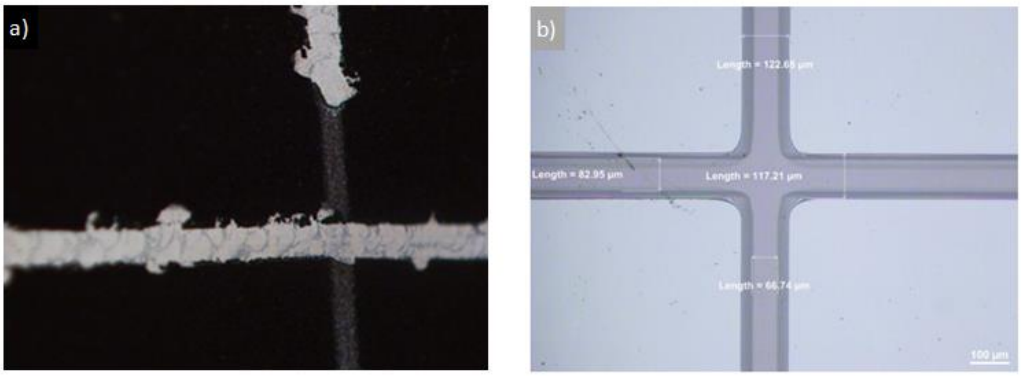

Figure 31. Optical microscope images of the line that separates the cells for (a) manually and (b) lithography separated cells.

To test and compare both methods, an i-ZnO/ZnO:Al double layer was sputter-deposited as the front contact on high-quality and homogeneous Mo/CIGS/CdS substrate supplied by *Nice Solar Energy*. High-quality substrates were used to guarantee that, if significant differences are detected in the performance of the solar cells, they can be attributed to the separation method, and not the solar cell itself. The box plots of the I-V parameters and average results comparing the different methods can be seen in Figure 32 and Table 5, respectively. Lithography separated cells showed an average efficiency loss of almost 1% in comparison with manually separated cells. The efficiency decrease can be attributed to a significant drop in short-circuit current density. Manually separated cells have on average, a short-circuit current density of 33.9 mA/cm^2, while lithography separated cells exhibited an average J_{sc} of 26.2 mA/cm^2, meaning that there was a 23% decrease for lithography-separated cells. This drop also explains the

increase in fill factor observed for the lithography method, since the fill factor is inversely proportional to the short-circuit current density, as evidenced by Equation (7). The open-circuit voltage, series, and shunt resistances were not significantly influenced by the separation method.

It is believed that the lithography process damages the window layer of the solar cell, reducing the current capture. For this reason, all solar cells fabricated in this thesis will be manually separated.

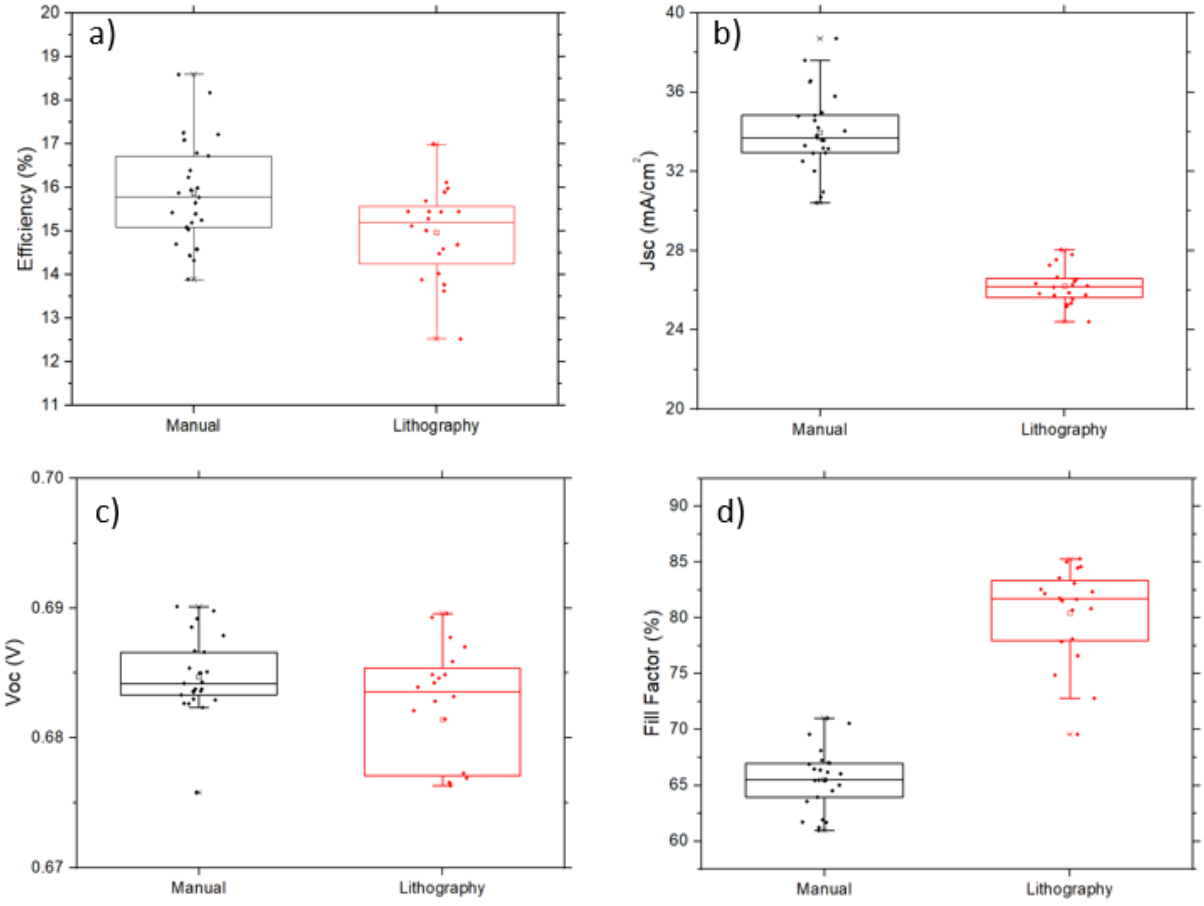

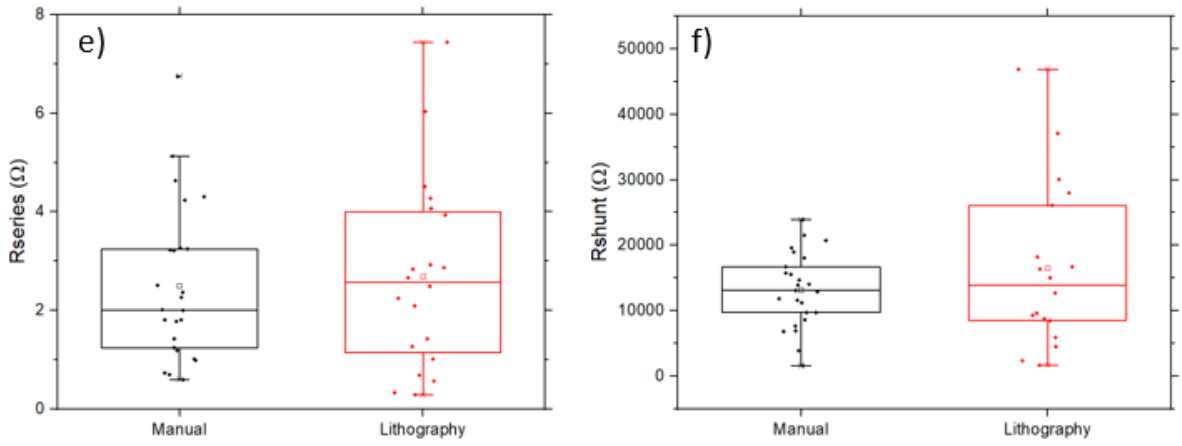

Figure 32. Box plot of (a) efficiency, (b) short-circuit current density, (c) open-circuit voltage, (d) fill factor, (e) series and (f) shunt resistances of manually and lithography separated cells.

Table 5. Average values of I-V parameters of solar cells separated via the manually and lithography methods.

Separation method	**Efficiency (%)**	**J_{sc} (mA/cm²)**	**V_{oc} (V)**	**Fill Factor (%)**	**Rseries (Ω)**	**Rshunt (Ω)**
Manual	15.9 ± 1.2	33.9 ±2. 0	0.69 ± 0.01	65.6 ± 2.7	2.5 ± 1.6	13161 ± 5593
Lithography	15.0 ± 1.0	26.2 ± 0.9	0.68 ± 0.01	80.5 ± 4.3	2.7 ± 1.9	16537 ± 12529

5. EFFECT OF KCN-ETCHING IN CIGSE SOLAR CELLS

The stoichiometry of the Cu-In-Ga target used in this work leads to Copper-rich growth conditions, enhancing the growth of CIGSe grains and, consequently, improving the efficiency of the solar cell, assuming that the excess Copper is removed [85]. There are different methods to remove excess Copper: either by using a multi-stage deposition, where one of the deposition stages is Copper-rich (enhancing the crystal growth) and the other stages are copper-deficient thus balancing out the Copper atomic ratios or by using a single Copper-rich stage where, after the deposition, a KCN treatment is conducted and the excess Copper-Selenide is chemically etched.

In this chapter, $Cu(In,Ga)Se_2$ absorber layers grown with a single Copper-rich stage for different deposition temperatures will be analyzed before and after a 30-second KCN-etching process. Solar cell results are shown at the end of the chapter.

5.1 Low-temperature growth

5.1.1 Characterization of the absorber layer

$Cu(In,Ga)Se_2$ thin films were first deposited at 200 °C on top of a Molybdenum bilayer and a soda-lime glass substrate. The other deposition parameters remained as defined in the calibration chapter: P_{CIG} = 30 W; p = 5.5×10^{-3} mbar; Se valve opening of 9 mm; 0.1 s ON/0.9 s OFF Selenium pulses. The goal of this first experiment was to confirm that the Cu-rich growth conditions are favorable for grain growth.

To identify the influence of the KCN-etching process in the morphologies of the CIGSe films, SEM analysis was carried out before and after such treatment. Figure 33 shows an overview of the film's surface. Before KCN-etch, the film is uniform, however, after the chemical etching treatment, large "craters" were observed, which may be attributed to the removal of $Cu_{2-x}Se$ material. It is expected that the absorber layer thickness inside the craters is significantly thinner than the expected 2 μm. A close-up image of the crystals of the 200 °C sample is also shown in Fig. 34. CIGSe grains reach sizes of 1.1 μm, confirming the grain growth enhancement under Cu-rich conditions, in comparison with the maximum grain size of 450 nm achieved when films were grown under Cu-poor conditions (see annex). The grain size was not influenced by the KCN etching process, however, it is clear that the chemical etching leads to more porous films and a size increase in what can possibly be pinholes, which may lead to short-circuits

between the conductive window layers and the back contact or damage the CdS/CIGSe interface, once the solar cell device is completed.

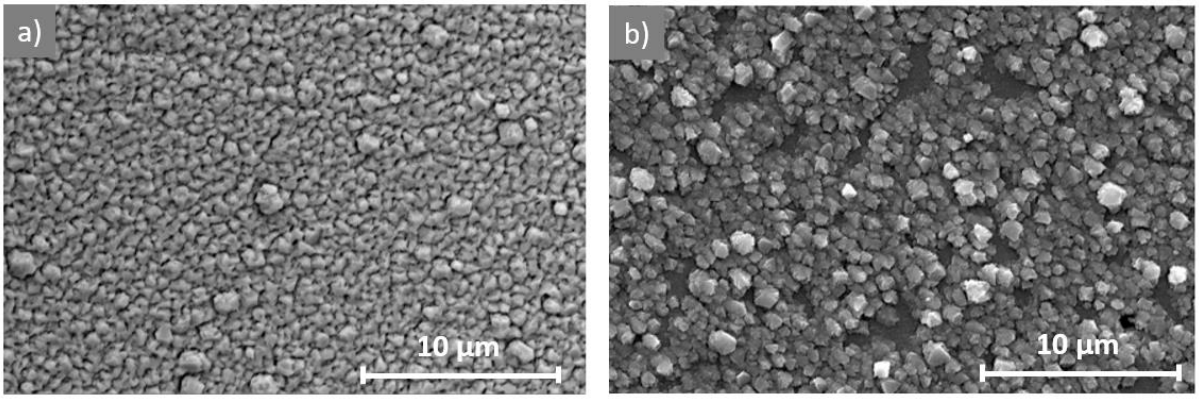

Figure 33. Overview image of 200 °C CIGSe sample (a) before and (b) after KCN-etching.

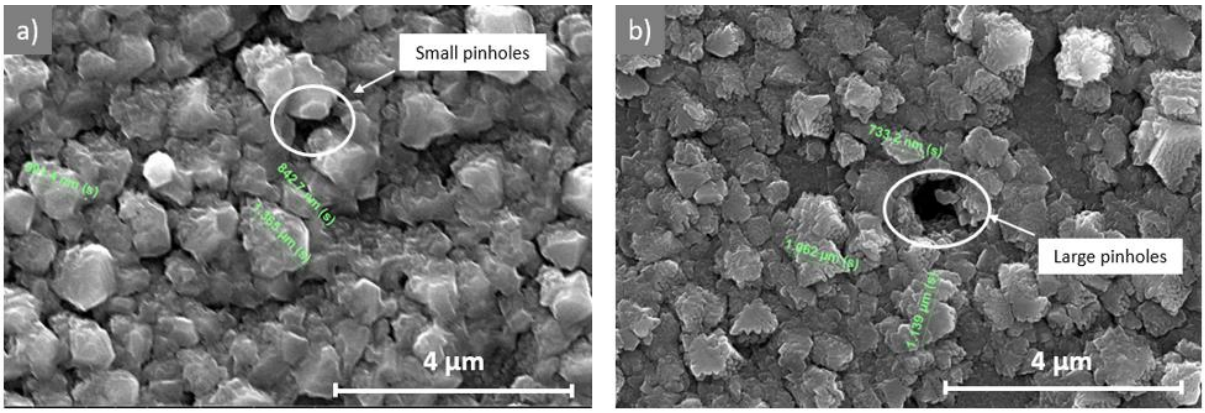

Figure 34. SEM images of CIGSe crystals (a) before and (b) after the KCN etching treatment at higher magnification.

EDX results for the 200 °C CIGSe layer are presented in Table 6. In agreement with the Cu-In-Ga target stoichiometry, before being submitted to the KCN etching process, the absorber layer exhibits Cu-rich stoichiometries, with a Copper atomic percentage of 28.6% and a CGI ratio of 1.52, indicating the existence of a $Cu_{2-x}Se$ phase on the CIGSe film. The GGI and [Se]/([Cu]+[In]+[Ga]) (SCGI) ratios are within the expect value range.

Following the etching treatment, the Cu atomic percentage and the CGI ratio decreased to 22.9% and 0.96, respectively. The film became Cu-poor, indicating that the undesired Copper-Selenide phase was successfully removed. As a consequence, the atomic percentage of Gallium and Indium increased slightly, even though the GGI ratio remained constant. Finally, a small increase in selenium concentration was detected. The most commonly observed $Cu_{2-x}Se$ phase in Cu-rich growth environments is the Cu_2Se

phase [85], thus when Copper-Selenide is eliminated, two atoms of Cu and a single atom of Se are removed, and the relative concentration of Se increases.

Table 6. Chemical composition of the CIGSe absorber layer deposited at 200 °C, obtained by EDX analysis with a 30 keV accelerating voltage.

	Cu (at%)	**Ga (at%)**	**In (at%)**	**Se (at%)**	**CGI Ratio**	**GGI Ratio**	**SCGI Ratio**
Before KCN	28.6	8.0	11.4	52.0	1.53	0.42	1.08
After KCN	22.9	10.0	13.8	53.3	0.96	0.42	1.13

Structural analysis of the deposited film before and after KCN was carried out by XRD diffraction and both patterns, as well as the $Cu_{2-x}Se$ ICDD PDF card (00-006-0680) and CIGSe ICDD PDF card (01-083-3354), are shown in Figure 35. It is clear that the film is polycrystalline, with preferential orientation along the (112) plane. Other CIGSe orientations corresponding to (220), (312/116), (400), (332) planes, and the molybdenum (110) plane were also observed. The typical XRD $Cu_{2-x}Se$ peaks are very similar to those of the typical CIGSe, thus, identifying the $Cu_{2-x}Se$ phase with XRD analysis is not a straightforward task [88]. The XRD pattern of the film before the KCN treatment exhibits an identical pattern to that obtained after KCN, apart from a small decrease in peak intensity following the etching, and a low-intensity peak at 31.1°, which can be attributed to the presence of the $Cu_{2-x}Se$ phase (after KCN this peak was no longer detected). After KCN, no complex peaks were detected, meaning that the deposited film forms single-phase chalcopyrite structures [84].

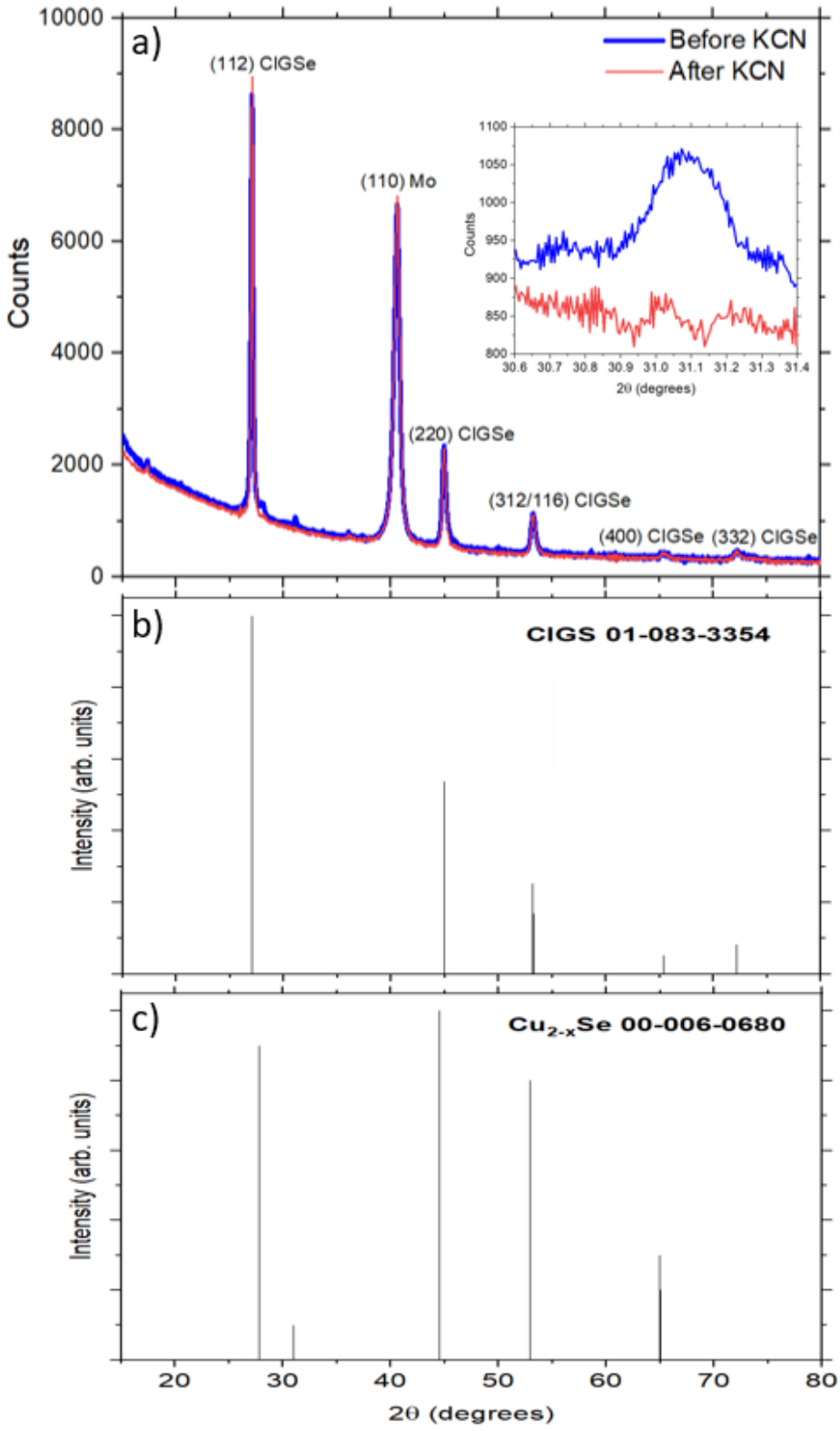

Figure 35. (a) XRD pattern of 200 °C CIGSe sample before and after KCN and a zoomed image of the peak attributed to the Copper-Selenide phase, (b) diffraction patterns of the $Cu_{2-x}Se$ phase according to the ICDD PDF card (00-006-0680), and (c) diffraction patterns of the CIGS according to the ICDD PDF card (01-083-3354),

To unambiguously show the presence of the Copper-Selenide phase and its removal by KCN-etching, Raman spectroscopy was performed [88]. An excitation wavelength of 532 nm and a power of 0.8 mW were used. The Raman spectra analysis is shown in Figure 36. As expected, before being submitted to the KCN etching treatment, the film exhibits a peak at 259 cm^{-1}, which is assigned to the A1 mode of the $Cu_{2-x}Se$ compound [88]. Following the KCN treatment, this mode was no longer detected, meaning the Copper-Selenide phase was successfully removed. Both spectra exhibit a Raman shift located around 174-175 cm^{-1}, which corresponds to the A1 mode of chalcopyrite CIGSe films, and the intensity of this peak increased significantly after the KCN treatment. It was previously reported [89] that by using an excitation wavelength of 532 nm, a penetration depth of the backscattered light in the CIGSe layer is estimated to be <100 nm. Thus, the significant intensity increase of the A1 mode of the absorber layer detected after the etching treatment, indicates that, before this treatment, the surface was heavily covered with the Copper-Selenide phase.

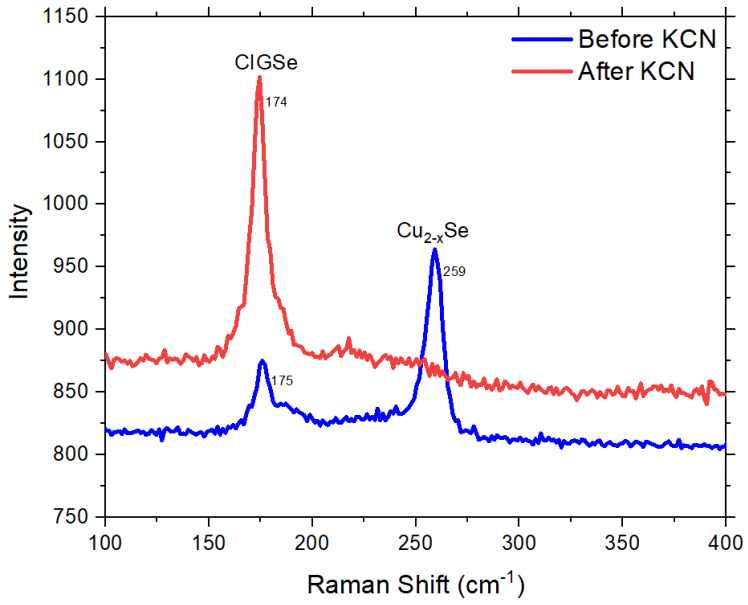

Figure 36. Raman spectrum of 200 °C CIGSe sample before and after KCN.

5.2 Temperature Series

The deposition temperature (T_{SUB}) is an important parameter in the growth of CIGSe thin films. T_{SUB} is known to have a strong influence on the surface morphology (e.g. grain size), elemental composition and, it has been reported that increasing this temperature leads to an enhancement in solar cell performance [2]. In this subchapter, the influence of substrate temperature will be studied; $Cu(In,Ga)Se_2$ absorber layers will be deposited on top of a Molybdenum bilayer and a soda-lime glass substrate at temperatures ranging from 350 °C to 500 °C. The other deposition parameters remain the same: P_{CIG} = 30 W; p = 5.5×10^{-3} mbar; Se valve opening of 9 mm; 0.1 s ON/0.9 s OFF Selenium pulses.

5.2.1 Characterization of the absorber layer

Scanning electron microscopy images of the four CIGSe layers after the KCN treatment grown with temperatures ranging from 350 °C to 500 °C are shown in Fig. 37. It is observed that using higher substrate temperatures results in an increased grain size. CIGSe films grown at 350 °C exhibited grain sizes of 1 μm, while films grown at 500 °C exhibited grain sizes up to 2.6 μm. Despite the difference in grain size, the CIGSe grain shape looks very similar for all temperatures. All samples show very well pronounced grain boundaries (GBs). Furthermore, the presence of a high density of holes in between GBs is evident. This phenomenon is attributed to the Cu-rich conditions and KCN treatment. Even though a profound understanding of the GBs role is still lacking, it is believed that these interfaces tend to become sinks for both chemical impurities and structural defects that segregate from the grain interior during the growth [90]. They also tend to form recombination centers, diminishing the carrier transport [91]. High-efficiency CIGSe solar cells are usually achieved using an alkali-fluoride post-deposition treatment, which is believed to have a positive impact on the GBs [92].

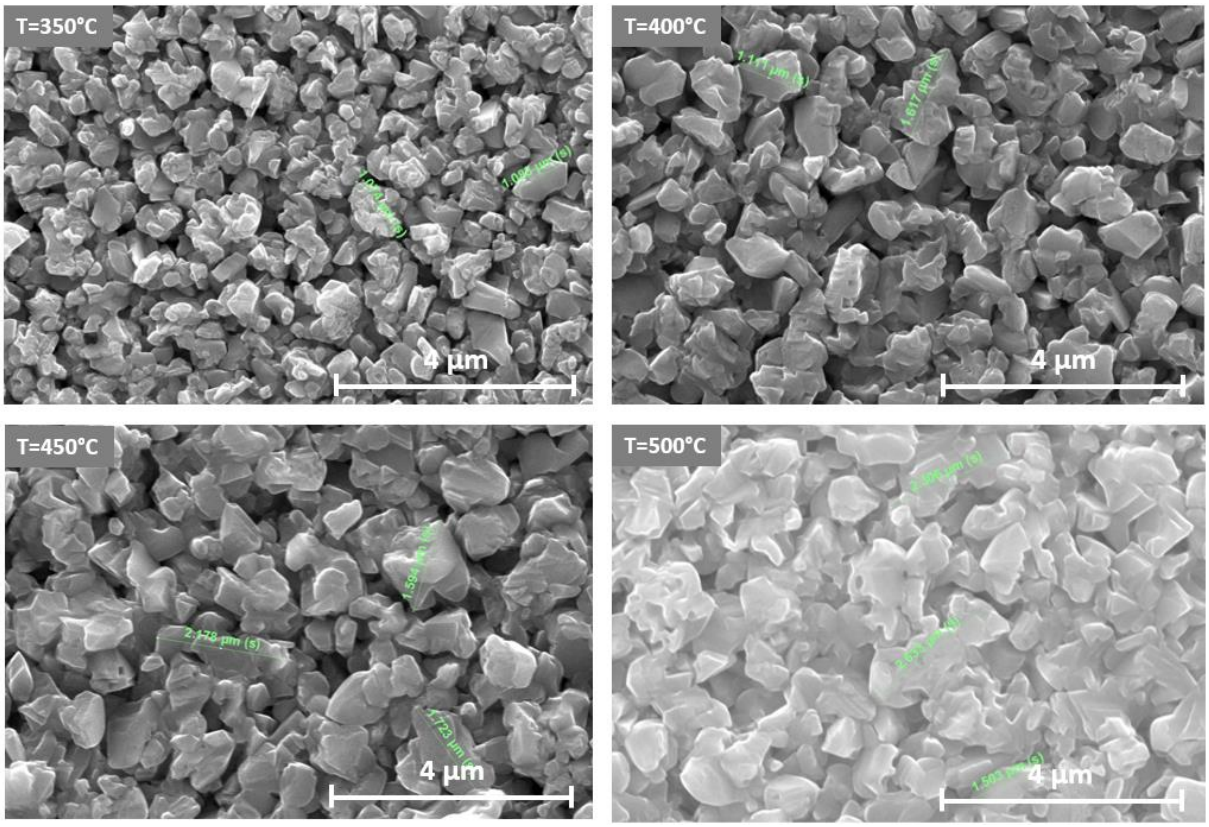

Figure 37. SEM Images of CIGSe crystals after KCN for deposition temperatures of 350 °C, 400 °C, 450 °C, and 500 °C.

Quantification of the bulk elemental concentrations of Cu, In, Ga, and Se obtained by EDX analysis is presented in Table 7 and Fig. 38. As already observed for the 200 °C sample, before the KCN treatment, all films exhibit Cu-rich stoichiometries, ranging from 31.1% (for 350 °C) to 34.7% (for 500 °C). The atomic percentage of Cu obtained for this set of samples is higher than that obtained for the 200 °C sample, indicating that higher temperatures favor even more the Copper-Selenide formation. Following the KCN etching treatment, all layers became Cu-poor and showed very similar Copper contents and CGI ratios. The temperature variance had minimal influence on the Gallium and Indium concentrations. The GGI ratio was near to the Cu-In-Ga target stoichiometry. After KCN, the Indium and Gallium concentrations increased, while the GGI ratio remained constant (the small deviation can be explained by the accuracy of the EDX measurements). The selenium concentration and the SCGI ratio increased after the chemical etching. This increase was more evident for the CIGSe samples which have higher Cu-rich stoichiometries (500 °C and 400 °C).

Table 7. Chemical composition of the CIGSe absorber layer deposited at 350 °C, 400 °C, 450 °C, and 500 °C, obtained by EDX analysis with a 30 keV accelerating voltage.

Temperature (°C)		Cu (at %)	Ga (at %)	In (at %)	Se (at %)	CGI ratio	GGI ratio	SCGI ratio
350	Before KCN	31.1	9.9	12.9	46.1	1.36	0.43	0.86
	After KCN	24.1	11.3	16.7	47.9	0.86	0.40	0.92
400	Before KCN	34.4	8.2	11.9	45.5	1.71	0.41	0.84
	After KCN	24.1	11.6	15.9	48.4	0.88	0.42	0.94
450	Before KCN	31.6	8.8	12.2	47.4	1.51	0.42	0.90
	After KCN	23.9	11.4	16.6	48.1	0.85	0.41	0.93
500	Before KCN	34.7	8.4	12.0	44.9	1.70	0.41	0.81
	After KCN	24.0	10.7	16.9	48.4	0.87	0.39	0.94

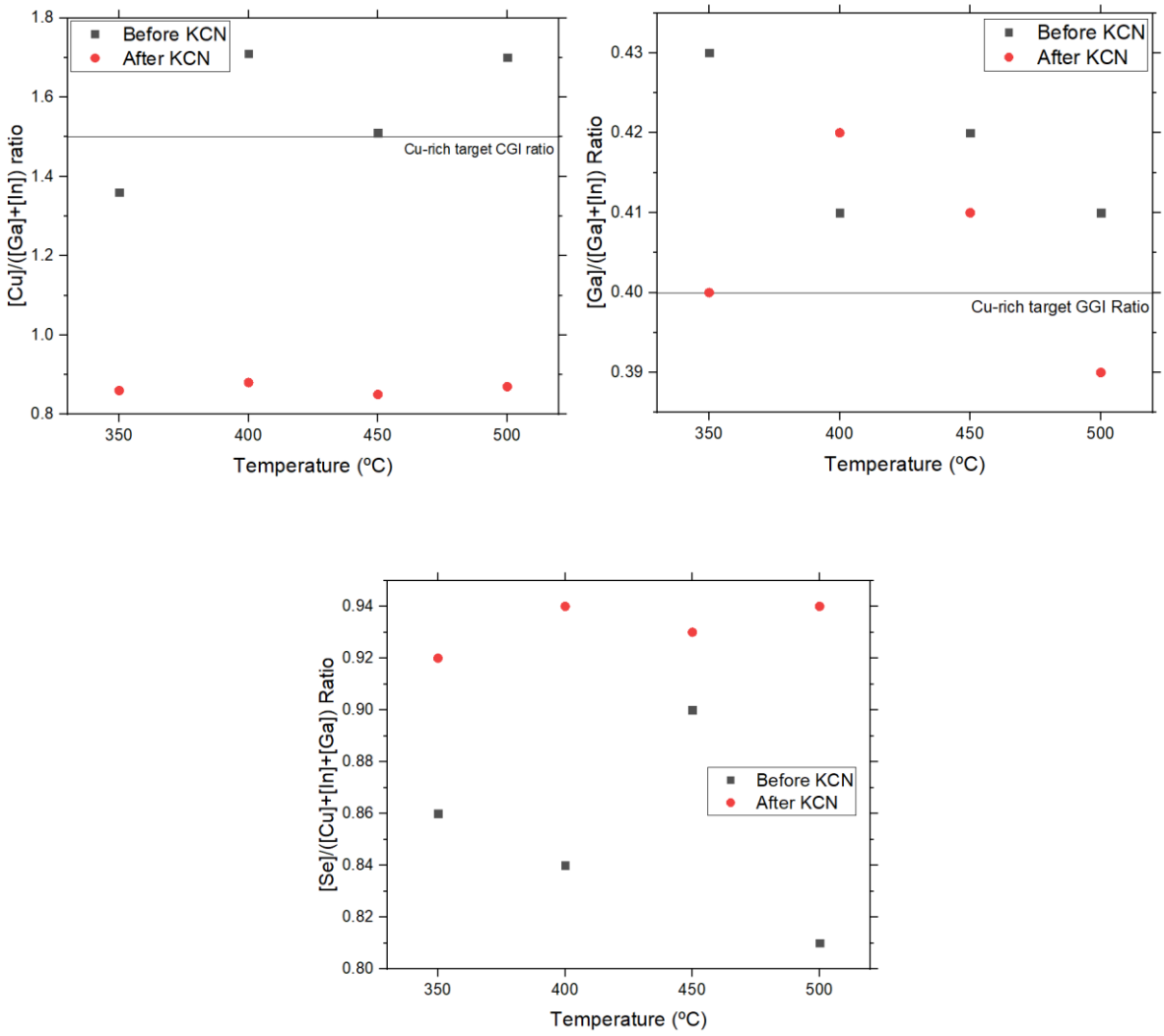

Figure 38. Evolution of the stoichiometric ratios with the substrate temperature.

The XRD diffractograms following the KCN treatment of the CIGSe thin films deposited at various substrate temperatures are given in Fig. 39. The results show polycrystalline films for all temperatures, and that the temperature increase didn't have a significant impact on the XRD patterns, since all temperatures show very similar patterns. As observed for the 200 °C sample, the films appear to show a preferential crystal orientation along the (112) planes. Other CIGSe orientations corresponding to (220), (312/116), (400), (332) planes, and the molybdenum (110) peak were also observed. Fig. 40 shows a zoomed-in image of the (112) and (220) planes. The intensity of such peaks increased with a temperature increase; thus, the higher substrate temperature is beneficial for the growth of polycrystalline films. Furthermore, an increase in the GGI content shifts the reflection plane to higher 2θ values, in agreement with what was previously observed in the literature [93],[94]. This increase is evidenced in Fig. 41.

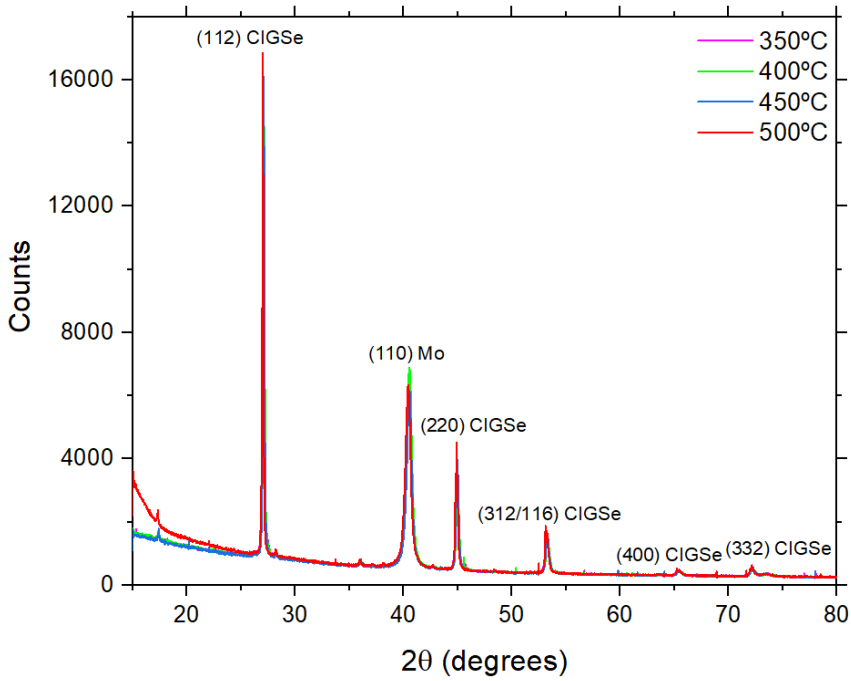

Figure 39. XRD pattern of CIGSe films deposited at 350 °C,400 °C,450 °C, and 500 °C after the KCN treatment.

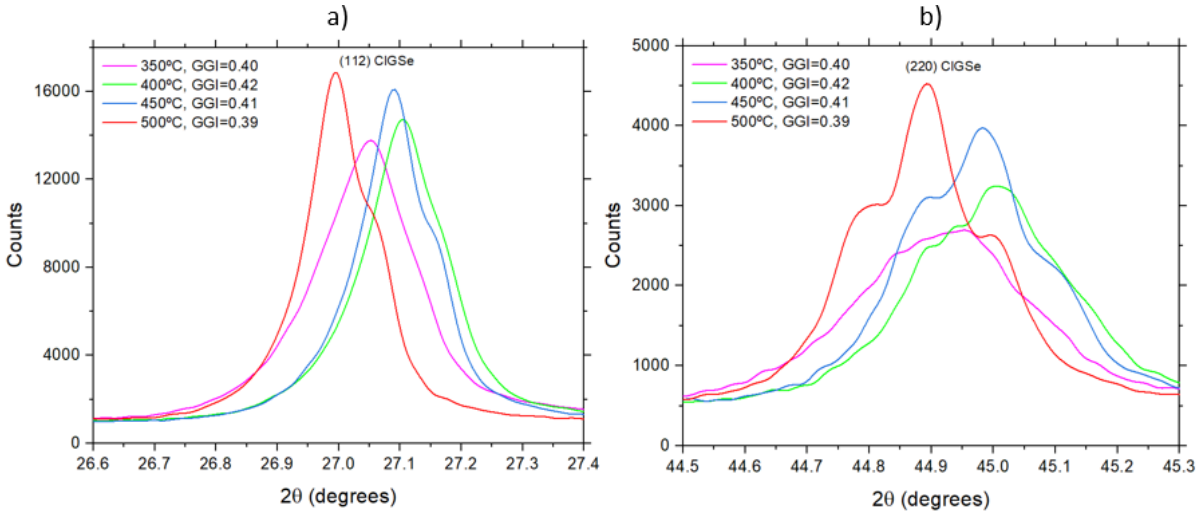

Figure 40. XRD pattern of CIGSe (a) (112) peak and (b) (220) peak for absorber layers deposited at 350 °C,400 °C,450 °C,500 °C.

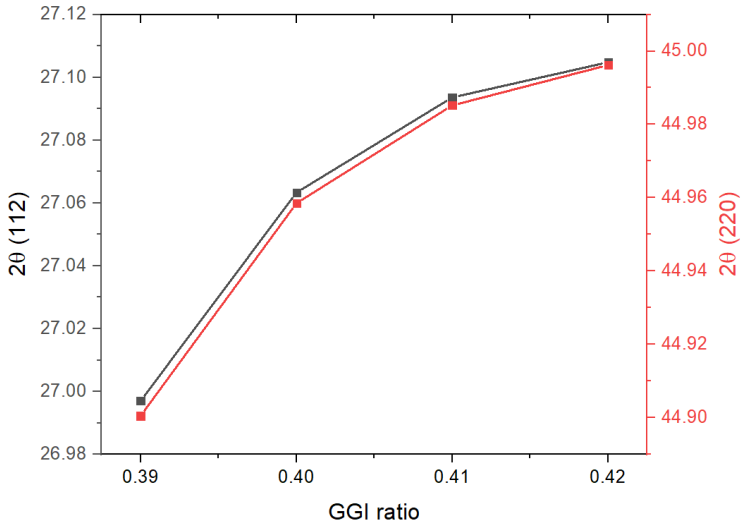

Figure 41. XRD diffraction angle dependence on GGI ratio for the (112) and (220) peaks for the temperature series.

Usually, efficient polycrystalline CIGSe films show a preferential orientation along the (112) or (220) planes [95]. The presence of Sodium has been noticed to have a strong influence on the CIGSe texture, as it tends to favor grain growth with a (112) preferred orientation [95]. Achieving a (220) textured CIGSe layer is therefore a challenging task, since the presence of Sodium is crucial for the solar cell performance, as stated in subchapter 2.4.3.

To evaluate the changes in the preferred orientation with the temperature variation, the texture coefficients for the most prominent peaks: (112), (220), and (312) were calculated using Eq. 12 and are shown in Fig. 42. It can be observed that all samples exhibit a preferential crystal orientation along the (112) plane, as the texture coefficient for this peak is greater than unity, and for the (220) and (312) peaks its values

are < 1. Furthermore, an increase in temperatures leads to a decrease in the texture coefficient of the (112) plane, meaning that lower temperatures are more favorable for crystallization along this orientation.

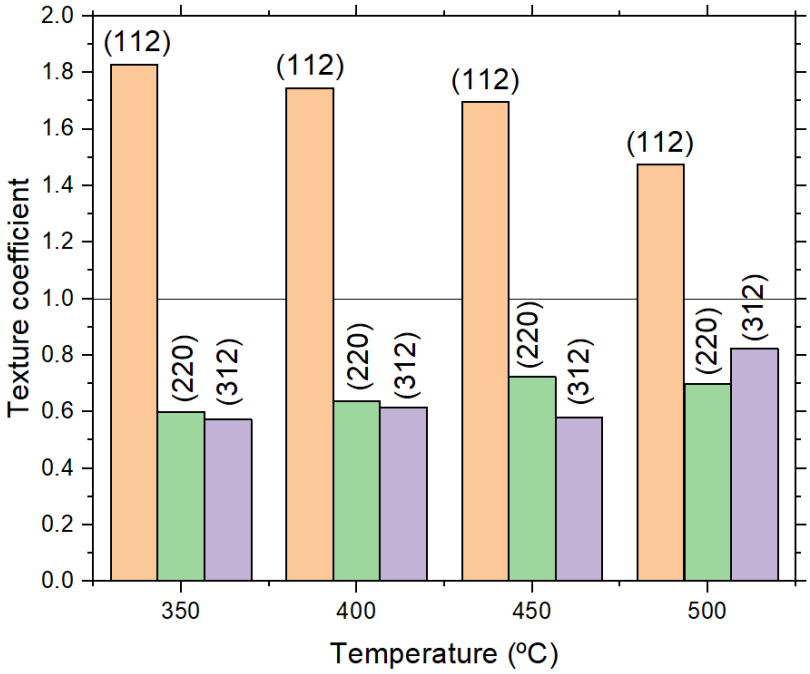

Figure 42. Texture coefficient of the different CIGSe peaks as a function of temperature.

To compare the grain size dependence on the growth temperature observed visually in the SEM images with data from the XRD characterization, the CIGSe crystallite size was calculated using the Scherrer equation (Eq. 11) with the (112) peak, as it is the preferential orientation of the CIGSe grains. A comparison of the obtained crystallite size values using the XRD results and an average of the surface grain size obtained in the SEM results for the different growth temperatures are displayed in Fig. 43 a) and b). When comparing the estimated crystallite size from the XRD measurement with the grain size observed from SEM measurements, it is expected that the grain size has larger values, because the grain sizes observed in SEM correspond to clusters of crystallites [96]. The SEM calculated grain size increases linearly with the temperature increase. The same behavior was obtained for the crystallite size dependence on temperature, except for the 500 °C absorber layer, which showed the same crystallite size as the one obtained for the 450 °C sample.

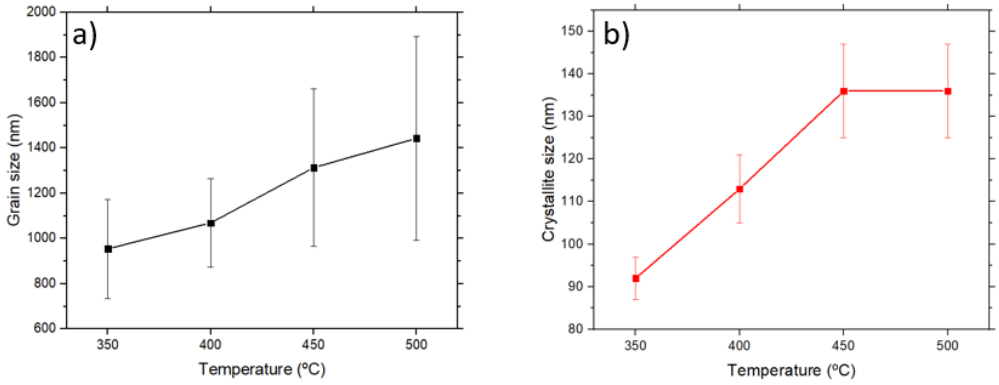

Figure 43. (a) CIGSe crystal sizes as a function of the temperature calculated with the average of the SEM analysis, (b) CIGSe crystallite calculated with the XRD measurements/Scherrer equation,

5.3 Solar cell analysis

Literature shows [85] that, in case of a Cu-rich CIGSe layer (i.e. leading to the formation of the Copper-Selenide phase), if no KCN treatment is done before the fabrication of the complete solar cell, the finished devices will be short-circuited. Thus, all of the CIGSe samples from the temperature series were submitted to a KCN-etching process, after which a CdS buffer layer was deposited by chemical bath deposition and an i-ZnO/ZnO:Al double layer was sputter-deposited as the front contact. As explained in section 4.3., the solar cells were manually separated into smaller solar cells, providing larger statistics, and ensuring that the current is collected from the whole cell. Fig. 44 shows the I-V curves of the best cells obtained for each temperature, from which the I-V parameters can be calculated.

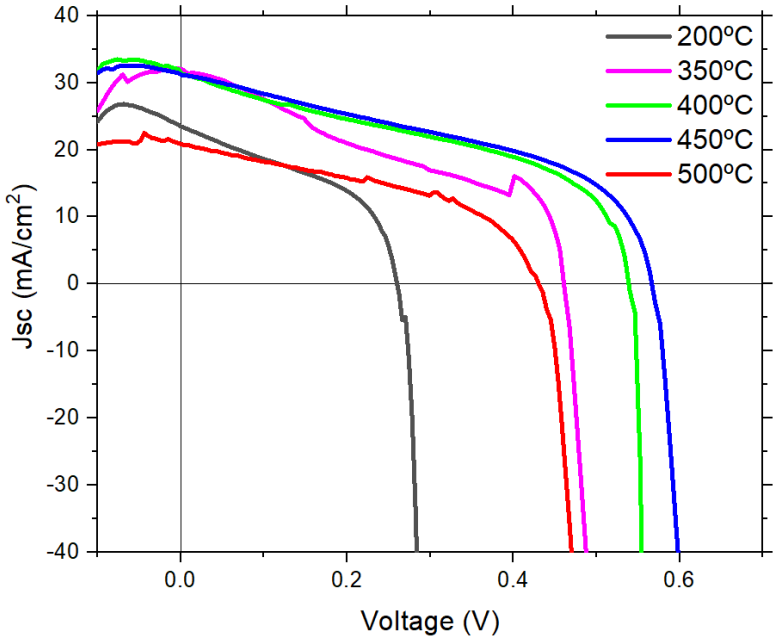

Figure 44. I-V curves of the best solar cells obtained for a CIGSe layer deposition temperature of 200 °C, 350 °C, 400 °C, 450 °C, and 500 °C. All the CIGSe layers were submitted to a KCN-etching process before the buffer layer deposition.

The box plots of the I-V parameters comparing the different deposition temperatures can be seen in Fig. 45. Table 8 displays the I-V parameters of the best performing cell and the average results of all measured cells.

The influence of temperature on solar cell efficiency is clear. The film deposited at 200 °C shows very low efficiencies in comparison with higher temperatures. The incorporation of Sodium in the CIGSe layer is known to improve the performance of the solar device [97], as it increases the cell efficiency, short-circuit current density, and open-circuit voltage (V_{oc}). The source of Sodium in the cells fabricated in this work is the soda-lime glass substrate, which requires a certain temperature to allow the diffusion of Na to the absorber layer. A deposition temperature of 200 °C might not be sufficient to cause the Na diffusion from the glass to the absorber layer. Besides this, the 200 °C sample exhibited worse XRD patterns (smaller peak intensities), and smaller grain size, explaining the low efficiencies, low current densities, and the low open-circuit voltage obtained for this sample.

Improved solar cell performances were found for higher deposition temperatures (>350 °C). An increase in temperature leads to an increase in efficiency, except for the 500 °C sample, where a big efficiency drop was observed, which can be attributed to a drop in V_{oc}, higher series resistance, and lower shunt resistance. A maximum efficiency of 8.4% was obtained, for the 450 °C CIGSe layer. The short-circuit current density was barely influenced by temperature, with average values ranging from 23.61 mA/cm^2 for 350 °C to 24.90 mA/cm^2 for 500 °C. The average values of V_{oc} increase from 0.42 V for 350 °C, to 0.54 V for 450 °C. As stated above, the 500 °C solar cell showed a huge drop in V_{oc}, displaying an average of 0.38 V. Low fill factor values between 40-50% were measured for all temperatures, while good CIGSe solar cells reach values between 65-85%, as seen in section 4.3.

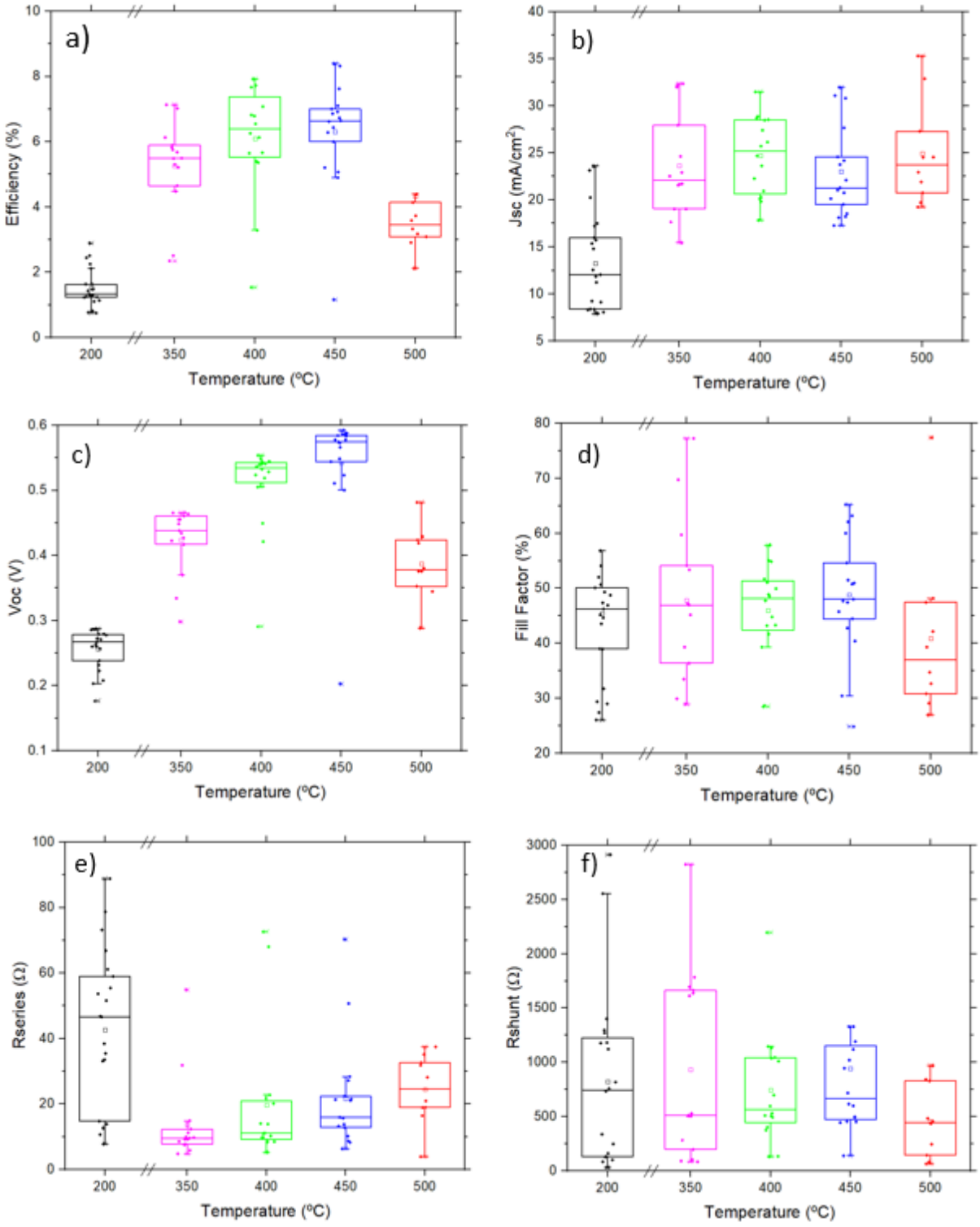

Figure 45. Box plot of (a) efficiency, (b) short-circuit current density, (c) open-circuit voltage, (d) fill factor, (e) series and (f) shunt resistances of CIGSe solar cells deposited under Cu-rich conditions with deposition temperatures of 200 °C, 350 °C, 400 °C, 450 °C, and 500 °C.

Table 8. Average and best solar cell I-V parameters obtained for CIGSe layer deposited under Cu-rich conditions with deposition temperatures of 200, 350, 400, 450, and 500 °C.

Temperature °C		Efficiency (%)	Jsc (mA/cm²)	Voc (V)	Fil Factor (%)	Rseries (Ω)	Rshunt (Ω)
200	Best cell	2.9	23.6	0.26	45	12.7	132
	Average	1.5 ± 0.6	13.3 ± 5.0	0.26 ± 0.03	45.0 ± 15.0	42.6 ± 24.3	823 ± 819
350	Best cell	7.02	32.4	0.46	45.18	5.8	1783
	Average	5.3 ± 1.4	23.6 ± 5.5	0.42 ± 0.05	47.8 ± 14.9	13.8 ± 12.9	935 ± 851
400	Best cell	7.9	31.5	0.54	44.8	11.1	375
	Average	6.1 ± 1.2	24.7 ± 3.8	0.51 ± 0.04	45.9 ± 7.3	19.8 ± 15.2	747 ± 500
450	Best cell	8.4	31.1	0.57	45.8	12.9	944
	Average	6.3 ± 1.8	23.0 ± 5.0	0.54 ± 0.1	48.8 ± 1.5	21.6 ± 17.1	944 ± 863
500	Best cell	4.4	20.7	0.43	47.4	20.9	1189
	Average	3.4 ± 0.7	24.9 ± 5.4	0.38 ± 0.05	40.9 ± 14.8	24.4 ± 10.4	455 ± 331

The 500 °C sample showed an odd behavior, where approximately half of the solar manifested a strong reverse-bias current leakage behavior, and had low shunt resistances, leading to not acceptable short-circuit current densities and efficiencies. For lower deposition temperatures, fewer cells had similar behavior, even though higher deposition temperatures lead to more frequent occurrence of this phenomenon. Cells showing this type of behavior were not considered in the I-V analysis described above. Some examples of such I-V curves and the respective I-V parameters are shown in Fig. 46 and Table 9. Even though a clear reason is yet to be understood, some possible explanations for the observed behavior are given here.

T. Hsieh et al. [85] observed a similar I-V curve response. They attributed it to the KCN-etching treatment, which forms voids at the grain boundaries that in turn may act as pinholes leading to current leakage and damaging the CdS/CIGSe interface.

Another possible explanation for the observed phenomenon is that, due to the high deposition temperature and the high GGI ratios, the Copper-Selenide phase, besides being present at the surface, diffuses to deeper regions of the absorber layer and might not be completely removed by the KCN treatment (as observed by P.Tsoulka et al. [98]), which attacks mainly the surface of the film. The Raman analysis conducted in this work is believed to only access the surface of the CIGSe layer (up to 100 nm in depth). Hence, if Cu-enriched regions are present within the layer, they would not be detected by Raman. The presence of this undesired phase would be detrimental for solar cell performance and explain the obtained results. Also noteworthy, is that the actual substrate temperature is slightly higher than the

stated nominal values, due to the position of the thermocouple at the backside of the sample heater. The temperature difference can be in the order of 50 - 70°C, which was estimated based on SLG substrate bending [104]. Thus, for the 500 °C nominal temperature, the actual temperature might be as high as 570°C.

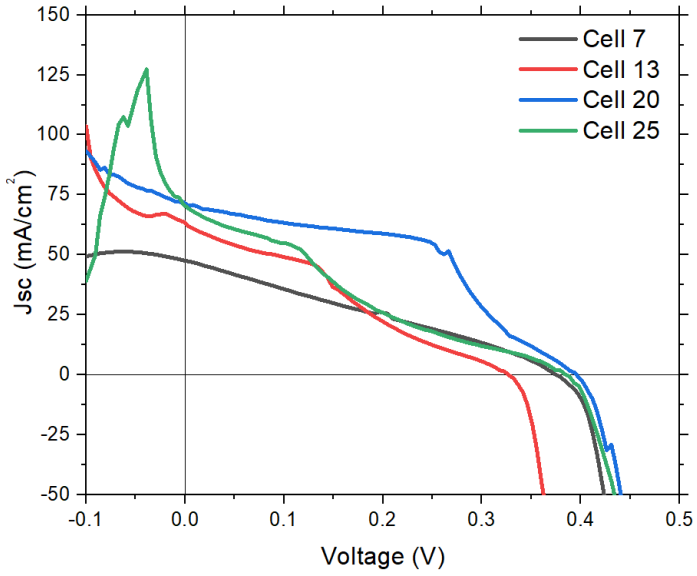

Figure 46. I-V curve of 500 °C solar cells that exhibit a reverse-bias current leakage.

Table 9. I-V parameters of the solar cells shown in Fig. 46.

Cell	Efficiency (%)	Jsc (mA/cm²)	Voc (V)	Fil Factor (%)	Rseries (Ω)	Rshunt (Ω)
7	5.1	47.6	0.37	27.7	19.0	163
13	6.3	62.5	0.32	29.9	22.2	44
20	14.3	71.6	0.39	49.1	18.9	66
25	6.0	72.7	0.39	20.9	16.4	249

6. INDIUM POST DEPOSITION

Following the issues identified in the previous chapter, which are believed to be a consequence of the KCN-etching process, a different approach to consume the residual Copper-Selenide phase obtained during the absorber layer growth will be studied. High-efficiency $Cu(In,Ga)Se_2$ thin-film solar cells are typically fabricated by a multi-stage co-evaporation process, where one of these stages leads to a Cu-rich composition, and the other stages are Cu-deficient, balancing out the overall Copper atomic percentage [5]. Here, a 2-stage sputtering process for the CIGSe layer will be developed. The first stage, consisting of the sputtering of the Cu-rich CIG target, will lead to the Cu-rich films. In the second stage, Indium will be deposited using a 99.999% purity Indium-sputtering target. In both stages, Selenium will be simultaneously supplied to the sample via the pulsed valved-cracker evaporation source. The ultimate goal is to eliminate the presence of the undesired $Cu_{2-x}Se$ phase without the need for the KCN-etching process.

All absorber layers described in this chapter were deposited at substrate temperature of 500 °C. Thus, with the Indium post-deposition (PD), the aim is to significantly improve the results obtained for the 500 °C deposition temperature. Higher thermal energies should favor the diffusion of Indium within the absorber layer, and Cu-rich conditions are known to also favor this diffusion [99]. The remaining deposition parameters are kept constant as defined in the previous chapter: P_{CIG} = 30W; $p=5.5\times10^{-3}$ mbar; Se valve opening of 9 mm; 0.1 s ON/0.9 s OFF Selenium pulses

6.1 Characterization of the absorber layer

Two CIGSe layers with different Indium post-deposition thicknesses will be studied. Using the EDX results obtained in the previous chapter for a deposition temperature of 500°C with an accelerating voltage of 30 keV, the experiment was designed to obtain the desired stoichiometries (i.e. the deposition thickness with the CIG and the Indium targets were estimated (see Table 10) taking into consideration the materials weight densities and atomic weight). The first sample consists of 1500 nm of CIGSe deposited with the Cu-rich target and 500 nm of Indium and Selenium. It is estimated that, for such thickness values, a CGI ratio of 0.96 and GGI ratio of 0.25 are obtained. The second sample consists of 1400 nm of CIGSe deposited with the Cu-rich target and 600 nm of Indium and Selenium, where a CGI ratio of 0.87 and a GGI ratio of 0.23 were predicted. The total thickness of both samples will be 2 μm, allowing a proper comparison with the results obtained in the previous chapter.

Table 10. Estimated stoichiometry of CIGSe films with Indium PD for different deposition thicknesses using a CIG and a In target, with a simultaneously supply of Selenium.

CIGSe thickness (nm)	In-Se thickness (nm)	# Cu atoms (/cm²)	# In atoms (/cm²)	# Ga atoms (/cm²)	CCI ratio	GGI ratio
1500	500	2.82×10^{18}	2.17×10^{18}	7.51×10^{18}	0.96	0.26
1400	600	2.63×10^{18}	2.31×10^{18}	7.01×10^{18}	0.87	0.23

SEM images of the Indium PD CIGSe layers before the KCN treatment are shown in Fig. 47. Both Indium PD samples exhibit large crystals, comparable with the size obtained for a CIGSe layer deposited without the Indium treatment. The sample with 1400 nm CIGSe and 600 nm In-Se sample shows slightly larger crystals (2.5 μm) than sample with 1500 nm CIGSe and 500 nm In-Se (2μm crystals). The result of the sample with only 2000nm CIGSe without the Indium PD, deposited at 500°C (this sample will be referred to as "2000 nm CIGSe") is also shown (after KCN treatment), to facilitate the comparison between the different approaches. The grain boundaries obtained for the Indium PD approach are not as pronounced as those obtained in Chapter 5, and there is a significant decrease in holes near the grain boundaries.

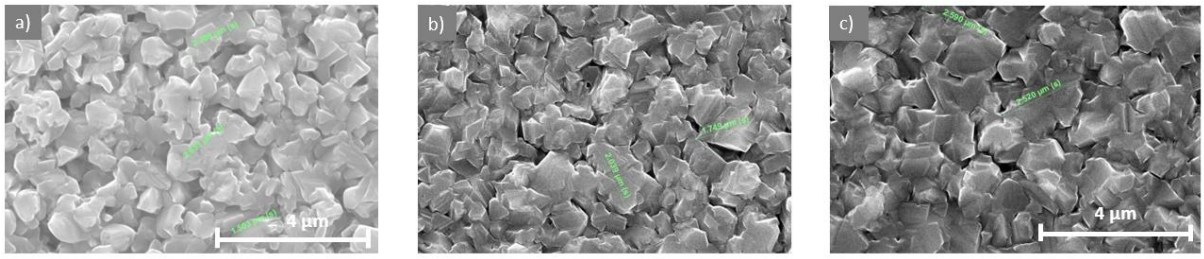

Figure 47. SEM Images of CIGSe thin films for samples deposited as (a) 2000 nm CIGSe after the KCN-etching (b) 1500 nm CIGSe followed by 400 nm In-Se, before the KCN-etching, and (c) 1400 nm CIGSe followed by 600 nm In-Se, before the KCN-etching.

Quantification of the bulk elemental concentrations of Cu, In, Ga, and Se obtained by EDX analysis were performed with two different accelerating voltages: 20 and 30 keV. The different accelerating voltages allow a more surface-sensitive result (20 keV) and a composition from deeper within the film (30 keV). The results are presented in Table 11 and allow to evaluate if the post-deposited Indium diffused through the film. Fig. 48 shows the variation of the CGI, GGI, and Selenium ratios, obtained for an accelerating voltage of 30 keV.

One can conclude that the post-deposited Indium successfully diffused through the absorber, seeing that there was an increase in Indium atomic percentage of 3 to 4% for higher accelerating voltages, and the

GGI ratio remained constant. To confirm this, a cross sectional analysis of the 1400nm CIGSe and 600nm In-Se film was performed (see Fig. 49), where it can be seen that the film is homogenous (i.e. it is not possible to detect where the CIGSe deposition ended and the In-Se deposition began). For the 2000 nm CIGSe sample, the Gallium concentration barely varies with increasing accelerating voltage, yet the GGI ratio is significantly lower for increasing accelerating voltages meaning that Indium is more concentrated in the front part of the film. As intended, both samples with post-deposited Indium show Cu-poor stoichiometries for a 30 keV accelerating voltage before the KCN treatment (Cu at% <25 and CGI ratio <0.90) and exhibit lower GGI ratios, ranging from 0.24 to 0.26 in comparison with the high GGI ratios for the 2000 nm CIGSe sample. Thus, it is possible to conclude that both Indium PD experiments were successful since the ideal CIGSe stoichiometries presented in subchapter 2.4.3. where achieved, while maintaining the enhanced grain size due to the initial Cu-rich growth conditions. The PD-Indium films were also submitted to the KCN-etching to see if this treatment had a significant impact on the film's stoichiometry. There was a slight decrease in Copper composition and CGI ratio following the KCN-etching process, even though this decrease was much smaller than the one obtained for the 2000 nm CIGSe absorber layer. Thus, the presence of very small amounts of an impurity phase of $Cu_{2-x}Se$ cannot be completely excluded based on the EDX analysis.

Table 11. Chemical composition of the CIGSe absorber layers deposited at 500°C with and without Indium PD, obtained by EDX analysis with 20 and 30 keV accelerating voltages.

Sample	Accelerating Voltage (keV)		Cu (at%)	Ga (at%)	In (at%)	Se (at%)	CGI ratio	GGI ratio	SCGI ratio
2000nm CIGSe	20	Before KCN	38.7	8.6	7.7	45.0	2.38	0.53	0.82
		After KCN	22.5	11.2	13.8	52.5	0.90	0.45	1.11
	30	Before KCN	34.7	8.4	12.0	44.9	1.70	0.41	0.81
		After KCN	24.0	10.7	16.9	48.4	0.87	0.39	0.94
1500nm CIGSe 500nm In-Se	20	Before KCN	23.5	6.2	18.3	52.0	0.96	0.25	1.08
		After KCN	22.4	6.5	18.3	52.8	0.90	0.26	1.12
	30	Before KCN	24.0	7.3	21.1	47.6	0.85	0.26	0.91
		After KCN	23.2	7.1	21.5	48.2	0.81	0.25	0.93
1400nm CIGSe 600nm In-Se	20	Before KCN	24.3	5.6	18.1	52.0	1.03	0.24	1.09
		After KCN	22.6	5.8	19.4	52.2	0.90	0.23	1.09
	30	Before KCN	24.2	6.7	21.5	47.8	0.86	0.24	0.91
		After KCN	23.3	6.8	21.9	48.0	0.81	0.24	0.92

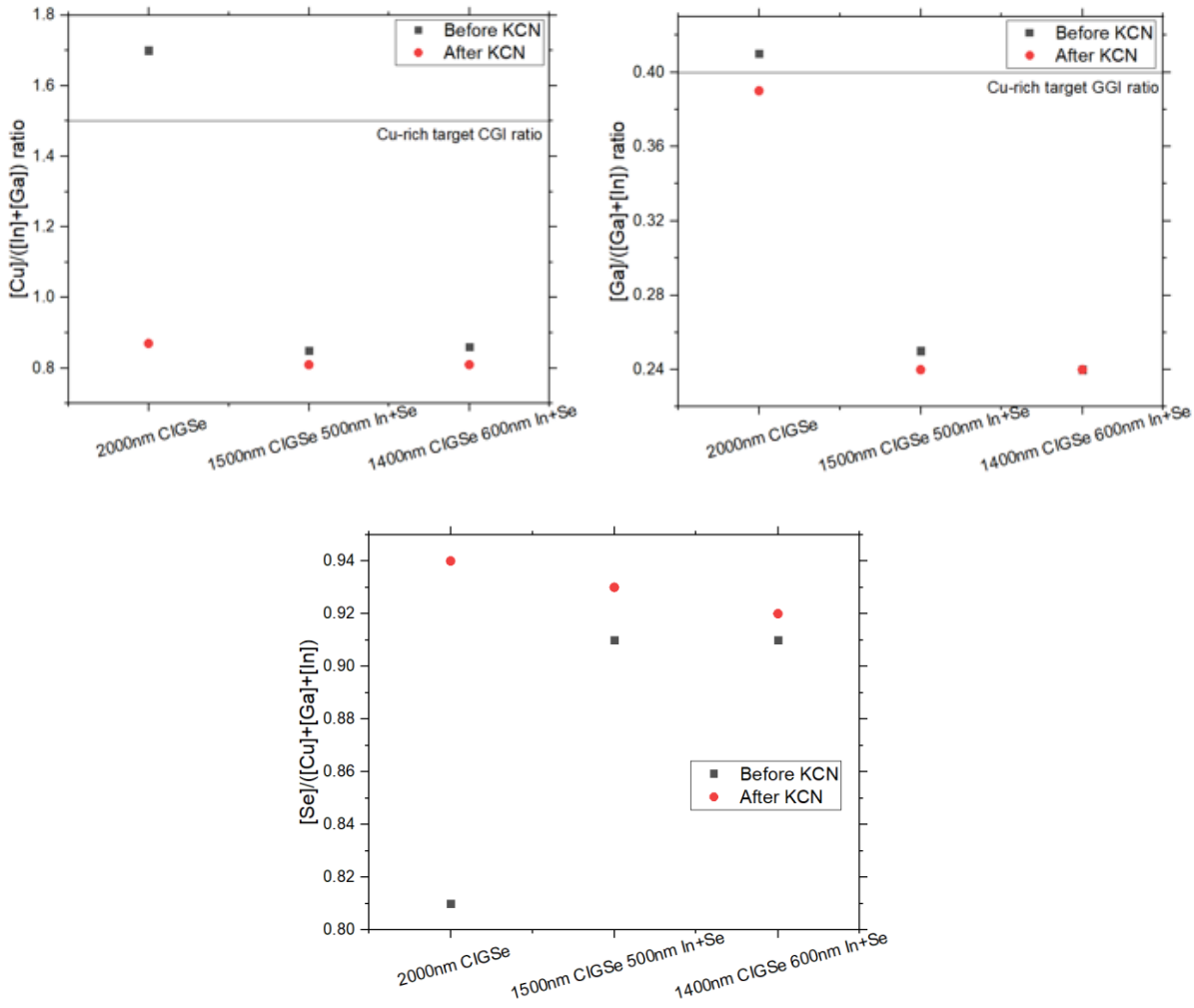

Figure 48. Evolution of the stoichiometry ratios with different Indium PD supplies, obtained by EDX analysis with a 30 keV accelerating voltage.

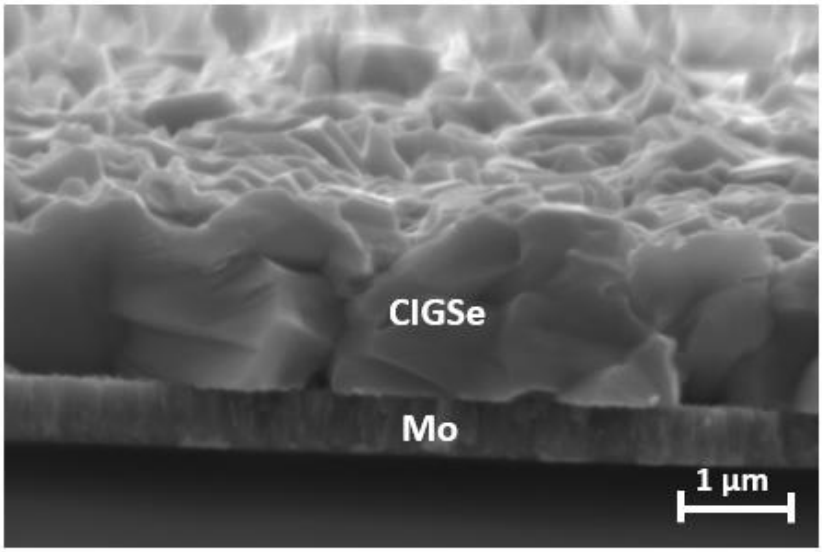

Figure 49. Cross section view of the 1400nm CIGSe and 600nm In-Se thin-film.

The EDX analysis showed Cu-poor stoichiometries for both samples with the Indium PD, suggesting that no Copper-Selenide should be present. To check this hypothesis, Raman spectroscopy was performed. Since the sputtering deposition is not homogenous, owing to the use of two different targets with different orientations to the sample, which can lead to slight inhomogeneity in the deposited layers, Raman spectroscopy was performed on several spots of the sample. The 1400nm CIGSe / 600nm In-Se sample did not exhibit any $Cu_{2-x}Se$ phase, however, the 1500nm CIGSe / 500nm In-Se sample revealed a small $Cu_{2-x}Se$ peak in the closest spot to the Selenium source and furthest spot away from the Indium target (Fig. 50). The intensity of this peak is much smaller in comparison with the one observed in the previous chapter, owing to the inferior atomic percentage of Copper. After the KCN-etching treatment, this compound was successfully removed.

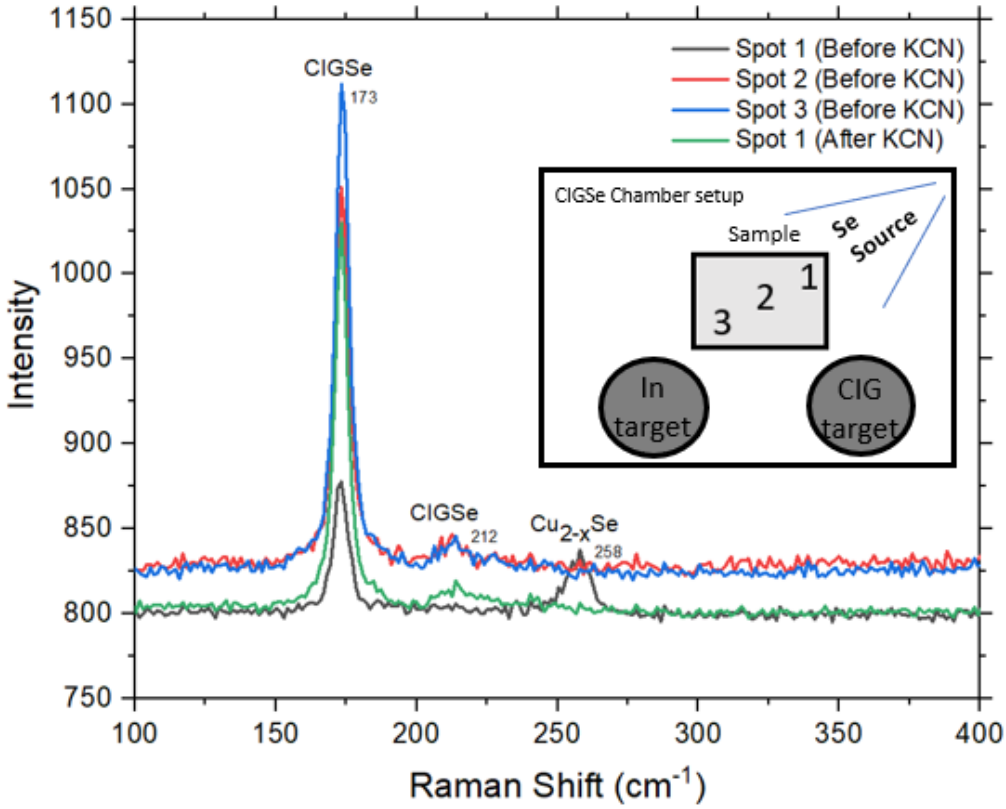

Figure 50. Raman spectra of the 1500nm CIGSe 500nm In-Se sample taken at different spots as illustrated in the sketch in the inset (the geometry of the Se source, CIG and In targets is also indicated), before and after KCN-etching.

The XRD pattern of both Indium PD absorber layers and the 2000 nm CIGSe film is shown in Fig. 51. As already observed for the 2000 nm CIGSe film (see Fig. 42), the PD Indium films appear to show a preferential orientation along the (112) plane and other CIGSe orientations corresponding to the (220),

(312/116), (400), and (332) planes were detected. The absorbers with Indium PD show significantly smaller peak intensities for all of the CIGSe peaks. The CIGSe peak intensities of the 1500 nm CIGSe sample are greater than the peak intensities of the 1400 nm CIGSe layer. Furthermore, there is a clear shift of the reflection planes to lower 2θ angles for lower GGI values. This can be seen more clearly in Fig. 52, which shows a zoomed-in image of the (112) and (220) planes, and in Fig. 53, where the angle shift dependence on the GGI ratio is plotted, for both planes.

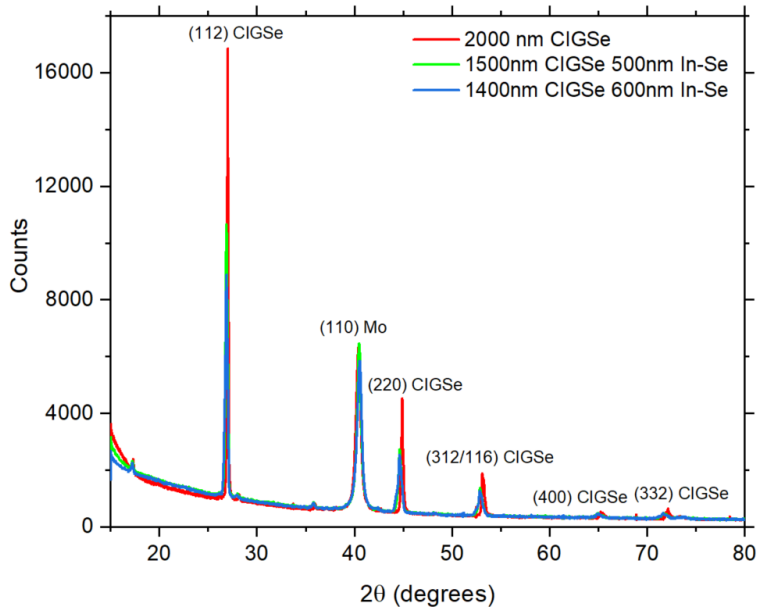

Figure 51. XRD pattern of CIGSe films with Indium PD before KCN treatment, and the 2000 nm CIGSe sample after KCN treatment. All films were deposited at 500 °C.

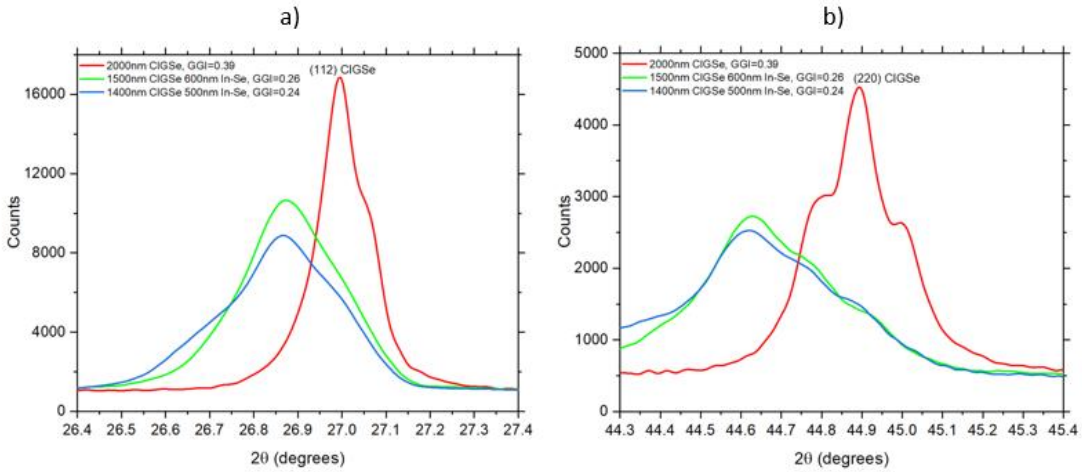

Figure 52. XRD pattern of CIGSe (a) (112) peak and (b) (220) peak for absorber layers with the Indium PD before KCN treatment, and the 2000 nm CIGSe after KCN treatment. All films were deposited at 500 °C. The GGI values presented are the ones obtained for an accelerating voltage of 30 keV.

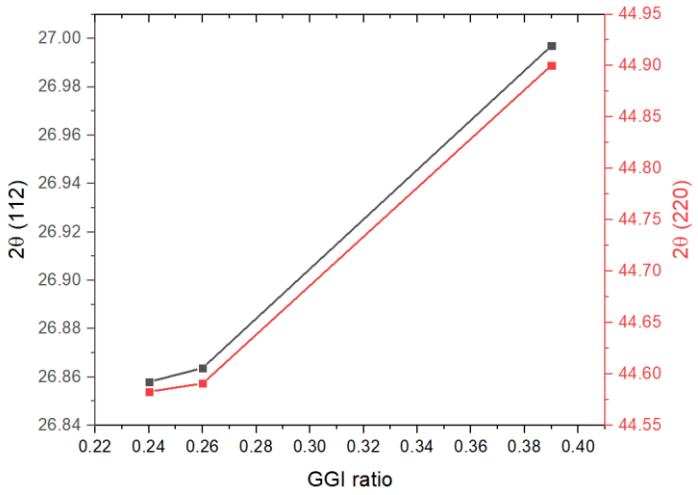

Figure 53. XRD diffraction angle dependence on GGI ratio for the (112) and (220) peaks.

The texture coefficient of the (112), (220), and (312) CIGSe planes for the 2000 nm CIGSe and Indium PD layers are shown in Fig. 54. The Indium PD did not have a significant impact on the preferential orientation of the CIGSe crystals, since both samples exhibit a preferential orientation along the (112) plane. However, is it evident that the significant decrease in the GGI ratio leads to an increase in the texture coefficient of the (112) peak, thus favoring, even more, the crystallization along this plane. Furthermore, there was also a significant decrease in the (312) orientation texture coefficient for the Indium PD samples.

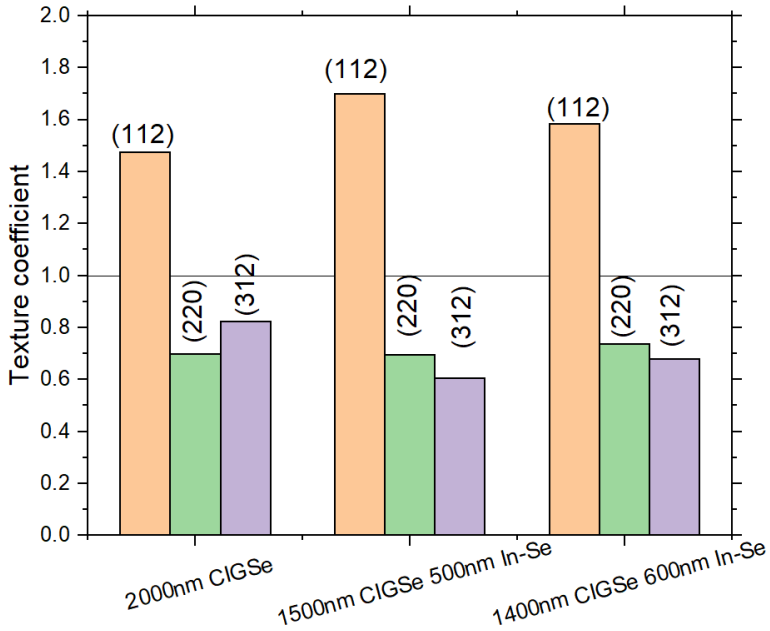

Figure 54. Texture coefficient of the different CIGSe peaks for absorber layers with the Indium PD before KCN treatment, and the 2000 nm CIGSe after KCN treatment.

The average of the surface grain size obtained in the SEM results and the crystallite size obtained using the XRD results are displayed in Fig. 55. All films have identical average surface grain size, confirming that the Indium PD didn't have an impact on the grain size and that the grain size is determined during the Cu-rich stages of the growth. Thus, it was expected that the crystallite size for all samples should also be similar. However, such behavior was not observed, as the 2000 nm CIGSe layer exhibited larger crystallite sizes than both Indium PD samples. In the literature, it has been reported that a variation of the GGI ratio affects the grain and crystallite size, assuming a fixed CGI ratio [100], [101]. An increase in the GGI leads to an increase in the grain/crystallite size until a certain GGI value is reached, while for higher GGI ratios a decrease in the grain/crystallite size is reported. Different studies report different values for the GGI ratio with maximum garin/crystallite size, in the range between 0.2 and 0.45(see Fig. 56) [100], [101].

However, in the present study, there is a convolution of two effects, since the CGI ratio and GGI ratio are changed simultaneously during the Indium PD, which has not been reported in literature yet. The observed results indicate that the grain size is not dependent on the GGI ratio, but the crystallite size follows the trend observed in the literature (i.e. an increase in GGI ratio results in larger crystallites). The threshold value that limits the crystallite size increase with the GGI ratio is unknown, since there are not sufficient data points.

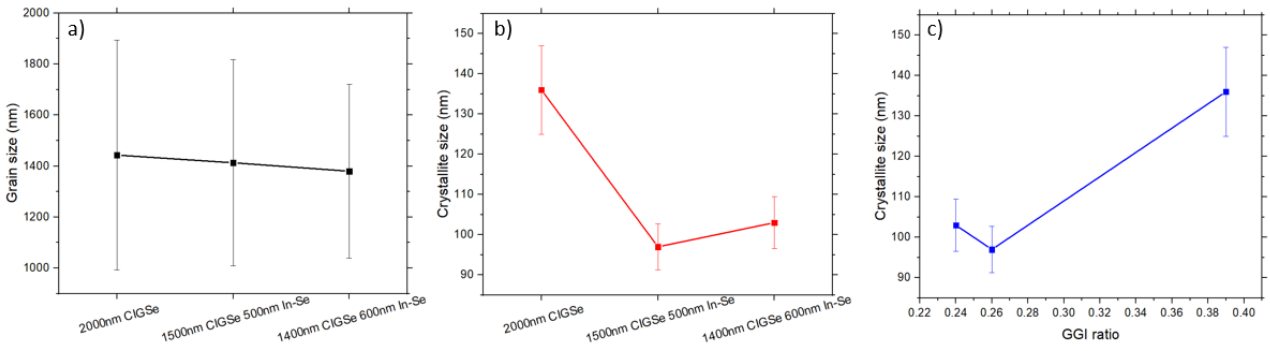

Figure 55. CIGSe crystal sizes for absorber layers with the Indium PD before the KCN treatment, and the 2000 nm CIGSe after the KCN treatment calculated with the average of the SEM analysis, (b) CIGSe crystallite sizes calculated with the XRD measurements/Scherrer equation, and (c) CIGSe crystallite size dependence on the GGI ratio

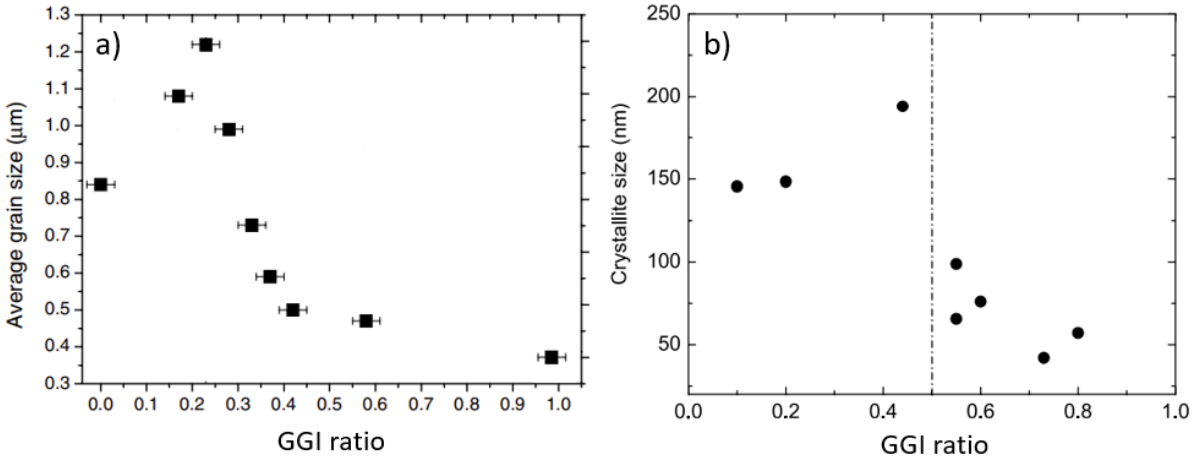

Figure 56. (a) Average grain size in CIGSe thin films for different GGI ratios obtained from Electron backscatter diffractions (EBSD) maps. The average grain size increases from 0 ≤ GGI ≤ 0.23 and decreases for 0.23 ≤ GGI ≤ 1. Image adapted from [101]. *(b) Dependence of the crystallite size dependence on the GGI ratio, derived from XRD pattern data* [100].

Another important parameter one can extract from the XRD data is the lattice parameters (a and c) of the absorber layer. The lattice parameters, shown in Table 12, were calculated using the interplanar spacing equation for the tetragonal systems (Eq. 8), and the information of the (112) and (220) peaks. Unlike what was observed for the grain size, which was independent of the final composition of the film, the lattice parameters are dependent on the final composition of the absorber layer. An increase of the lattice parameters (a from 5.70Å to 5.74Å, and c from 11.47Å to 11.50Å) was observed for a decrease in GGI ratio (from 0.39 to 0.24), which is in agreement with previous literature reports [100], [102]. The replacement of Gallium ions for Indium ions, leading to lower GGI ratios, causes an increase in the lattice parameters because the Indium ions (0.81Å) are larger than the Gallium ions (0.61Å). Balboul et al. [100] showed a correlation between the c/a ratio and solar cell efficiency, where the best-performing cells had a c/a ratio of 2.0, likewise obtained for both Indium PD samples.

Table 12. Influence of [Ga]/([Ga]+[In]) ratio on the lattice parameters for absorber layers with the Indium PD before the KCN treatment, and the 2000 nm CIGSe after the KCN treatment

Sample	GGI ratio	c (A°)	a (A°)	c/a
2000 nm CIGSe	0.39	11.47	5.70	2.01
1500 nm CIGSe 500 nm In-Se	0.26	11.49	5.74	2.00
1400 nm CIGSe 600 nm In-Se	0.24	11.50	5.74	2.00

6.2 Solar cell analysis

To conclude the Indium PD study, solar cells for both Indium PD experiments were completed without the step of the KCN treatment. A CdS buffer layer was deposited by chemical bath deposition, and an i-ZnO/ZnO:Al double layer was sputter-deposited as the front contact. To see the influence of the KCN-etching treatment on the solar cell performance, an extra sample of the 1400 nm CIGSe and 600 nm In-Se was grown and submitted to the KCN-etching. The solar cell results of the 2000 nm CIGSe layer are also shown, to allow a proper comparison between the two different methods. The I-V curves of the best performing cell for each sample are shown in Fig. 57.

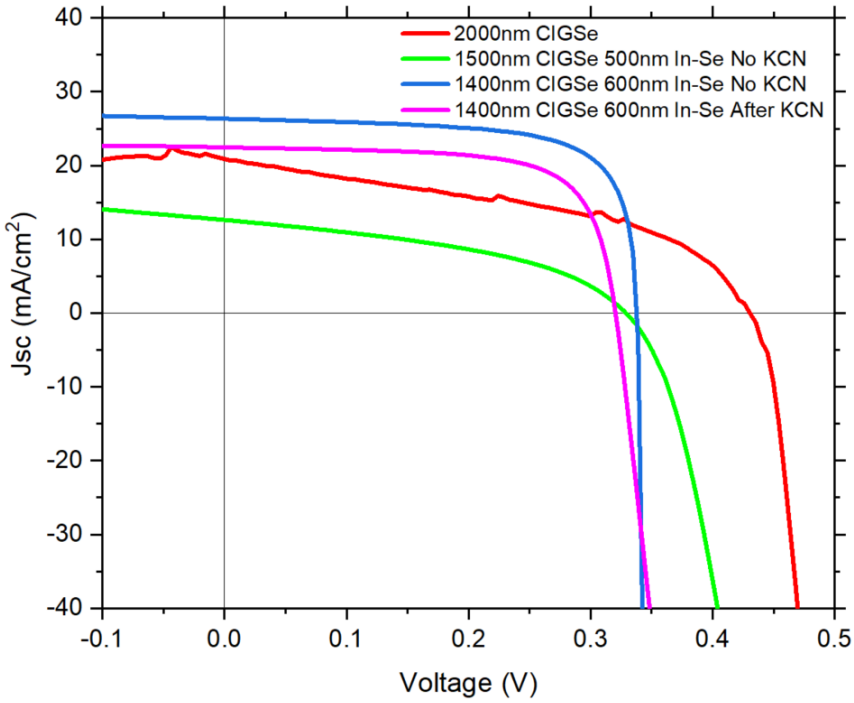

Figure 57. I-V curves of the best solar cells obtained for the 2000nm CIGSe and Indium PD samples. All films were deposited at 500 °C.

The box plots of the I-V parameters comparing the different deposition processes can be seen in Fig. 58. Table 13 displays the I-V parameters of the best performing cell and the average results of all measured cells.

For the 1500 nm CIGSe and 500 nm In-Se sample, only one cell worked, showing an efficiency of 1.8%. All other cells were short-circuited and, therefore, did not work properly. Although this sample was deposited with the same sputtering conditions as shown in the previous sub-chapter, where the sample only had $Cu_{2-x}Se$ in one corner of the sample, it is believed that for this deposition, Copper-Selenide was

distributed throughout the sample, thus deteriorating its performance, also explaining the very low shunt resistance and high series resistances.

For the 1400 nm CIGSe / 600 nm In-Se sample without the KCN treatment, different results were obtained. All of the solar cells worked (indicating that no $Cu_{2-x}Se$ was present on the film), exhibiting an average efficiency of 6.1%, which was a good improvement when in comparison with the 3.4% average efficiency obtained for the 2000 nm CIGSe sample (with KCN treatment). The J_{sc} showed a slight improvement of almost 1 mA/cm^2, while the open-circuit voltage decreased from 0.38 V to 0.33 V, owing to the smaller GGI ratios, as reported in the literature [102]. Besides the large efficiency enhancement, there was also a big increase in fill factor, where this sample showed an average FF of 67.2%, comparing to the average FF of 40.9% obtained for the 2000 nm CIGSe sample. Lower series resistances and higher shunt resistances were also obtained for the Indium PD absorber. Furthermore, all of the solar cells had very similar I-V values, meaning that the sample was very homogenous.

The 1400 nm CIGSe / 600 nm In-Se sample submitted to the KCN-etching process showed worse performance than the one without KCN. The average efficiency, open-circuit voltage and fill factor for this sample were 3.7%, 0.25 V, and 53.8%, respectively, in comparison with the average 6.1% efficiency, 0.33 V V_{oc}, and 67.2% FF, obtained for the sample without KCN. Moreover, approximately half of the divided solar cells had the same reverse-bias current leakage problem as seen for the 2000 nm CIGSe cell, showing very high short-circuit current densities and low shunt resistance (see discussion in section 5.3.). Thus, it is possible to conclude that the Indium PD approach is beneficial for solar cell performance, at least for deposition temperatures of 500 °C, and that the KCN-etching process is detrimental for the performance of the solar cells when the overall composition is already Cu-poor.

Table 13. Average and best solar cell I-V parameters obtained for 2000nm CIGSe and Indium PD samples.

Sample		Efficiency (%)	Jsc (mA/cm²)	Voc (V)	Fil Factor (%)	Rseries (Ω)	Rshunt (Ω)
2000 CIGSe (With KCN)	Best cell	4.4	20.7	0.43	47.4	20.9	1189
	Average	3.4 ± 0.7	24.9 ± 5.4	0.38 ± 0.05	40.9 ± 14.8	24.4 ±1 0.4	455 ± 331
1500 CIGSe 500 In-Se (No KCN)	Best cell	1.8	12.6	0.33	42.6	42.9	443
	Average	0.2 ± 0.5	2.2 ± 3.3	0.06 ± 0.09	26.4 ± 5.3	182.0 ± 81.4	229 ± 105
1400 CIGSe 600 In-Se (No KCN)	Best cell	6.7	26.3	0.34	72.1	1.5	1088
	Average	6.1 ± 0.4	25.9 ± 1.6	0.33 ± 0.01	67.2 ± 5.8	3.3 ± 1.6	845 ± 692
1400 CIGSe 600 In-Se (With KCN)	Best cell	5.3	22.5	0.32	70.43	4.6	1898
	Average	3.7 ± 1.3	24.6 ± 3.4	0.25 ± 0.07	53.8 ± 14.9	6.5 ± 2.2	455 ± 331

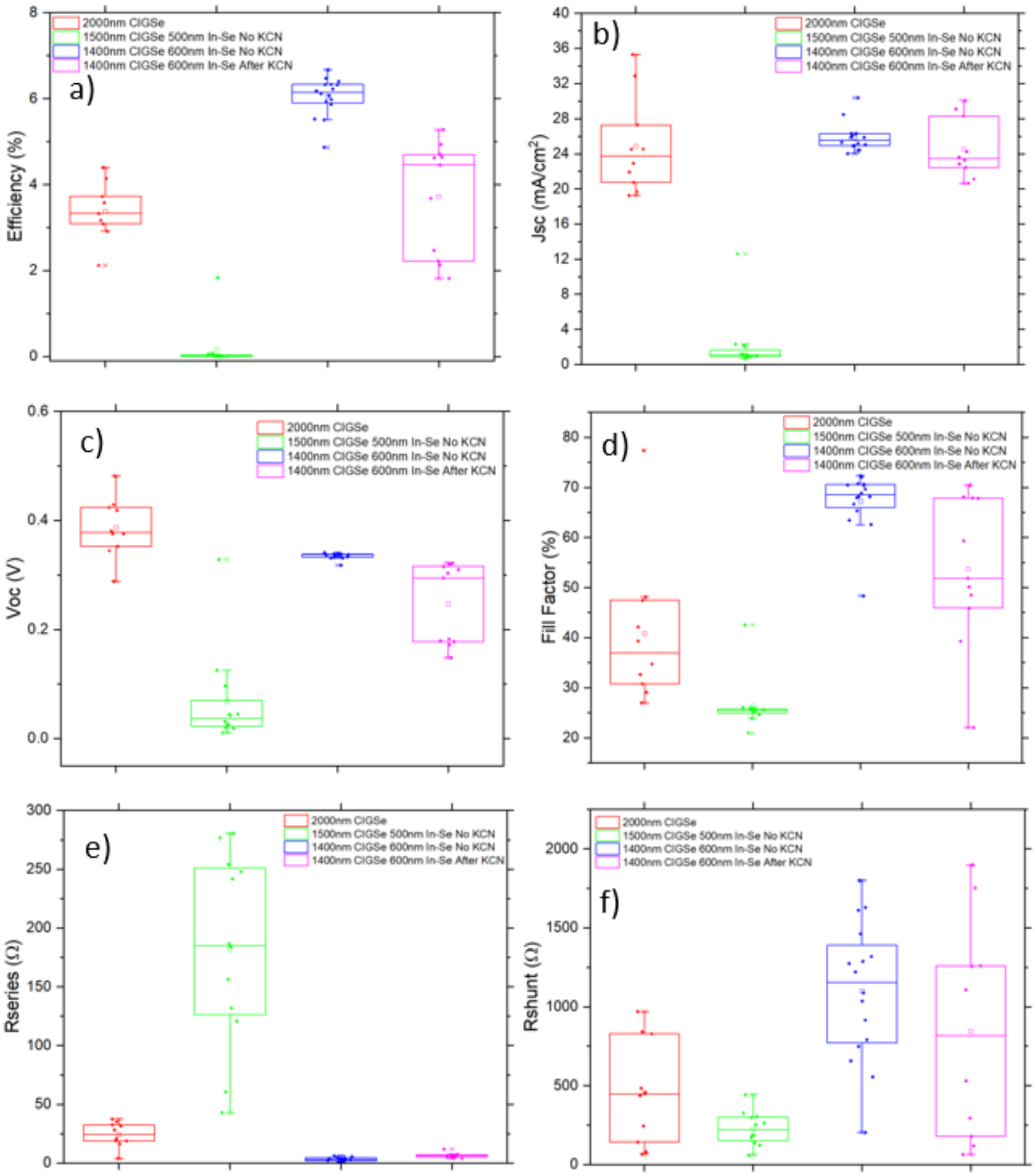

Figure 58. Box plot of (a) efficiency, (b) short-circuit current density, (c) open-circuit voltage, (d) fill factor, (e) series and (f) shunt resistances for the 2000 nm CIGSe and Indium PD samples.

7. Conclusions and Future work

In the present work, CIGSe layers were deposited with a Cu-rich CIG target, which is known to improve the grain size but, as a disadvantage, leads to the presence of an undesired Copper-Selenide phase on the CIGSe thin-film. Additionally, the deposited films show a rather high GGI ratio, due to a high Ga content in the CIG target. The objective of this thesis was twofold: to understand the influence of temperature and GGI ratios on the absorber layer properties and solar cell performance, and to test two different approaches to eliminate the undesired Copper-Selenide phase, (i) KCN-etching treatment, and (ii) Indium post-deposition.

The initial studies, which consisted of depositing absorber layers without Indium post-deposition (i.e. high GGI ratios will be obtained) at different temperatures, and a subsequent KCN-etching process to remove the Copper-Selenide phase, revealed that a temperature increase results in an increase in grain size, which is expected to be beneficial for solar cell performance. However, all films exhibited very well pronounced grain boundaries and holes near the grain boundaries. The density of holes increased with the temperature increase. Solar cell results showed that an increase in temperature from 200 °C up to 450 °C causes an efficiency improvement. However, the 500 °C samples did not follow this trend, as poor solar cell performances were obtained. Unrealistic short-circuit current densities were measured and the I-V curves showed a reverse-bias current leakage behavior. Two possibilities to explain this phenomenon were discussed, (i): the KCN-etching process forms some voids at grain boundaries which may act as pinholes leading to current leakage and damaging the CdS/CIGSe interface, and (ii): as a result of the high deposition temperature and high GGI ratios, the Copper-Selenide phase migrates towards deeper regions of the film and is not removed upon exposure of the CIGSe layer to the KCN solution. Best efficiency of 8.4% and average efficiency of 6.3% were obtained for a deposition temperature of 450 °C.

To improve the results obtained for solar cells with 500 °C deposited absorber layers, CIGSe layers were deposited at this temperature, followed by an Indium post-deposition. The Indium post-deposition was successful since the Copper-Selenide phase was fully converted into CIGSe, thereby eliminating the need for the KCN-etching process while maintaining the enhanced grain size promoted by the initial Cu-rich conditions. The films were more compact, exhibited less pronounced grain boundaries, and the density of holes in the film decreased significantly. Furthermore, the smaller GGI ratios obtained for the Indium post-deposition had a notable impact on the crystalline properties of the absorber, as there was a shift in the XRD diffraction angle towards smaller angles, the crystallite size decreased, the lattice parameters increased, and the preferential growth along the (112) orientation was enhanced. Solar cell results of one

of the Indium PD-samples without the KCN treatment revealed an improved performance (an average efficiency of 6.1% was obtained, in comparison to the 3.4% obtained for the sample with the KCN-treatment and no Indium post-deposition). Additionally, the CIGSe absorber layer that showed an average efficiency of 6.1% was replicated, but this time, it was submitted to a KCN-etching treatment. There was a performance decrease, since the average measured efficiency for the latter sample was 3.5%, thus indicating that, for the case of the samples with Indium PD (i.e. the samples already have Cu-poor stoichiometries), the KCN-etching is detrimental for the solar cell performance.

For future work, and to better understand the KCN-etching impact, the duration of such process and the concentration of the KCN-solution could be varied. Related to the Indium post-deposition, a possible study would be the optimization of the amount of supplied Indium and to lower the deposition temperature to 450°C, as this temperature showed the best efficiency obtained in this thesis. Finally, varying the Selenium pulse duration could also result in improved solar cell performance, as was the case with previous studies conducted in STAR [103].

REFERENCES

[1] M. S. Cengiz et al., "Price-efficiency relationship for photovoltaic systems on a global basis," *International Journal of Photoenergy,* 256101, *pp 1-12,* (2015).

[2] J. Ramanujam et al., "Copper indium gallium selenide based solar cells - A review," *Energy and Environmental Science*, 10(6), pp 1306-1319, (2017).

[3] L. C. Andreani et al., "Silicon solar cells: Toward the efficiency limits," *Advances in Physics*, 4(1), 1548305, (2019).

[4] "Solar Frontier hits 23.35% efficiency with thin-film cell." [Online]. Available: https://renewablesnow.com/news/solar-frontier-hits-2335-efficiency-with-thin-film-cell-639947/. [Accessed: 11-Sep-2020].

[5] I. Repins *et al.*, "19.9%-efficient ZnO/CdS/CuInGaSe2 solar cell with 81.2% fill factor," *Prog. Photovoltaics Res. Appl.*, 16(3), pp 235-239, (2008).

[6] M. Kaelin et al., "Low-cost CIGS solar cells by paste coating and selenization," *Thin Solid Films*, 480, pp 486-490, (2005).

[7] Y. C. Lin et al., "Preparation and characterization of Cu(In,Ga)(Se,S) 2 films without selenization by co-sputtering from Cu(In,Ga)Se 2 quaternary and In2Se3 targets," *Appl. Surf. Sci.*, 257(9), pp 4278-4284, (2011).

[8] D. Lincot *et al.*, "Chalcopyrite thin film solar cells by electrodeposition," *Sol. Energy*, 77(7), pp 725-737, (2004).

[9] M. G. Panthani *et al.*, "Synthesis of CuInS2, CuInSe2, and Cu(In xGa1-x)Se2 (CIGS) nanocrystal 'inks' for printable photovoltaics," *J. Am. Chem. Soc.*, 130(49), 16770-16777, (2008).

[10] "About Solar Energy | SEIA." [Online]. Available: https://www.seia.org/initiatives/about-solar-energy. [Accessed: 09-Jan-2020].

[11] S. N. Nahar et al., "Solar Irradiance of the Earth's Atmosphere," *Clim. Chang. Food Secur. South Asia*, pp. 31–42, (2010).

[12] L. Wald et al., "Basics in solar radiation at earth surface ," hal-01676634, (2019).

[13] "Sky Renderer by Peter Kutz: Spectral Solar Irradiance." [Online]. Available: http://skyrenderer.blogspot.com/2012/10/spectral-solar-irradiance.html. [Accessed: 09-Jan-2020].

[14] K. Tanabe et al., "A review of ultrahigh efficiency III-V semiconductor compound solar cells: Multijunction tandem, lower dimensional, photonic up/down conversion and plasmonic nanometallic structures," *Energies*, 2(3), pp. 504–530, (2009).

[15] E. Carrier et al., "Photovoltaics: The Basics," pp. 151–179, (2018).

[16] S. C. Erwin et al., "Doping semiconductor nanocrystals," *Nature, 436(7047)*, pp 91-94, (2005).

[17] B. Zaidi et al., "Introductory Chapter: Introduction to Photovoltaic Effect," in *Solar Panels and Photovoltaic Materials*, London UK, pp 1-8, (2018).

[18] J. J. M. Halls *et al.*, "Efficient photodiodes from interpenetrating polymer networks," *Nature*, 376(6540), pp 498-500, (1995).

[19] A. Helbig et al., "Quantitative electroluminescence analysis of resistive losses in Cu(In, Ga)Se2 thin-film modules," *Sol. Energy Mater. Sol. Cells*, 94(6), pp 978-984, (2010).

[20] H. Fu et al., "Efficiency droop in GaInN/GaN LEDs," *Nitride Semicond. Light. Diodes Mater. Technol. Appl., 2*, pp. 299–325, (2018).

[21] A. Vossier et al., "Is Auger recombination the ultimate performance limiter in concentrator solar cells?," *Appl. Phys. Lett.*, 97(19), 193509-193509-3, (2010).

[22] H. Yu et al., "II-VI compound semiconductor nanowires: Optical properties and nanophotonics,",

Semiconductor Nanowires: Materials, Synthesis, Characterization and Applications, pp 29-69, (2015).
[23] D. Reguera et al., "Kinetic equations for diffusion in the presence of entropic barriers," *Phys. Rev. E*, 64(6), 061106, (2001).
[24] M. Henini et al., "Principles of Electronic Materials and Devices (Second Edition)," *Microelectronics J.*, 33, pp 681-681, (2002).
[25] "CollectionProbability | PVEducation."[Online]. Available: https://www.pveducation.org/pvcdrom/solar-cell-operation/collection-probability. [Accessed: 13-Jan-2020].
[26] T. H. Sajeesh et al , "Significance of Absorber Layer in Thin Film Solar Cells," pp. 1–61, (2012).
[27] B. J. Skromme et al., in "Semiconductor Heterojunctions," *Encyclopedia of Materials: Science and Technology*, (2006).
[28] F. Rana et al., in "Semiconductors Optoelectronics", Chapter 2: "Semiconductor Heterostructures," *Semicond. Optoelectron.*, pp. 1–29, (2011).
[29] P. Perfetti et al., "The problem of heterojunction band discontinuities," *Surf. Sci.*, 189, pp 362-382, (1987).
[30] S. M. Myers et al., "Recombination by band-to-defect tunneling near semiconductor heterojunctions: A theoretical model," *J. Appl. Phys.*, 120(13), 134502, (2016).
[31] M. Nariman et al., "Diagnosis of photovoltaic modules using alternate methods of measurement," Bachelor Thesis, (2017).
[32] G. E. Jellison et al., *Crystalline silicon solar cells*, vol. 212. (2018).
[33] "File:I-V Curve n.PNG - Wikimedia Commons." [Online]. Available: https://commons.wikimedia.org/wiki/File:I-V_Curve_n.PNG. [Accessed: 22-Jan-2020].
[34] M. Jiang et al., "Cu2ZnSnS4 Thin Film Solar Cells: Present Status and Future Prospects," *Solar Cells - Research and Application Perspectives*, (2013).
[35] Z. Crossbeam et al., "FIB-SEM Investigations of the Microstructure of CIGS Solar Cells", (2018).
[36] S. Sharbati et al., "Impact of the band offset for n-Zn(O,S)/p-Cu(In,Ga)Se2 solar cells," *IEEE J. Photovoltaics*, 4(2), pp 697-702, (2014).
[37] S. Shirakata et al., "Effects of CdS buffer layers on photoluminescence properties of Cu(In,Ga)Se2 solar cells," *Sol. Energy Mater. Sol. Cells*, 93(6-7), pp 988-992, (2009).
[38] K. H. Ong *et al.*, "Review on substrate and molybdenum back contact in CIGS thin film solar cell," *International Journal of Photoenergy*, 9106269 , (2018).
[39] F. Kessler et al., "Technological aspects of flexible CIGS solar cells and modules," *Sol. Energy*, 77,(6) pp 685-695, (2004).
[40] Dai, Xinyi et al., "Molybdenum thin films with low resistivity and superior adhesion deposited by radio-frequency magnetron sputtering at elevated temperature," *Thin Solid Films*, 567, pp 64-71, (2014).
[41] P. M. P. Salomé et al., "Mo bilayer for thin film photovoltaics revisited," *J. Phys. D. Appl. Phys.*, 43(34), 345501, (2010).
[42] T. Wada et al., "Characterization of the Cu(In,Ga)Se2/Mo interface in CIGS solar cells," *Thin Solid Films*, 387(1-2), pp 182-122, (2001).
[43] F. S. Hasoon et al., "The formation of the MoSe 2 layer at Mo/CIGS interface and its effect on the CIGS device performance," 2017 *IEEE 44th Photovolt. Spec. Conf. (PVSC)*, 7749861, pp. 1–5, (2017).
[44] E. S. Mungan et al., "Modeling the effects of Na incorporation on CIGS solar cells," *IEEE J. Photovoltaics*, 3, pp 451-456, (2013).
[45] H. P. Chen *et al.*, "Analysis of high-efficiency Mo-Based solar selective absorber by admittance locus method," *Coatings*, 9(4), pp 256, (2019).

[46] T. Klinkert et al., “Comprehension and optimisation of the co-evaporation deposition of Cu (In , Ga) Se2 absorber layers for very high efficiency thin film solar cells Torben Klinkert,” Diss. Université Pierre et Marie Curie-Paris VI, (2015).
[47] H.-W. Schock et al., in "Thin-Film Solar cells", Chapter 10: “Properties of Chalcopyrite-Based Materials and Film Deposition for Thin-Film Solar Cells,” Berlin, Heidelberg, pp 163-182, (2004).
[48] J. A. Berumen-Torres *et al.*, “Properties of ZnO-Cu_2-xSe thin films deposited by sputtering from composite ZnSe-Cu_2O targets,” *Opt. Mater. Express*, 6(9), pp. 2812-2823, (2016).
[49] J. J. Loferski et al., “Theoretical considerations governing the choice of the optimum semiconductor for photovoltaic solar energy conversion,” *J. Appl. Phys.*, 27(7), pp 777-784, (1956).
[50] W. Shockley et al., “Detailed balance limit of efficiency of p-n junction solar cells,” *J. Appl. Phys.*, 32(3), pp 510-519, (1961).
[51] Y. Hirai et al., “Numerical study of Cu(In,Ga)Se2 solar cell performance toward 23% conversion efficiency,” *Jpn. J. Appl. Phys.*, 53(1), 012301, (2014).
[52] T. Feurer *et al.*, “Progress in thin film CIGS photovoltaics – Research and development, manufacturing, and applications,” *Prog. Photovoltaics Res. Appl.*, 25(7), pp 645-667, (2017).
[53] E. Avancini *et al.*, “Voids and compositional inhomogeneities in Cu(In,Ga)Se2 thin films: evolution during growth and impact on solar cell performance,” *Sci. Technol. Adv. Mater.*, 19(1), pp 871-882, (2018).
[54] A. V. Mudryi *et al.*, “Structural and optical properties of thin films of Cu(In,Ga)Se2 semiconductor compounds,” *J. Appl. Spectrosc.*, 77(3), pp 371-377, (2010).
[55] W. Witte et al., “Raman investigations of Cu(In,Ga)Se2 thin films with various copper contents,” *Thin Solid Films*, 517(2), pp 867-869, (2008).
[56] U. Rau et al., in Practical Handbook of Photovoltaics, “Cu(In,Ga)Se2 Thin-Film Solar Cells,” *Solar Cells*, pp 367-413, (2013).
[57] D. Rudmann, “Effects of sodium on growth and properties of Cu(In,Ga)Se2 thin films and solar cells,” *Thesis*, (2004).
[58] X. Zhu et al., “Determining factor of MoSe 2 formation in Cu(In,Ga)Se 2 solar Cells,” *Sol. Energy Mater. Sol. Cells*, 101, pp 57-61, (2012).
[59] P. Jackson et al., “Effects of heavy alkali elements in Cu(In,Ga)Se2 solar cells with efficiencies up to 22.6%,” *Phys. Status Solidi - Rapid Res. Lett.*, 10(8), pp 583-586, (2016).
[60] I. The et al., “Chapter 1 Buffer Layer for Thin Film Heterojunction Solar Cells,” *Sol. Cells*, pp. 1–26.
[61] T. Minemoto *et al.*, “Theoretical analysis of the effect of conduction band offset of window/CIS layers on performance of CIS solar cells using device simulation,” *Sol. Energy Mater. Sol. Cells*, 67(1-4), pp 83–88, (2001).
[62] D. Kim *et al.*, “Optimization of CdS buffer layer for high efficiency CIGS solar cells,” *J. Nanosci. Nanotechnol.*, 16(5), pp 5074–5077, (2016).
[63] F. Bittau et al., “Analysis and Optimisation of Window Layers for Thin Film CdTe Solar Cells,” Dissertation. Loughborough University, (2017).
[64] R. S. Araoz, “Chemical bath deposition of Zn (S,O) buffer layers and application in Cd-free chalcopyrite-based thin-film solar cells and modules,” Dissertation, *Helmholtz Zent. Berlin, Berlin, Ger.*, (2009).
[65] B. L. Williams et al., “The competing roles of i-ZnO in Cu(In,Ga)Se2 solar cells,” *Sol. Energy Mater. Sol. Cells*, 157, pp 798-807, (2016).
[66] W. J. Maeng et al., “Studies on optical, structural and electrical properties of atomic layer deposited Al-doped ZnO thin films with various Al concentrations and deposition temperatures,” *J. Phys. D. Appl. Phys.*, 44(44), 445305, (2011).

[67] C. H. Zhai *et al.*, "Effects of Al Doping on the Properties of ZnO Thin Films Deposited by Atomic Layer Deposition," *Nanoscale Res. Lett.*, 11(1), pp 1-8, (2016).
[68] J. C. Lee et al., "RF sputter deposition of the high-quality intrinsic and n-type ZnO window layers for Cu(In,Ga)Se2-based solar cell applications," *Sol. Energy Mater. Sol. Cells*, 64(2), pp 185-195, (2000).
[69] Y. Qiu et al., "Direct current sputtered aluminum-doped zinc oxide films for thin crystalline silicon heterojunction solar cell," *Mater. Chem. Phys.*, 141(2-3), pp 744-751, (2013).
[70] D. Kim et al., "Fabrication of rough Al doped ZnO films deposited by low pressure chemical vapor deposition for high efficiency thin film solar cells," in *Current Applied Physics*, , 10(3), pp 5 459-462, (2010).
[71] K. moh Linet al., "Parametric study on preparation and characterization of ZnO:Al films by sol-gel method for solar cells," *Mater. Sci. Eng. B Solid-State Mater. Adv. Technol.*, 139(1), pp 81-87, (2007).
[72] J. Song et al., "Properties of ZnO:Al thin films for solar cells by pyrosol method," *Conference Record of the IEEE Photovoltaic Specialists Conference*, 1, pp 630-633, (1994).
[73] L. Cao et al."Highly transparent and conducting fluorine-doped ZnO thin films prepared by pulsed laser deposition," *Sol. Energy Mater. Sol. Cells*, 95(3), pp 894-898, (2011).
[74] "Sputtering System – AJA ATC Orion 8 | PoliFAB." [Online]. Available: https://www.polifab.polimi.it/equipments/orion-8/. [Accessed: 29-Sep-2020].
[75] R. Würz et al. "Native oxidation of CuGaSe2 crystals and thin films studied by electron paramagnetic resonance and photoelectron spectroscopy," *Phys. Rev. B - Condens. Matter Mater. Phys.*, 70(20), 205321, (2004).
[76] D. Fuster *et al.*, "System for manufacturing complete Cu(In,Ga)Se2 solar cells in situ under vacuum," *Sol. Energy*, 198, pp 490-498, (2020).
[77] R. Apkarian et al, , *Self-studies prior to Fundamentals of Scanning Electron Microscopy*, (2018).
[78] Www.iitk.ac.in, "Image Formation and Interpretation SEM Imaging Process," *Indian Inst. Technol. Kanpur*, 2018.
[79] JEOL, "Scanning Electron Microscope A To Z," *Serv. Adv. Technol.*, (2006).
[80] "CMP - FIB (Universität Paderborn)." [Online]. Available: https://chemie.uni-paderborn.de/en/research-groups/technische-chemie/cmp/facilities/fib/. [Accessed: 27-Feb-2020].
[81] W. D. Callister et al.*Materials Science and Engineering 9th Edition*. (2014).
[82] S. A. Speakman et al, "Introduction to X-Ray Powder Diffraction Data Analysis," *Mater. Sci. and Engineering at MIT*, (2003).
[83] C. V Raman et al., "A new class of spectra due to secondary radiation Part I," 419, (1928).
[84] P. K. Mishra et al. , "Effect of processing parameter on structural, optical and electrical properties of photovoltaic chalcogenide nanostructured RF magnetron sputtered thin absorbing films," *Mater. Sci. Semicond. Process.*, 25, pp 307-319, (2014).
[85] T. P. Hsieh et al., "Effects of residual copper selenide on CuInGaSe2 solar cells," *Solid. State. Electron.*, 56(1), pp 175-178, (2011).
[86] A. Chirila *et al.*, "CIGS solar cells grown by a three-stage process with different evaporation rates," *Conference Record of the IEEE Photovoltaic Specialists Conference*, 34, pp 812-816, (2009).
[87] K. Decock et al., "Characterization of graded CIGS solar cells," *Energy Procedia*, 2(1), pp 49-54, (2010).
[88] J. Chen *et al.*, "Effect of substrate temperature and post-annealing on the properties of CIGS thin films deposited using e-beam evaporation," *J. Phys. D. Appl. Phys.*, 49(49), 495601, (2016).
[89] C. Insignares-Cuello et al., "Raman scattering analysis of electrodeposited Cu(In,Ga)Se2 solar cells: Impact of ordered vacancy compounds on cell efficiency," *Appl. Phys. Lett.*, 105(2),

021905, (2014).
[90] C. Persson et al., “Anomalous grain boundary physics in polycrystalline: CuInSe2: The existence of a hole barrier,” *Phys. Rev. Lett.*, 91(26), 266401, (2003).
[91] C. R. M. Grovenor et al., “Grain boundaries in semiconductors,” *J. Phys. C Solid State Phys.*, 18(21), 4079, (1985).
[92] N. Nicoara *et al.*, “Direct evidence for grain boundary passivation in Cu(In,Ga)Se2 solar cells through alkali-fluoride post-deposition treatments,” *Nat. Commun.*, 10(1), pp 1-8, (2019).
[93] J. E. Lee et al., “Deposition and characterization of Cu(In,Ga)Se2 thin films from the ink of sonochemically prepared CIGSe nanoparticles,” *Chinese J. Phys.*, 56(1), pp 392-403, (2018).
[94] S. Jung et al., “Effects of Ga contents on properties of CIGS thin films and solar cells fabricated by co-evaporation technique,” *Curr. Appl. Phys.*, 10(4), pp 990-996, (2010).
[95] F. Couzinié-Devy et al., “Re-investigation of preferential orientation of Cu(In,Ga)Se2 thin films grown by the three-stage process,” *Prog. Photovoltaics Res. Appl.*, 19(5), pp 527-536, (2011).
[96] Y. Shi et al, “Effects of post-heat treatment on the characteristics of chalcopyrite CuInSe2 film deposited by successive ionic layer absorption and reaction method,” *Thin Solid Films*, 515(7-8), pp 3339-3343, (2007).
[97] M. Esmaeili-Zare *et al.*, “The role of Na incorporation in the low-temperature processed CIGS thin film solar cells using post deposition treatment,” *J. Alloys Compd.*, 658, pp 12-18, (2016).
[98] P. Tsoulka et al., “Detrimental copper-selenide bulk precipitation in CuIn1-xGaxSe2 thin-film solar cells. A possible reason for the limited performance at large x?,” *Thin Solid Films*, 712, 138297, (2020).
[99] T. Walter et al., “Crystal growth and diffusion in Cu(In, Ga)Se2 chalcopyrite thin films,” *Thin Solid Films*, 224(1), pp 74-81, (1993).
[100] M. R. Balboul et al., “Correlation of structure parameters of absorber layer with efficiency of Cu(In,Ga)Se2 solar cell,” *Applied Physics A: Materials Science and Processing*, 92(3), pp 557-563, (2008).
[101] D. Abou-Ras *et al.*, “Impact of the Ga concentration on the microstructure of CuIn1-x Gax Se2,” *Phys. Status Solidi - Rapid Res. Lett.*, 2(3), pp 135-137, (2008).
[102] K. Timmo *et al.*, “Cu(In,Ga)Se2 monograin powders with different Ga content for solar cells,” *Sol. Energy*, 176, pp 648-655, (2018).
[103] Daniel Brito et al., "Growth and characterization of Cu(In,Ga)Se_2 thin film for solar cells by pulsed hybrid reactive magnetron sputtering ", Masther thesis, Universidade do Minho, (2019)
[104] Marina Alves et al., "Cu(In,Ga)Se2 thin film solar cell by magnetron sputtering", Master thesis, Universidade do Minho, (2017)

ANNEX 1 – COMPARISON OF ABSORBER LAYERS AND SOLAR CELLS GROWN WITH CU-RICH AND CU-POOR SPUTTER TARGETS

Previous studies conducted in STAR consisted of depositing CIGSe absorber layers with a Cu-poor target with the following composition: $Cu_{0.5}In_{0.35}Ga_{0.15}$, at depositions temperatures of 200 °C, 400 °C, and 500 °C [103]. This target will lead to Cu-poor compositions without the necessity of KCN/ Indium post-deposition. Furthermore, different GGI ratios were obtained, as the GGI ratio of this target was 0.3. Note that the GGI ratio of the target used in this thesis was 0.4. The sputtering conditions were very similar to the ones used in this thesis (see Table 14), and the selenium supply conditions were the same (i.e. same valve opening, and the same pulses). Here, a direct comparison of the CIGSe layers and solar cells deposited with the different Cu-In-Ga targets (Cu-poor and Cu-rich) will be conducted.

Table 14. Sputtering conditions of Cu(In,Ga)Se_2 films with Cu-poor [103], and Cu-rich Cu-In-Ga targets.

Target	Thickness (nm)	Power (W)	Time (min)	Pressure (mbar)
Cu-poor	2000	30	100	6×10^{-3}
Cu-rich	2000	30	52	5.6×10^{-3}

Characterization of the absorber Layer

Figures 59, 60, and 61 show a side-by-side SEM image comparison of the absorber layers grown with the different targets at depositions temperatures of 200 °C, 400 °C, and 500 °C, respectively. The "Indium PD" sample refers to the sample grown at 500 °C with a CIGSe thickness of 1400 nm and a In-Se thickness of 600 nm, as shown in Chapter 6. It was observed that, for the same deposition temperature, CIGSe layers grown under Cu-rich conditions show significantly larger crystals than layers grown under a Cu-poor environment. These results confirm the initial hypothesis, that Cu-rich conditions favor crystal growth. The crystal growth enhancement was more noticeable at a deposition temperature of 200 °C, where the grains reached sizes of 450 nm for the Cu-poor target and, for the Cu-rich target, grains as big as 1.1 μm were detected. Different grain morphologies between Cu-rich and Cu-poor growth conditions were also obtained, particularly for the 400 °C sample, where the Cu-poor sample exhibits triangular shaped grains.

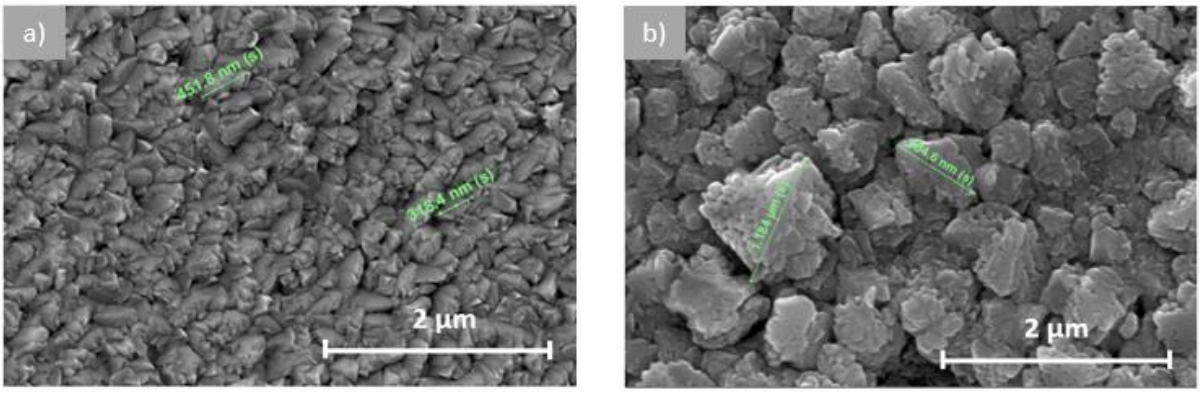

Figure 59. SEM Images of CIGSe crystals grown at a deposition temperature of 200 °C with a (a) Cu-poor target [103], and (b) Cu-rich target.

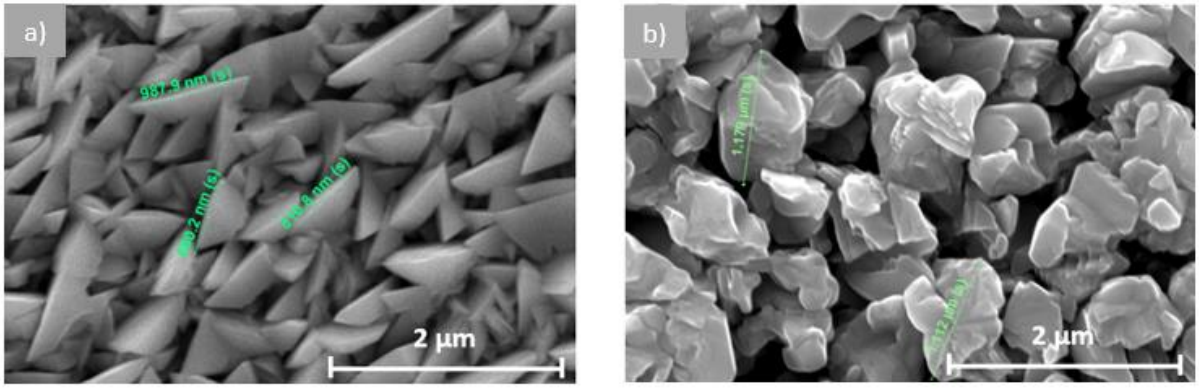

Figure 60. SEM Images of CIGSe crystals grown at a deposition temperature of 400 °C with a (a) Cu-poor target [103], and (b) Cu-rich target.

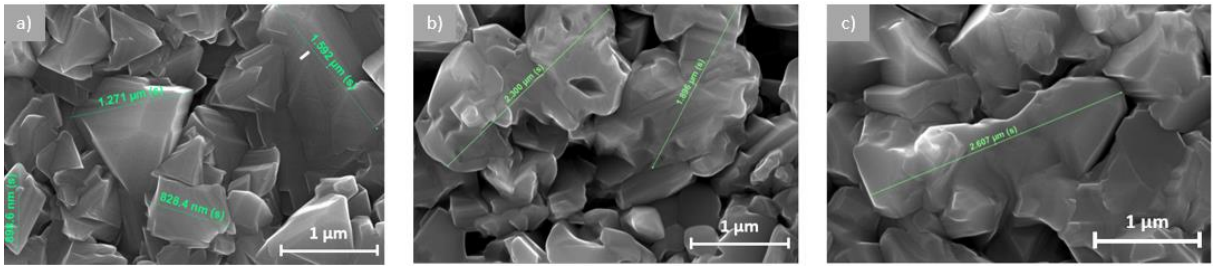

Figure 61. SEM Images of CIGSe crystals grown at a deposition temperature of 500 °C with a (a) Cu-poor target [103], (b) Cu-rich target and KCN-etching treatment, and (c) Cu-rich target and Indium post-deposition.

The chemical composition ratios measured by EDX are presented in Fig. 62. Following the KCN-etching treatment/Indium post-deposition, the samples grown with the Cu-rich target exhibit similar CGI ratios to the CGI ratio of the absorber layers grown with the Cu-poor target. The main difference in the stoichiometric properties obtained with the different targets is the GGI ratio. Owing to the high Cu atomic % of the Cu-rich target, there is an Indium deficiency in the target, which leads to higher GGI ratios. The exception is the Indium PD sample, which shows GGI ratios comparable to those grown under Cu-poor

conditions. The Selenium ratios of the CIGSe layers grown with the Cu-poor target are higher than the ones obtained for the Cu-rich target.

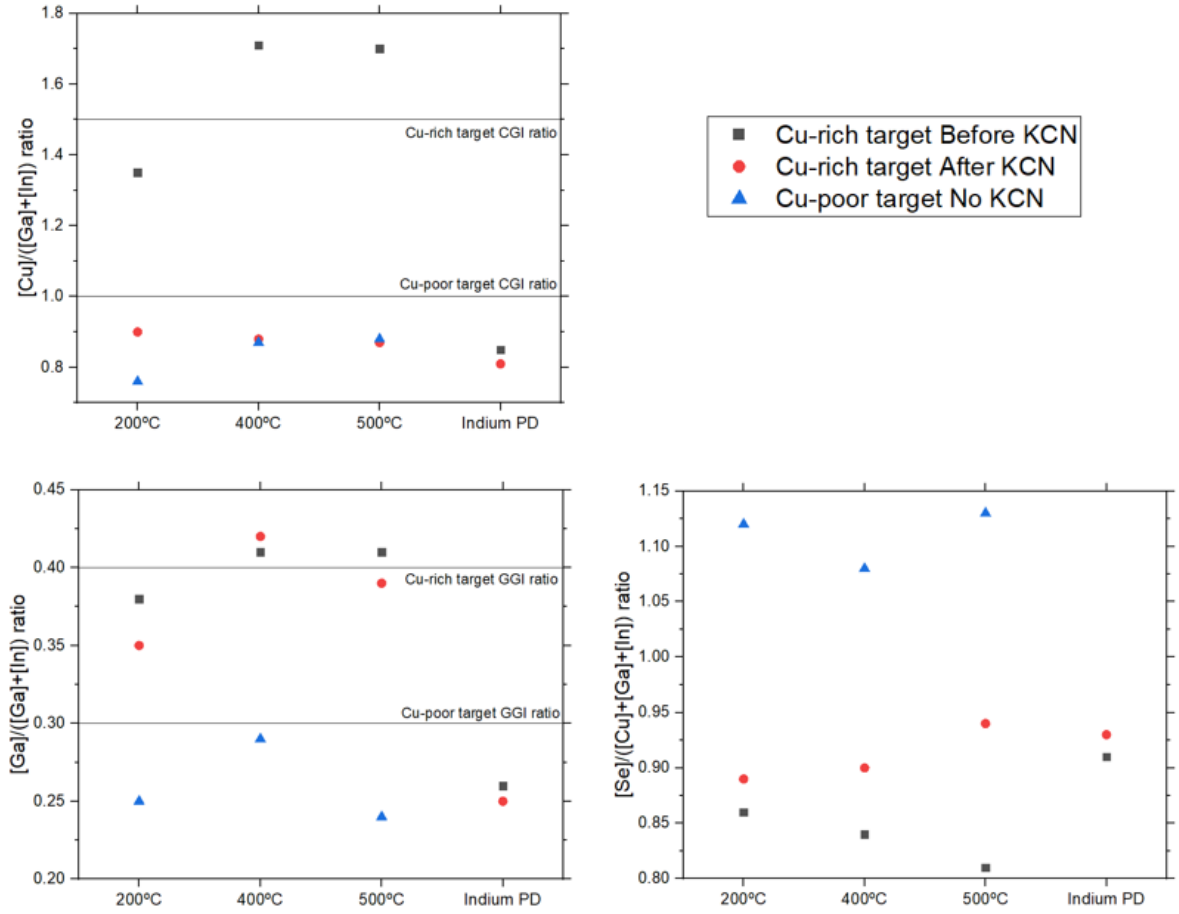

Figure 62. Stoichiometric ratios of CIGSe layers grown with Cu-rich and Cu-poor [103], targets before and after KCN.

Fig. 63 shows a comparison of the XRD measurements obtained for all deposition temperatures. For all samples, the (112) orientation shows the largest peak intensity. Other CIGSe orientations corresponding to the (220), (312/116), and (400) planes were also detected. In a similar fashion to what was observed in the XRD measurements presented in Chapter 6, there is a shift of the reflection planes to lower 2θ angles for the Cu-poor samples, corresponding to the lower GGI ratios. The 400°C Cu-poor sample shows significantly smaller (112), and significantly higher (220) peak intensities, when in comparison with the results obtained for the Cu-rich sample. The 500 °C Cu-poor sample exhibited the largest (112) peak intensity of all absorber layers, however some unidentified peaks at diffraction angles of 37.1°, 38.2°, and 41.3° were detected.

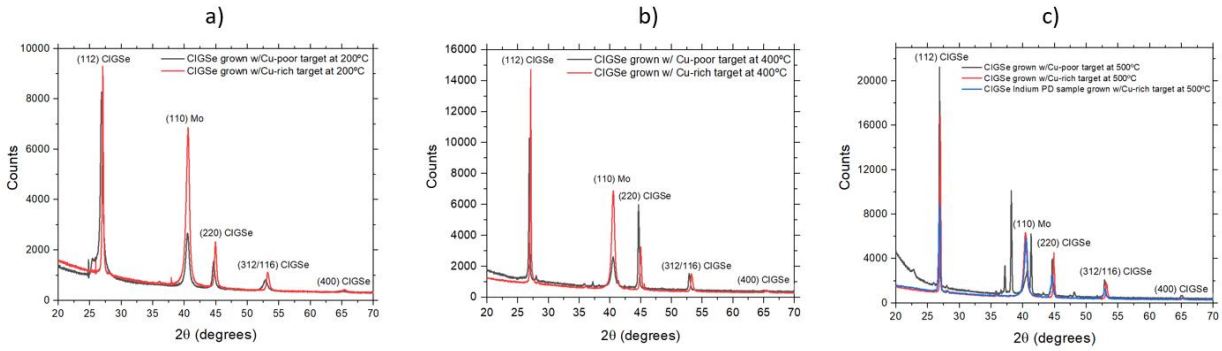

Figure 63. XRD patterns of CIGSe films grown at with a Cu-poor [103], and Cu-rich target at (a) 200°C, (b) 400°C, and (c) 500°C.

Fig. 64 presents the texture coefficient for all the CIGSe layers studied in this chapter. The 200 °C and 500 °C samples showed similar results to the CIGSe layers grown under Cu-rich conditions, where the texture coefficient of the (112) peak is greater than 1, thus it is the preferred crystal orientation. In fact, the texture coefficient of the (112) peak for these Cu-poor samples is higher than those obtained for the Cu-rich samples, confirming what was previously observed in Chapter 6: lower GGI ratios seem to favor the (112) growth direction. The 400 °C sample showed different results. Owing to the high (220) peak intensity, this absorber layer shows a texture coefficient greater than unity for both (112) and (220) planes. This means that, in contrast with what was observed in all other layers, where the preferential orientation was only the (112) orientation, this sample shows preferential orientation along both (112) and (220) planes, possibly related to the different triangular morphology obtained in the SEM analysis for this absorber layer.

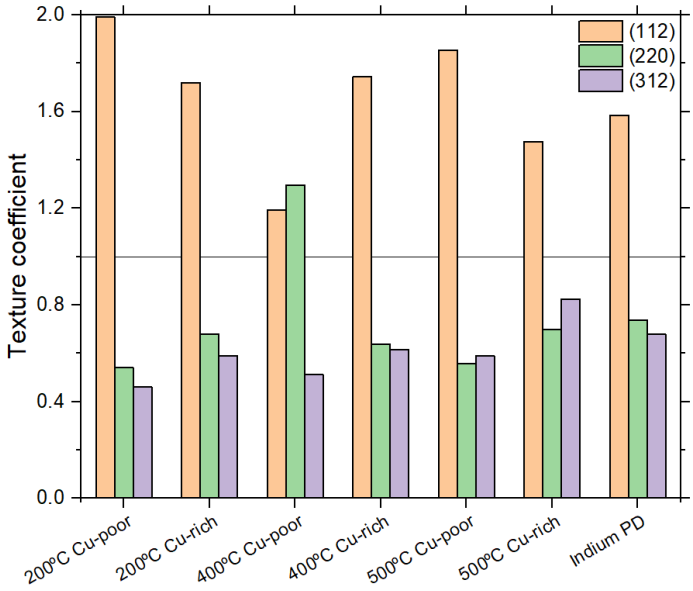

Figure 64. Texture coefficient of the different CIGSe peaks for absorber layers deposited with Cu-rich and Cu-poor target [103], at different temperatures.

To confirm the grain size enhancement resulting from the stoichiometric nature of the CIG target, the average grain size measured in SEM images is displayed in Fig. 65a. All films deposited with the Cu-rich target exhibit a higher average grain size than those grown with the Cu-poor target. The XRD-calculated crystallite size (which is dependent on both deposition temperature and GGI ratio) of the different absorbers layers is presented in Fig. 65b. It is observed that all CIGSe absorbers grown with the Cu-rich target show larger crystallite sizes than those grown with the Cu-poor target. The crystallite size drop observed for the Indium PD sample is a consequence of its low GGI ratio when in comparison with the other Cu-rich target grown samples, However, it shows larger crystallite size than all of the Cu-poor samples, meaning that the initial Cu-rich conditions have a more significant impact on the crystallite size than the impact of the GGI ratio.

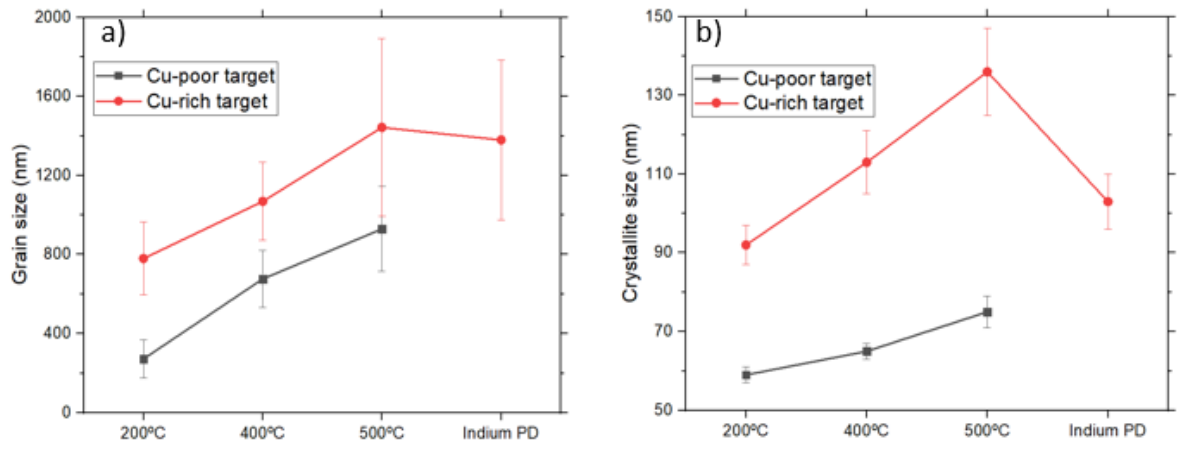

Figure 65. CIGSe crystal sizes for absorber layers grown with Cu-rich and Cu-poor targets [103], calculated with the average of the SEM analysis, and (b) CIGSe crystallite calculated with the XRD measurements/Scherrer equation

The calculated lattice parameters, a and c, for the different CIG targets and different deposition temperatures are shown in Fig. 66. With the exception of the Indium PD sample, samples grown under Cu-rich conditions reveal smaller lattice parameters than those of samples grown with the Cu-poor target. As explained in Chapter 6, inferior GGI ratios lead to the replacement of smaller Gallium ions by larger Indium ions, resulting in an increase in the lattice parameters.

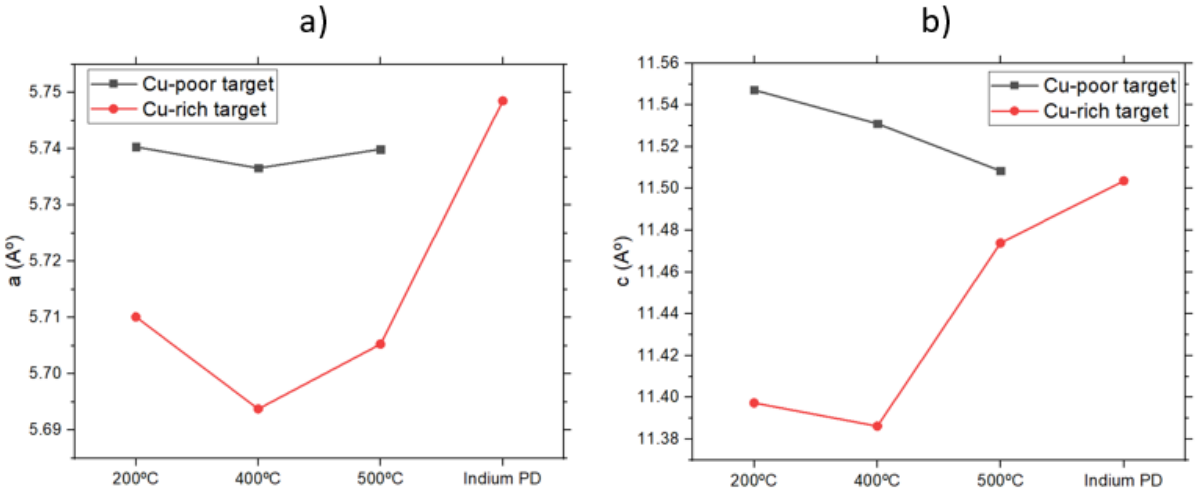

Figure 66. Influence of deposition temperature and CIG stoichiometric nature in the lattice parameters of the CIGSe absorber.

Solar cell analysis

To finalize the comparison of the effect of the different targets, solar cells were completed with a CdS buffer layer, deposited by chemical bath deposition, and a sputter-deposited i-ZnO/ZnO:Al double layer as the front contact. All samples, with the exception of the Indium PD sample, were submitted to a 30s

KCN-etching treatment. The best I-V curves obtained for deposition temperatures of 400 °C and 500 °C are presented in Fig. 67. It is important to notice that, for the Cu-poor target, the solar cells with CIGSe layer grown at 200 °C didn't manifest any efficiency, while the 200°C absorber grown with the Cu-rich target displayed an average efficiency of 1.5%. Furthermore, from the I-V curves presented in Fig. 67, it becomes clear that Cu-rich conditions enhance solar cell performance, especially at lower temperatures (200°C and 400°C).

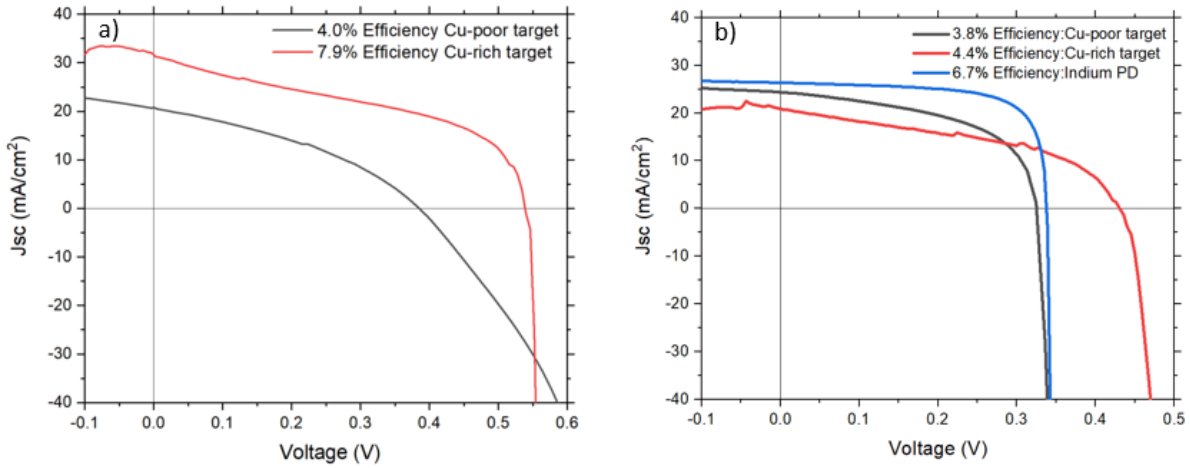

Figure 67. I-V curves of the best solar cells obtained for deposition temperatures of (a) 400°C, and (b) 500°C, for CIGSe layer grown with Cu-poor [103], and Cu-rich targets.

The box plots of the I-V parameters comparing the different deposition temperatures can be seen in Fig. 68. It can be observed that, for both Cu-In-Ga targets, there was a drop in efficiency when the deposition temperature increased from 400 °C to 500 °C. Despite this, CIGSe thin films grown under Cu-rich conditions manifest higher efficiencies than those grown under Cu-poor conditions. The Indium PD sample shows better efficiencies than the other 500 °C samples, but it did not reach efficiencies as high as the ones obtained for the 400 °C Cu-rich sample. This observation might be attributed to a lack of Selenium for the deposition at 500 °C, where Selenium can re-evaporate; optimization of the Selenium valve opening, or the Selenium pulses might be required. All Cu-rich samples show improved short-circuit current densities. The most improved parameter resulting from the Cu-rich target was the open-circuit voltage, due to the higher GGI ratios. The open-circuit voltage of the Indium PD sample is very similar to the V_{OC} displayed by the 500 °C Cu-poor sample. There was an improvement in fill-factor for the Cu-rich target for deposition temperatures of 400 °C, while for 500 °C the FF slightly decreased for the sample without the Indium post-deposition. The Indium PD sample was the sample with the highest fill factor

obtained in this thesis. The samples deposited with the Cu-rich target also manifest lower series resistances, and higher shunt resistance, which is beneficial for the solar cell performance.

Owing to the obtained I-V results and the improved crystalline properties, it is possible to conclude that the Cu-rich Cu-In-Ga target is the better target for CIGSe growth and solar cell performance.

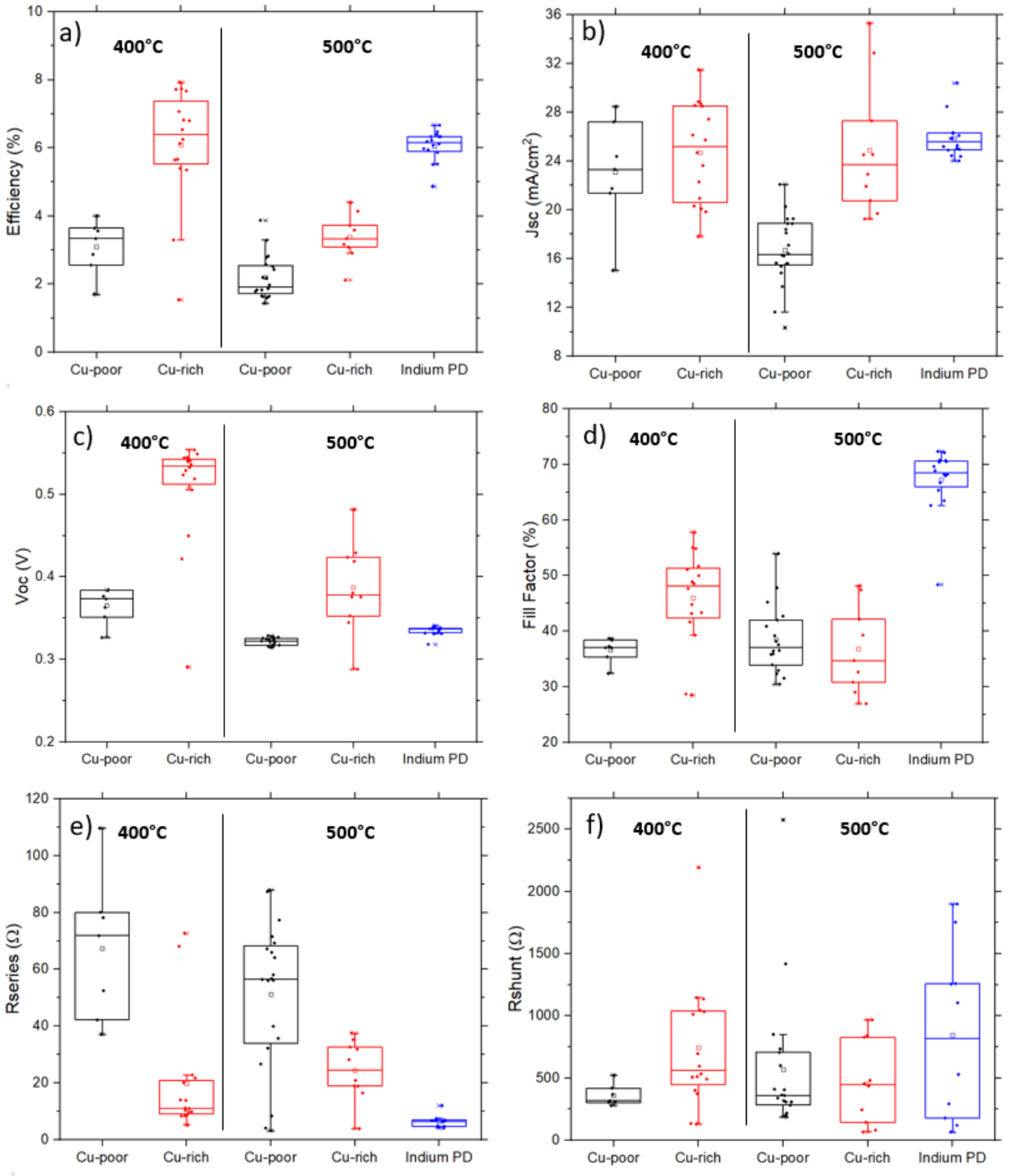

Figure 68. Box plot of (a) efficiency, (b) short-circuit current density, (c) open circuit voltage, (d) fill factor, (e) series and (f) shunt resistances of CIGSe solar cells deposited with a Cu-poor [103], and Cu-rich Cu-In-Ga target at deposition temperatures of 400 °C and 500 °C.